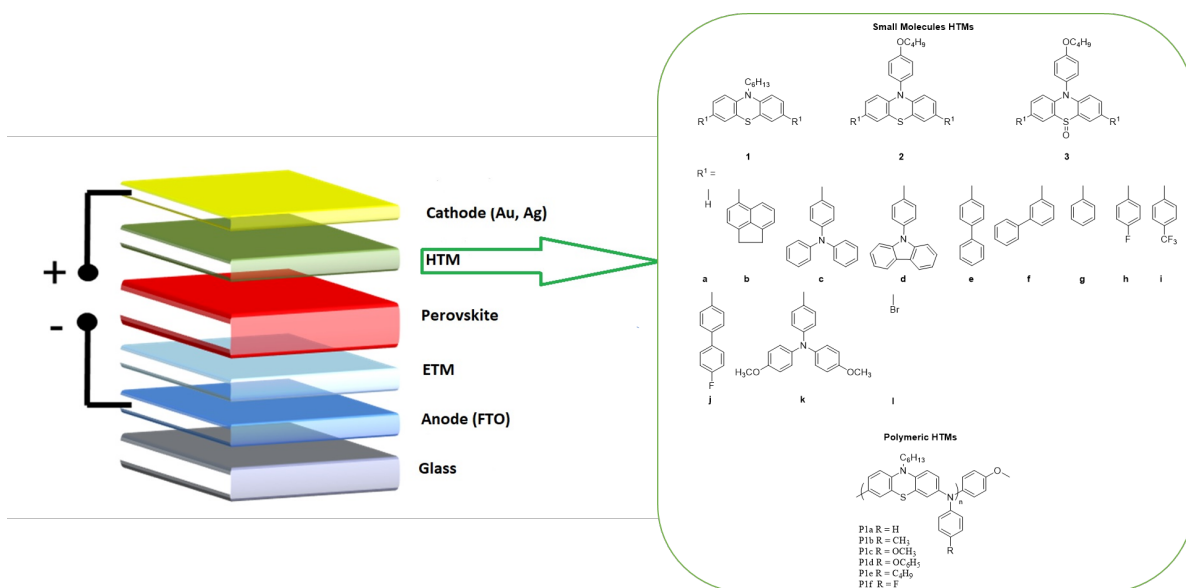




Università degli Studi di Torino
Doctoral School of the University of Torino
PhD Program in Chemical and Materials Sciences XXIV Cycle

Synthesis and Characterization of Phenothiazine-based Small molecule and Polymeric Transparent Organic Hole Transporting Materials for Perovskite Solar Cells



Mohamed Magdy Hassan Desoky

Supervisor:
Prof. Pierluigi Quagliotto



Università degli Studi di Torino
Doctoral School of the University of Torino
PhD Program in Chemical and Materials Sciences XXIV cycle

**Synthesis and Characterization of Phenothiazine-based Small molecule and
Polymeric Transparent Organic Hole Transporting Materials for Perovskite Solar
Cells**

Candidate: **Mohamed Magdy Hassan Desoky**

Supervisor: **Prof. Pierluigi Quagliotto**

Jury Members: **Prof. Alberto Minassi**

Università del Piemonte Orientale
Dipartimento di Scienze del Farmaco

Prof. Paola Delli Veneri

ENEA
Unità Tecnica Tecnologie Portici

Prof. Nadia Barbero

Università di Torino
Dipartimento di Chimica

Head of the Doctoral School: **Prof. Alberto Rizzuti**

PhD Programme Coordinator: **Prof. Bartolomeo Civalleri**

Torino, 2022

Abstract

In this work we are presenting the synthesis of novel classes of transparent Hole Transporting Materials (HTMs) based on Low-Cost Phenothiazine (PTZ) for perovskite solar cells applications. Three scaffolds based on PTZ were prepared either by alkylation of the nitrogen atom by nucleophilic substitution in presence of base (scaffold 1) or by Buchwald-Hartwig arylation (scaffold 2). Scaffolds 1 and 2 were brominated using bromine to prepare the intermediates for the coupling reactions, and the brominated scaffold 2 was further oxidized to prepare the scaffold 3 intermediate. The Suzuki coupling was used for the synthesis of small molecule based HTMs, while for the polymeric based HTMs Buchwald amination polymerization was preferred to polymerize the brominated scaffold 1 intermediate with different low-cost anilines. All HTMs were properly characterized with several techniques and were transparent to visible light. The tuning of the phenothiazine core and of their substituents gave access to new HTMs with different properties. Some of them were applied in perovskite solar cells, obtaining interesting results.

INDEX

1 Introduction	8
1.1 Motivation	8
1.2 Perovskite solar cells (PSCs)	10
1.2.1 Basic and working principle.....	10
1.2.2 Architectures and building blocks of Perovskites Solar Cells	14
1.2.3 Mesoscopic and planar structures	14
2 Building components of PSCs	19
2.1 An Overview	19
2.2 Hole-transporting materials (HTMs).....	22
2.2.1 Inorganic HTMs	25
2.2.2 Organic HTMs	26
2.2.3 Chemical Doping.....	34
3 Phenothiazine	36
3.1 Phenothiazine as a building block in organic semiconductors	36
3.2 Properties of Phenothiazine derivatives	39
3.2.1 Phenothiazine Based Hole Transporting Materials for PSCs	40
4 Transparent Tandem solar cells.....	51
4.1 Absorption of light irradiation in the UV-region (<450nm) and the NIR part (>700nm) portions of the solar spectra.	51
4.2 Transparent Hole Transporting Materials	52
5 Methodology Development.....	54
5.1 An overview	54
5.2 Development of phenothiazine-based hole transporting materials	58
5.3 Synthetic Strategy.....	59
5.3.1 Scaffolds core preparation	60

5.3.2 Preparation of Arylboronate reagents	66
5.4 HTMs Synthesis.....	69
5.4.1 <i>HTM Small Molecules</i>	69
5.4.2 Polymeric HTMs	76
6 Synthesis and characterization of small molecule based HTMs.....	80
6.1 Series 1	80
6.1.1 Synthesis.....	80
6.1.2 Characterization	82
6.2 Series 2 and 3	89
6.2.1 Synthesis.....	89
6.2.2. Characterization	92
6.3 Conclusions.....	103
6.4 Effect of slight modifications of the triphenylamine unit on the HTMs properties and performance	109
6.5 Effect of the modification of the phenothiazine core on the properties and performances of HTMs	121
6.5.1 Absorption and emission through UV-Vis and Fluorescence spectroscopy..	121
6.5.2 Electrochemical characterization through cyclic voltammetry.....	123
6.5.3 Thermal Stability through TGA and DSC.....	124
7 Synthesis and characterization of Phenothiazine Polymeric based HTMs: Results and Discussion	129
7.1 An overview	129
7.2 Synthesis.....	129
7.3 Characterization	131
7.3.1 Molecular weight measurement by SEC	131
7.3.2 Absorption and emission through UV-Vis and Fluorescence spectroscopy..	131
7.3.3 Thermal Stability through TGA and DSC.....	133

7.3.4 Electrochemical characterization through cyclic voltammetry.....	136
8 Experimental.....	139
8.1 Materials and instruments	139
8.1.1 Materials	139
8.1.2 Instruments	139
8.2 Synthesis.....	142
8.2.1 10-hexyl-10H-phenothiazine (1a).....	142
8.2.2 3,7-dibromo-10-hexyl-10H-phenothiazine (1l)	143
8.2.3 10-(4-butoxyphenyl)-10H-phenothiazine (2a)	144
8.2.4 3,7-dibromo-10-(4-butoxyphenyl)-10H-phenothiazine (2l)	145
8.2.5 10-(4-butoxyphenyl)-10H-phenothiazine 5-oxide (3a).....	146
8.2.6 3,7-dibromo-10-(4-butoxyphenyl)-10H-phenothiazine 5-oxide (3l)	147
8.2.7 N,N-diphenyl-4-(4,4,5,5-tetramethyl-1,3,2-dioxaborolan-2-yl)aniline (c) ...	148
8.2.8 2-(1,2-dihydroacenaphthylen-5-yl)-4,4,5,5-tetramethyl-1,3,2-dioxaborolane (b)	149
8.2.9 9-(4-bromophenyl)-9H-carbazole (d-Br)	150
8.2.10 9-(4-(4,4,5,5-tetramethyl-1,3,2-dioxaborolan-2-yl)phenyl)-9H-carbazole (d)	151
8.2.11 2-([1,1'-biphenyl]-4-yl)-4,4,5,5-tetramethyl-1,3,2-dioxaborolane (e).....	151
8.2.12 4-methoxy-N-(4-methoxyphenyl)-N-(4-(4,4,5,5-tetramethyl-1,3,2-dioxaborolan-2-yl)phenyl)aniline (k).....	152
8.2.13 4,4'-(10-hexyl-10H-phenothiazine-3,7-diyl)bis(N,N-diphenylaniline) (1c) .	153
8.2.14 4,4'-(10-hexyl-10H-phenothiazine-3,7-diyl)bis(N,N-bis(4-methoxyphenyl)aniline) (1k)	154
8.2.15 3,7-bis(1,2-dihydroacenaphthylen-5-yl)-10-hexyl-10H-phenothiazine (1b)	155
8.2.16 3,7-bis(4-(9H-carbazol-9-yl)phenyl)-10-hexyl-10H-phenothiazine (1d)	155
8.2.17 3,7-di([1,1'-biphenyl]-4-yl)-10-hexyl-10H-phenothiazine (1e)	156
8.2.18 3,7-di([1,1'-biphenyl]-3-yl)-10-hexyl-10H-phenothiazine (1f)	156

8.2.19 4,4'-(10-(4-butoxyphenyl)-10H-phenothiazine-3,7-diyl)bis(N,N-diphenylaniline) (2c)	157
8.2.20 4,4'-(10-(4-butoxyphenyl)-10H-phenothiazine-3,7-diyl)bis(N,N-bis(4-methoxyphenyl)aniline) (2k)	158
8.2.21 3,7-bis(4-(9H-carbazol-9-yl)phenyl)-10-(4-butoxyphenyl)-10H-phenothiazine (2d)	158
8.2.22 10-(4-butoxyphenyl)-3,7-bis(1,2-dihydroacenaphthylen-5-yl)-10H-phenothiazine (2b)	159
8.2.23 3,7-di([1,1'-biphenyl]-4-yl)-10-(4-butoxyphenyl)-10H-phenothiazine (2e)	160
8.2.24 10-(4-butoxyphenyl)-3,7-diphenyl-10H-phenothiazine (2g)	160
8.2.25 10-(4-butoxyphenyl)-3,7-bis(4-fluorophenyl)-10H-phenothiazine (2h)	161
8.2.26 10-(4-butoxyphenyl)-3,7-bis(4-(trifluoromethyl)phenyl)-10H-phenothiazine (2i)	162
8.2.27 10-(4-butoxyphenyl)-3,7-bis(4'-fluoro-[1,1'-biphenyl]-4-yl)-10H-phenothiazine (2j)	162
8.2.28 10-(4-butoxyphenyl)-3,7-bis(4-(diphenylamino)phenyl)-10H-phenothiazine 5-oxide (3c)	163
8.2.29 3,7-bis(4-(9H-carbazol-9-yl)phenyl)-10-(4-butoxyphenyl)-10H-phenothiazine 5-oxide (3d)	164
8.2.30 10-(4-butoxyphenyl)-3,7-bis(4-(trifluoromethyl)phenyl)-10H-phenothiazine 5-oxide (3i)	165
8.2.31 P1a Polymer	166
8.2.32 P1b Polymer	167
8.2.33 P1c Polymer	168
8.2.34 P1d Polymer	168
8.2.35 P1e Polymer	169
8.2.36 P1f Polymer	169
9 References	170
list of abbreviations	209

1 INTRODUCTION

1.1 Motivation

To date, most of energy sources in the world are non-renewable sources, e.g. coal, crude oil, nature gas and uranium.¹ Their use has harmful effects on the environment causing the global warming and fast climate change on Earth. According to environmental scientists, the earth temperature has increased by more than one degree comparing to the 19th century.²

The earth temperature rising is mainly due to greenhouse effect, which is a result of the combustion of non-renewable energy sources. By 2070 the average air temperature during the summer of the Gulf-countries would make these states unsuitable for human life if the greenhouse gas release continues increasing with the current rates.²⁻⁵ Therefore, a constant and significant reduction of greenhouse gases release is required to overcome the issue of climate change.

Beside the above-mentioned harmful side-effects, the scarcity of not-renewable energy sources, is forcing the global community to look for new sustainable and cleaner energy resources, such as, solar, wind, hydroelectric, biomass, geothermal, ocean energy.⁶ A 430 quintillion Joules of energy (430×10^{18} J) are emitted every

hour by the sun while the world need of energy per year is 410 quintillion Joules, making the sun a perfect match as clean and sustainable source.⁵

Recently, the International Renewable Energy Agency has published the renewable capacity statical report of 2021, specifying that the world added more than 260 GW of renewable energies in 2020, exceeding expansion in 2019 by close to 50 %.⁷ In practice, solar and wind energy sources have shown remarkable expansion, with 127 GW and 111 GW of new installations in 2020, respectively, and both now make up more than half of the total installed renewable energy capacity.⁷ This is showing that solar as an energy source is one of the promising sources to achieve the global energy demands and the requirements of the Paris Agreement which requires the decrease the temperature by 1.5 °C in next 5 years.⁷ Although the raise in the global solar energy share, the total consumption of modern renewable energy sources including solar energy is too low (2%) comparing to fossil fuels (79.7%).⁸ To increase the share of solar energy, there is a strong need to research and develop new solar energy technologies. In general, photovoltaics solar cells are divided into three generation as shown in Figure 1.

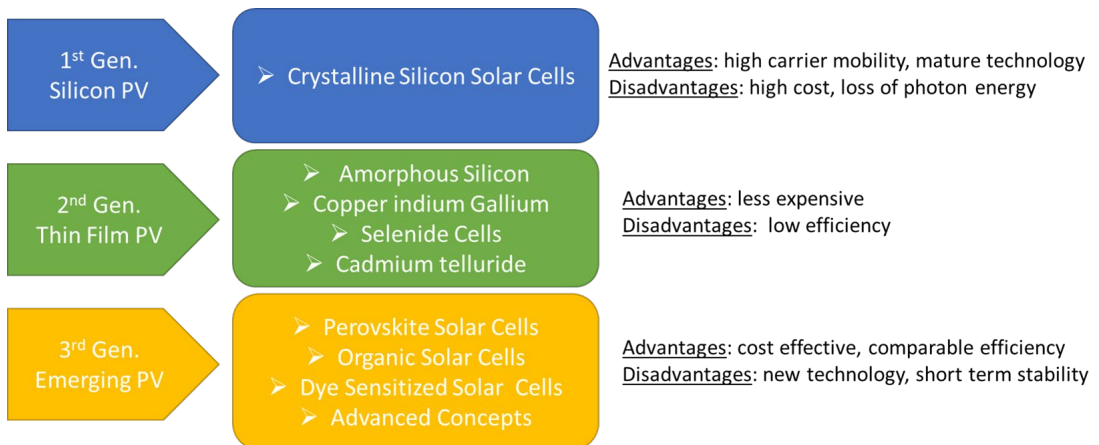


Figure 1. Generations of photovoltaics (Modified from Ref. 9).⁹

1.2 Perovskite solar cells (PSCs)

1.2.1 Basic and working principle

The Russian mineralogist Gustav Rose discovered perovskite material for first time in 1839.¹⁰ CaTiO_3 material was named perovskite after the Russian mineralogist Count Lev A. Perovski (1792-1856). CaTiO_3 can be converted to a semiconductor material by replacing the oxygen atoms by halogen atoms or a mixture of various halogen atoms. In general, perovskites have the structure of ABX_3 (Figure 2) with crystalline properties, containing three different inorganic or organic species: A is an Inorganic (e.g. Cs^+) or organic (e.g. Methyl ammonium MA), while B is a divalent cation (e.g. Pb(II) or Sn(II)), and X is a halogen or a mixture of different halogens (I, Br^- , Cl^-). The first use of a perovskite material in solar cells was in 2009 by Miyasaka

and co-workers using methylammonium lead bromide ($\text{CH}_3\text{NH}_3\text{PbBr}_3$) and methylammonium lead iodide ($\text{CH}_3\text{NH}_3\text{PbI}_3$) as sensitizers on TiO_2 in DSSC devices giving efficiencies of 3.13% and 3.81%, respectively.¹¹ Because of the interaction between the used iodide/triiodide liquid electrolyte in DSSCs with the perovskite, the two perovskites were degraded, rapidly. To overcome this degradation problem a solid-state HTM was designed and used as electrolyte, Spiro-OMeTAD, to replace the I^-/I_3^- liquid electrolyte.³ These DSSCs based on halide perovskite materials as active absorbent of light and solid state HTMs are called Perovskite Solar Cells (PSCs) and have captured the interest of many researchers in the field of photovoltaics technology.

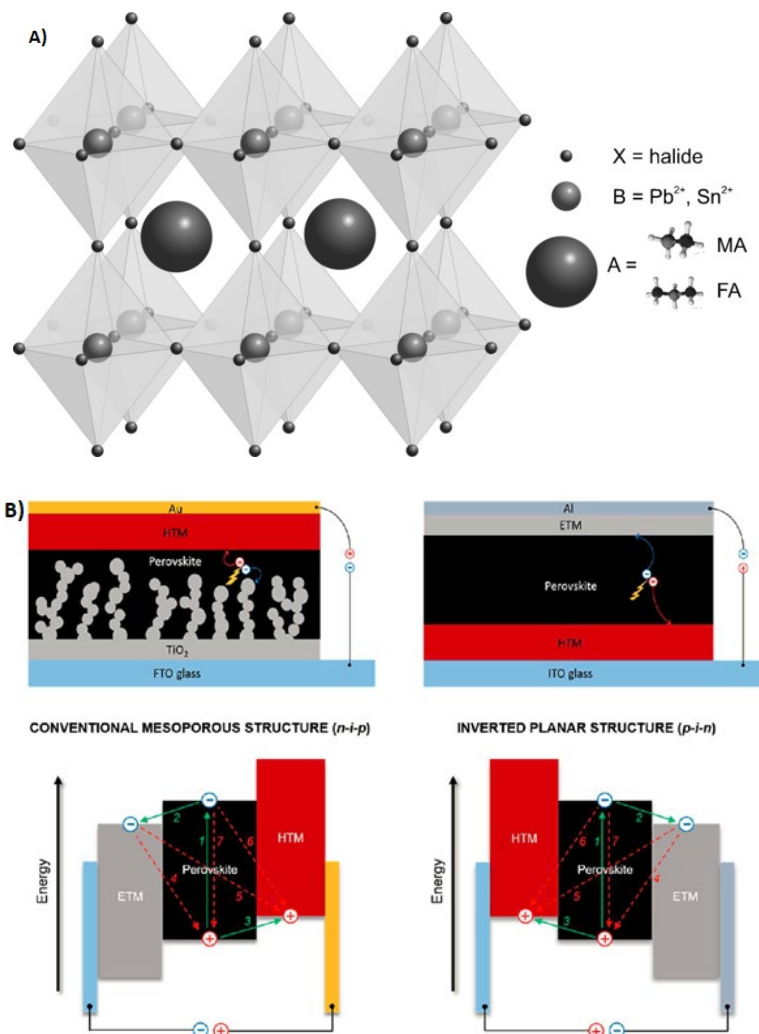
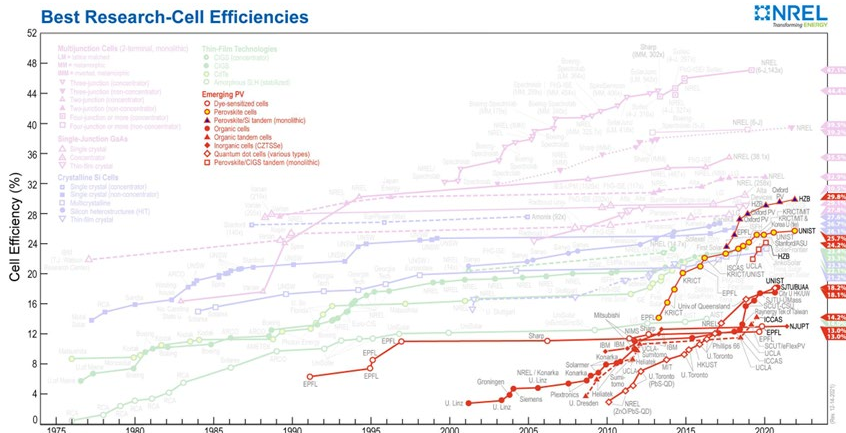


Figure 2. A) perovskite structure (Reproduced from Ref. 12 with permission from John Wiley and Sons),¹² B) Schematic diagram of the working mechanism of PSCs (Reproduced from Ref. 13 with permission from the Royal Society of Chemistry).¹³

Since the early work of Miyasaka in 2009,¹¹ the research on perovskite solar cells have grown rapidly as the power conversion efficiency (PCE) raised from 3.9% to 10% using a solid-state HTM in PSCs,^{14,15} reaching 25.6% in 2021¹⁶ approaching the highest values obtained by single-crystalline silicon solar cells as shown in (Figure 3) . PSCs have a potential to be the PV

technology of the future due to its high performance and the cost-effective solution based process used in perovskite solar cells fabrication.

A)



B)

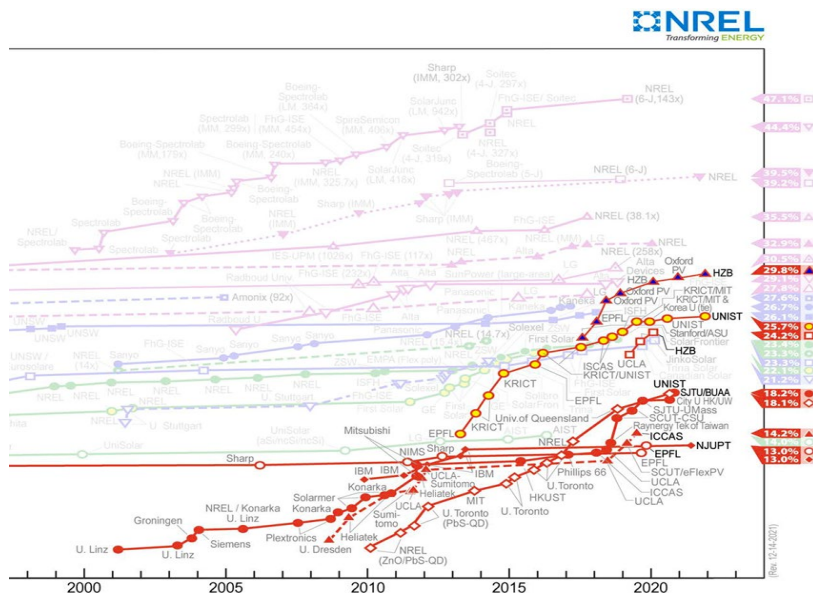


Figure 3. Emerging Photovoltaic efficiencies:¹⁷ A) Full diagram and B) expansion of the relevant section. Note: Perovskite Solar Cells are represented by the yellow-filled circle (Modified from Ref. 17).

1.2.2 Architectures and building blocks of Perovskites Solar Cells

Mainly we have two architecture types of PSCs (Figure. 4), the first one is the regular *n-i-p* (negative-intrinsic-positive) and the second one is the inverted *p-i-n* (positive-intrinsic-negative). Both of them can be mesoporous or planar. In the first one a n-type electron transport layer (made of an Electron Transporting Material, ETM e.g., TiO₂, SnO₂, etc.) is lying at the bottom of device structure where it is deposited onto a conductive glass (FTO), followed by the active layer (perovskite) and finally by the p-type hole transport layer (made of a Hole Transporting Material, HTM: e.g., Spiro-OMeTAD, P3HT, PTAA, etc.) and finally by a metal electrode on the top. As far as the second one is concerned, the inverted *p-i-n* architecture, the hole transport layer is laying over the glass, at the bottom of the solar cell, followed by the perovskite active material, by the electron transport layer and, finally, by the metal electrode.¹⁸

1.2.3 Mesoscopic and planar structures

1.2.3.1 Mesoscopic structure

In case of mesoscopic structure, the perovskite crystals are filling the pores into the mesoporous n-type metal oxide (e.g. TiO₂, SnO₂, Al₂O₃, etc.) and covering it. The mesoscopic structure has a larger interface at the perovskite/HTM or

perovskite/ETM interface in normal and inverted structures and the mesoporous scaffold provides an efficient extraction of charges.¹⁸ Adding to that, the performance of the perovskite device can be enhanced by changing the mesoporous ETL. In the case of the first cell, made using mesoporous TiO₂ as n-type ETM layer and Spiro-OMeTAD as HTM layer, the efficiency was around 8% using 300 nm thickness of a perovskite layer of methylammonium lead iodide chloride (CH₃NH₃PbI₂Cl) halide, but when Al₂O₃ was used as a mesoporous oxide the PCE increased to 10% as Al₂O₃ acts as an insulator due to its wide band gap of 7.00 and 7.6 eV for am- and γ - Al₂O₃, respectively,¹⁹ and cannot transport the electrons due to energy level mismatch with the CB of perovskite active layer. In fact, Al₂O₃ supports only the crystallization of the perovskite, and since in this kind of solar cells there is no n-type oxide the devices are not sensitized solar cells as upon excitation of the electron from the VB to the conduction band we have only the movement of holes to the HTM.¹⁵ Also, the current density of PSC devices can be enhanced by using a mixture of larger particles of TiO₂-ZrO₂ in the mesoporous layer can increase the light scattering.²⁰ Mesoscopic based PSC devices have been investigated, reaching efficiencies of more than 25%. Devices based on the mesoscopic structure show negligible hysteresis (fluctuations in current-voltage response in forward and reverse directions) in comparison with planar architecture due to the large area

contact between the perovskite active layer and the mesoporous resulting in efficient electron transfer and separation.^{15,21} However, TiO₂ have some drawbacks as it has low electron mobility, can show charge accumulation at the TiO₂/perovskite interface because of its photocatalytic activity and the presence of trap states, which lower the stability of the PSC devices under UV irradiation.²² Also, the production of the TiO₂ layer needs sintering at very high temperatures (around 500 °C), which results in the degradation of the polymeric materials (e.g. polyethylene naphthalate, polyethylene terephthalate) of flexible solar cells making the use of TiO₂ unsuitable in flexible optoelectronic devices. Because of these disadvantages many efforts have been done to replace the mesoporous TiO₂ layer, TiO₂ nanowires were synthesized using atomic layer deposition, to enhance the electron collection and the absorption coefficient.²³ Besides that, SnO₂ based mesoporous materials which have a valence band (VB) of -7.94 eV that is deeper than the -7.2 eV of the TiO₂ ETL, were explored and developed due to their excellent properties as SnO₂ has a 100 times higher electron mobility, wider band gap around 4 eV and deeper conduction band (CB) of -4.23 eV than TiO₂, which has a conduction band placed at -4.05 eV.^{22,24} When the mesoporous SnO₂ ETL is treated with TiCl₄, the device PCE jumps at 8.54%, higher than the mesoporous TiO₂ ETL, for which PCE was only 7.20%.²⁵ In conclusion, introducing mesoporous ETL in PSC based devices provides improved control of the

morphology of the device, negligible hysteresis and high performance and reproducibility.^{26,27} Still, the mesoporous layer has some drawbacks, as without it the device structure is simplified, and the efforts and device production costs are reduced.²⁸

1.2.3.2 Planar structure

The structure of the PSC planar architecture is shown in Figure 4. A planar PSC device was fabricated initially by Snaith et al.¹⁵ with a compact ETL (TiO₂), a 150 nm perovskite active layer (MAPbI_{3-x}Cl_x) and a HTL layer (based on Spiro-OMeTAD) giving a PCE of 1.8%. After controlling the processing condition, film thickness, atmosphere and annealing temperature, the morphology of PSC device was optimized giving a high photocurrent when a complete surface coverage was obtained, achieving a PCE of 11.4% with a short-circuit current density (J_{sc}) of 20.30 mA/cm² and an open-circuit voltage (V_{oc}) of 0.89 V.²⁷ Furthermore, the use of highly uniform vapour deposited layer perovskite active layer, while ETL (TiO₂) and HTL (Spiro-OMeTAD) layers were deposited by solution-based processes, improved the performance of planar PSC devices leading to PCE over 15% with V_{oc} of 1.07 V which indicates that it not always necessary to use complex nanostructures to obtain high performances of PSC devices.²⁹ It was found that the introduction of a hydrophilic buffer layer of PMMA (Poly(methyl methacrylate)), which was treated by a homemade ozone

plasma generator for the hydrophilic grafting (HGG) onto the non-wetting HTMs, can dramatically improve PCE to 20.75% with very high air stability, excellent reproducibility and imperceptible hysteresis.³⁰ From the commercialization point of view, the inverted planar (*p-i-n*) structure have a high potential for large-scale fabrication because of its moderate processing temperature, around 100 °C, good air stability, low cost, and short production time.^{28,31}

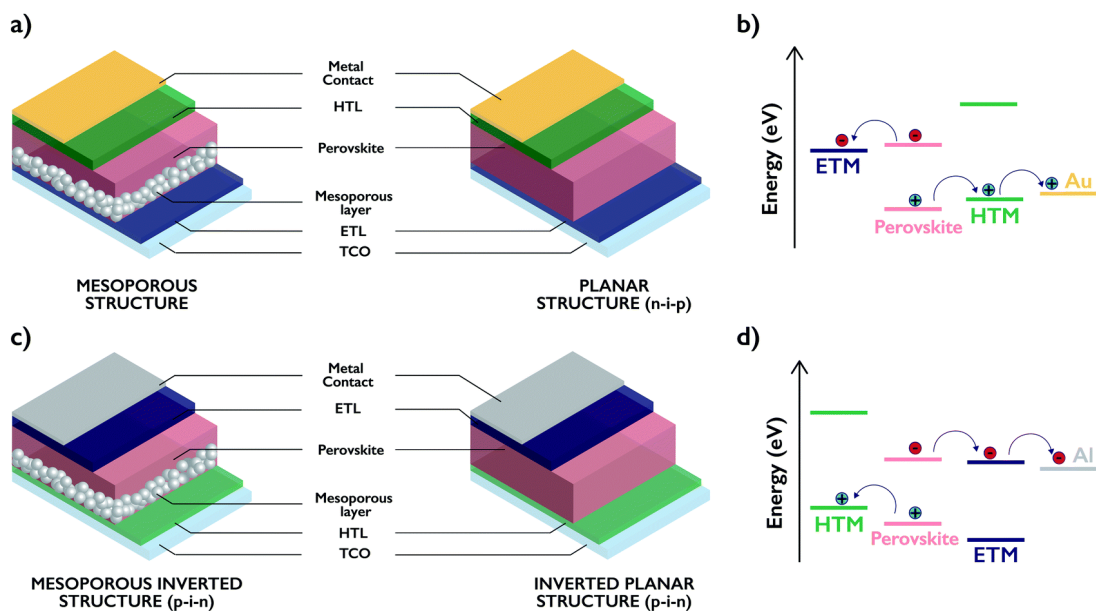


Figure 4. Schematic illustration of the most common device architecture of PSCs: (a) (n-i-p) mesoporous and planar structures. (b) Energy diagram of the different components of a conventional PSC. (c) Inverted (p-i-n) mesoporous and planar structures. (d) Energy diagram of the different components of an inverted PSC (Reproduced from Ref. 32 with permission from the Royal Society of Chemistry).³²

2 BUILDING COMPONENTS OF PSCS

2.1 An Overview

Beside the perovskite active layer, the main parts of the perovskite solar cell device are the counter electrode (CE), the electron transporting layer (ETL) and the hole transporting layer (HTL). The counter electrode is important for the device performance and stability by collecting holes. Generally, noble and transition metals such as Ni, Mo, Cu, Cr, Au and Ag are used as counter electrode. The counter electrode has to collect and extract the charge carriers efficiently from the perovskite sensitizer with the help of HTL and ETL. Thus, the CE should have high electric conductivity and aligned work function. For example, the Fermi level of the counter electrode must be above the valence band and below the conduction band edge of the perovskite active layer.³³

It was reported that the CE is one of the main causes of cell degradation, which can occur due to metal migration into the HTM layer or the corrosion of the CE if and when it comes in contact with the perovskite layer. Lately, in a device with the FTO/TiO₂/MAPbI₃/HTM/Au configuration it was reported that Au diffuses into the perovskite layer and dramatically decreases the solar cell performance.³⁴

To overcome this issue a buffer interlayer was added between the CE and the perovskite layer but it provided protection for a short-time frame. Until now, the

need for long-term stability still remains, as the perovskite active layer tends to diffuse under continuous light irradiation, which degrades the PSC devices. To increase the long-term stability, new electrodes are used.^{34–38} It was reported that copper (Cu) electrodes are stable for many years even in direct contact with the perovskite active layer and can replace the Au electrodes because of the high resistance to corrosion of Cu even in presence of harsh halogens and non-oxidizing acids (e.g. HBr, HI, HCl). Due to the absence of the interaction between the Cu counter electrode and the perovskite after a long-term under sun irradiation and thermal annealing, the Cu did not migrate nor diffuse into the perovskite layer.³⁶ It is so clear that it is important to obtain a long-term stable CE for constructing a stable PSC device.

Electron transporting materials (ETMs) have an important role in perovskite solar cells (PSCs). The main role of the ETM is to extract and transport the perovskite's photogenerated electrons while blocking the holes.^{39–41}

Also, the homogenous and uniform ETL can increase the air stability of the solar cell device by blocking the diffusion of oxygen, metal particles and moisture.⁴² For an ETM to be ideal it should have these properties: *i*) excellent electron affinity and tuned energy levels with the perovskite active layer to increase charge separation and block recombination; *ii*) excellent electron mobility, which helps extracting and

transport the electrons; *iii*) chemical stability to prevent any interaction with the perovskite or the anode; *iv*) facial processability and low-cost; *v*) hydrophobicity, to block moisture infiltration into the perovskite.^{43–45} The most common ETMs used in perovskite devices are inorganic metal oxides (e.g. TiO₂, ZnO, SnO₂, WO₃, Zn₂SnO₄ and SrTiO₃), while also organic compounds are used, e.g., fullerene derivatives.^{43,46–}

⁵¹ The most highly performing devices are based on mesoporous ETMs as they give large surface area and maximize the loading of the absorber, that leads to low recombination due to continuous electron flow. Beside fullerene, many other organic molecules were used as ETM in high-performing PSCs. These are small molecules, polymers and ionic liquids, e.g. based on perylene derivatives because of their high chemical stability, thermal stability and high electron mobility. The non-fullerene organic ETMs have some advantages over the fullerene ones, as they have easily tunable chemical structure, high synthetic yield, facial processing and it is highly possible to decrease their cost.^{52–55} Bai et al.⁵⁶ have fabricated a cell with a PCE of 19.5% and maintaining 90% of initial performance using an interesting designing of ETM in which a cross-linkable silanol bound used to the carboxylic acid group of a fullerene, which was decorated with a hydrophobic CF₃ group, to increase the water resistance. To resolve the issue of stability, besides the design of new high-performing ETMs, many various strategies have been such as, the use

fulleropyrrolidinium iodide (bis-C₆₀) and amine-functionalized DMAP-C₆₀ layers to prevent oxygen or moisture and at the same time giving high performing devices.^{56–61} Although a lot of efforts have been done for the development of new strategies to produce efficient ETMs, there are still challenges to be addressed. One of the challenges is the use of SnO₂ as ETL. Tin oxide is known as an excellent ETM which can provide devices with high efficiencies, but the annealing temperature can affect the film characteristics and thus its effect on the film characterization and the device performance still needs to be explored.⁴⁷

2.2 Hole-transporting materials (HTMs)

HTMs play an important role when we are looking for highly performing and long-term stable perovskite solar cell devices. The HTM is a “must” in all PSCs devices as it is responsible for efficient extraction and transport of holes from the perovskite active layer to the metal electrode. Besides, it protects the perovskite layer from the diffusion of the metal from the electrodes (Au, Ag and Al).^{62,63} HTMs work on the reduction of the charge recombination at the Perovskite/HTM interface covering the perovskite surface uniformly, as the HTM should have a higher LUMO energy level than the conduction band (CB) of the perovskite to prevent the electron back transfer (charge recombination). Besides that, the HTMs improve the stability of the

perovskite devices by surface passivation via ionic, covalent, and non-covalent interactions.^{64–67} HTMs can act as a barrier to avoid the entrance of oxygen and/or moisture which protects the perovskite active layer from the ambient-induced degradation, leading to the improvement of long-term stability of the device.⁶⁸

The Ideal HTM for a perovskite solar cell should follow several requirements: *i)* tunable energy levels; *ii)* high hole mobility; *iii)* soluble in the common organic solvents used for its deposition; *iv)* hydrophobic; *v)* highly conductive; *vi)* low-cost; *vii)* chemical and thermal stability; *viii)* transparency in the visible region for enabling the highest light absorbance by the perovskite active layer.¹³ Also, easily attainable, biodegradable and environmentally friendly HTMs are required to obtain green solar cell devices.^{69–71} The polymeric PEDOT:PSS (Figure 9) HTM is a commonly used material, which gave low efficiency of 3.9% in a planar device due to the un-optimized absorber layer thickness (< 50 nm) and the modest characteristics of the Perovskite/HTM interface (MAPbI₃). By using perfluorinated isomers to tune the HOMO energy level of poly(3,4-ethylenedioxythiophene) polystyrene sulfonate (PEDOT:PSS) from 4.86 eV to 5.4 eV the device performance was increased to 11.7%.⁷² The PEDOT:PSS has many pro, as affordability, facile synthesis and it has been investigated in organic electronics but it still have some cons, like *i)* its acidity which can result an issue for the electrodes; *ii)* its hydrophilic and hygroscopic nature

lead to reduction of device stability and iii) the molecular weight batch from batch variation. Currently the most used HTM in perovskite solar cells is Spiro-OMeTAD (2,2',7,7'-tetrakis[N,N-di(4-methoxyphenyl)amino]-9,9'-spirobifluorene).⁷³ HTMs can be divided into two main categories: 1) Inorganic HTMs and 2) Organic HTMs.

2.2.1 Inorganic HTMs

Inorganic hole transporting materials have the advantage of wide band gap and high hole mobility. The energy alignment between the HOMO level of the HTM and the VB of the perovskite is an important factor for device high efficiency. For this reason, the energy levels of inorganic HTMs in PSCs are shown in Figure 5. Cu based HTMs like CuSCN, CuI and CuO_x have been used extensively because of their band matching and good efficiency. Oxides such as NiO_x, MoO_x and MoO₃ are a very promising HTMs as they have very good and reproducible results in PSCs devices. MoO₃ in inverted structure has showed an efficiency of 18.2%, which is an outstanding achievement.⁷⁴

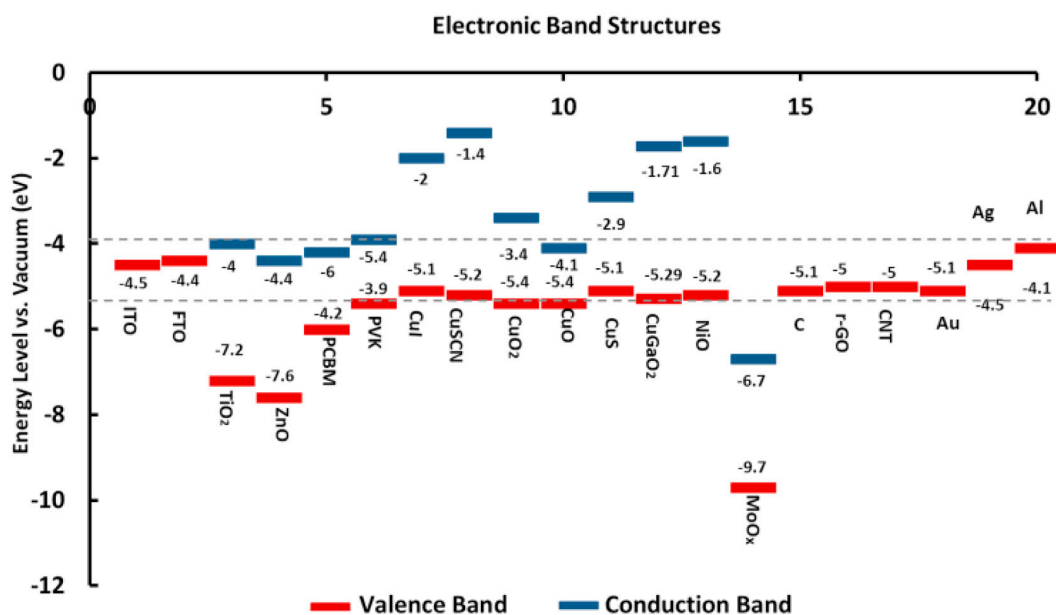


Figure 5. The energy levels alignment of inorganic HTMs in PSCs (Reproduced from Ref. 74 with permission from Elsevier).⁷⁴

2.2.2 Organic HTMs

The organic HTMs can be divided into 2 major classes: small molecule^{18,75} and polymeric HTMs.^{75,76}

2.2.2.1 Small molecules

Small-molecules HTMs are interesting since they can be produced and easily purified by assembling different moieties, containing Donor and/or Acceptor functional groups tailoring and adapting their properties to the specific perovskite needs, based on the molecular structure and on the solid-state packing state.⁷⁷ In fact, the hole mobility value of pristine organic HTMs, for both small molecules and polymers, is relatively low, in the range 10^{-4} – 10^{-6} $\text{cm}^2 \text{V}^{-1} \text{S}^{-1}$. For a better performance in a PSC, a HTM should have a hole mobility of at least 10^{-4} $\text{cm}^2 \text{V}^{-1} \text{s}^{-1}$; ⁷⁸ so, the required hole mobility can be usually obtained by doping.⁷⁹

Here we are presenting some of the most used units for organic small molecules HTMs.

2.2.2.1.1 Spirobifluorene

The bulky twisted spirobifluorene-based Spiro-OMeTAD (Figure 6a) is the most studied HTMs small molecule and showed one of the best efficiency performances

since its first use was in 1998.⁸⁰ At the beginning it was used for DSSCs and gave an efficiency of 0.74% which was improved by the use of dopants 4-*tert*-butylpyridine (t-BP) and lithium bis(trifluoromethanesulfonyl)imide (LiTFSI), achieving a PCE of 2.56%.⁸¹ Then the efficiency was improved to 7.2% by adding a Co^{III} complex (FK102) dopant.⁸² Although the first 2 dopants are still used to improve the hole mobility and V_{oc} , various Co^{III} complexes were examined to enhance the hole mobility of the Spiro-OMeTAD. A PCE of 19% was obtained by using a mixed perovskite having the composition $(\text{FAPbI}_3)_{0.85}(\text{MAPbBr}_3)_{0.15}$.⁸³ Another mixed Perovskite absorber prepared through the optimization of the ratio of lead iodide/formamidinium iodide and excess of PbI_2 , gave an efficiency of 20.8 % in the mesoscopic configuration using doped Spiro-OMeTAD.⁸⁴ As a matter of fact, the presence of the methoxy groups (-OCH₃) in the HTM is responsible for tuning the HOMO level of the molecule, beside the important role they play in attaching the molecule to the perovskite layer. To notice this behavior, Seok et al.⁸⁵ studied the electric and optical properties of Spiro-OMeTAD having methoxy groups in para- (pp-OMe, Figure. 6b), ortho- (po-OMe, Figure. 6 d) and meta- (pm-OMe, Figure. 6c) positions. The methoxy unit has electron withdrawing effects due to the inductive effect, nevertheless, as Hammett demonstrated, depending on the substitution pattern it can behave as electron-donating (if resonance can act for it) or withdrawing unit in the para- and meta

position respectively, while in the *ortho*-position it has a more important steric effect.

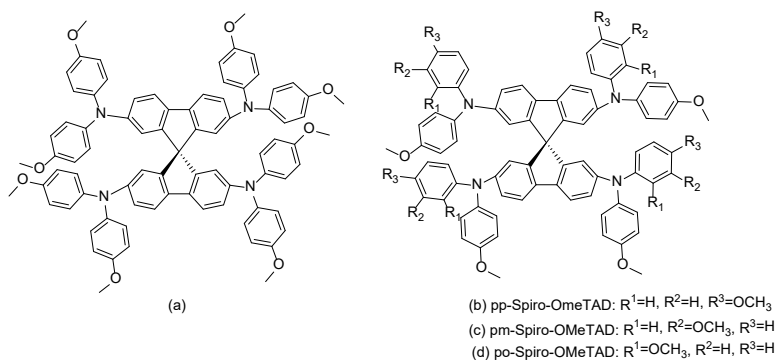


Figure 6. Structures of Spiro-OMeTAD HTMs.

2.2.2.1.2 Thiophenes

They present a striking class of compounds, which were used intensively as building units for organic semiconductors and were widely studied due to their optoelectronic properties and their high hole mobility which is an attractive property for HTMs.⁷⁸ Nazeeruddin et al.⁶⁶ obtained a PCE of 20.2% using a thiophene based HTM (Figure 7) with mixed perovskite (containing mixed MA and FA cations, with I and Br anions).

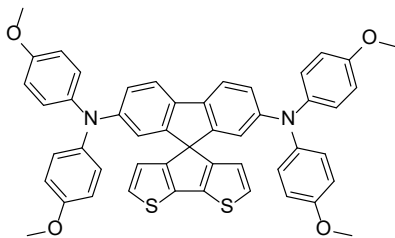


Figure 7. Structure of a thiophene based HTM.

2.2.2.1.3 Triphenylamines

Triphenylamine (TPA) unit is one of the most used building blocks in organic electronics. Because of its propeller-like structure, it gives rise to non-planar geometry that control the packing of the material in solid state and influence the optoelectronic properties of the TPA based material.⁸⁶ Many star-shaped HTMs based on TPA unit were designed, for example, Ko et al., (Figure 8 (a) and (b)), with a diphenyl ethenyl side arm acting as acceptor,⁸⁷ giving efficiencies of 9 and 11.8%, respectively, in MAPbI₃ based devices.

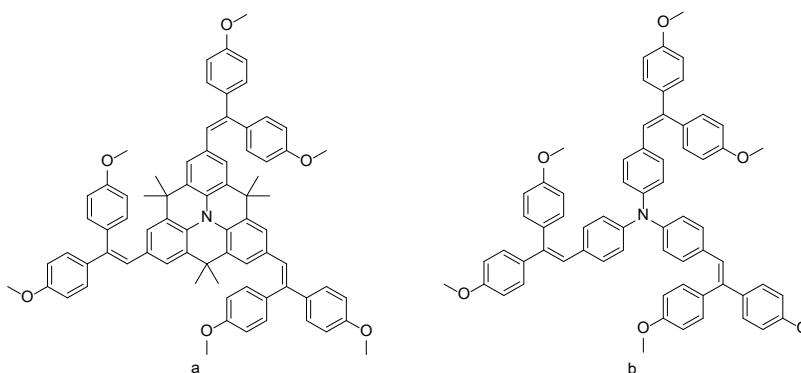


Figure 8. Structure of triphenylamine based HTMs: a) “TPA-MeOPh”; b) “FA-MeOPh”.

2.2.2.2 Polymers

Conjugated polymers have been used for many years in organic electronics, like OFET,⁸⁸ OPV,⁸⁹ OLED,⁹⁰ etc. HTMs based on polymers can be divided into three main types: i) homopolymers; ii) copolymers and iii) D-A (Donor-Acceptor) copolymers. As a matter of fact, homopolymers have been used in large scale because of their facile synthesis and availability.⁹¹ Polymeric HTMs have higher stability comparing to molecular HTMs (normally known as “small molecules”), which in general results in more stable devices.⁹² Even if small molecules offer a defined molecular weight and structure with high synthetic reproducibility and easy purification, on the other hand, polymers often have better properties in terms of mechanical and thermal stability, higher hole mobilities and processability.^{93–96} High device efficiencies exceeding 20% can be obtained using low-cost and air stable conjugated polymers by replacing the hygroscopic and expensive molecular HTM, such as Spiro-OMeTAD.^{21,97,98} Currently, the most studied conjugated polymers as HTMs in PSCs are the polymers based on Polytriarylamine (PTAA), P3HT and PEDOT:PSS that are shown in Figure 9.⁶⁸

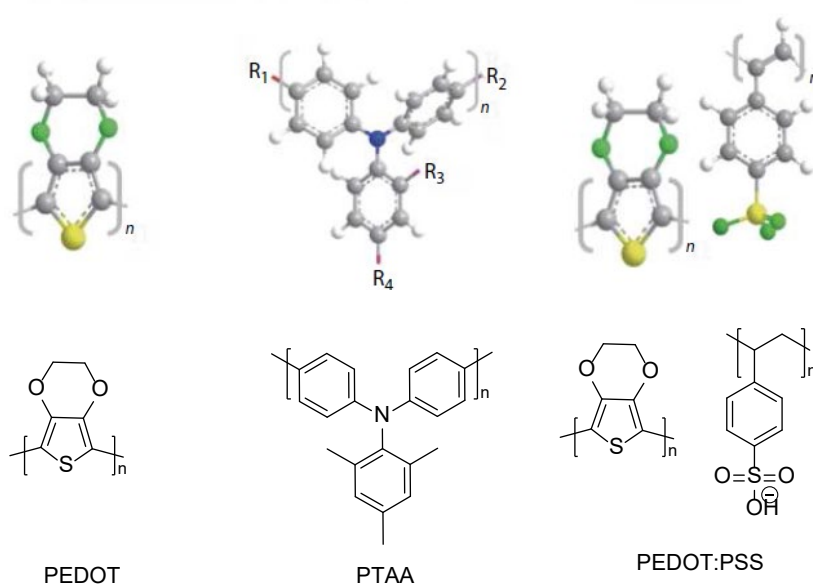


Figure 9. Structure of the most used polymers as HTMs.

2.2.2.2.1 Polytriarylamines (PTAA) based HTMs

As a result of the high hole mobility induced by the triphenylamine unit, PTAA is an important class of hole transporting materials in organic photovoltaics.⁹⁹ The PTAA is a commercially available polymer, in which the 2,4,6-trimethylaniline is linked to a biphenyl moiety. Its own properties are excellent and made it the standard reference for the polymer-based PSC efficiency. PTAA-like polymers have high hole mobility of (10^{-2} - 10^{-3} $\text{cm}^2\text{V}^{-1}\text{s}^{-1}$) under doping conditions, strong interaction with the perovskite and low thermal degradation. PTAA-based polymers are considered as efficient HTMs.¹⁰⁰ Besides the effectiveness of PTAA polymers as HTMs, they have been used in different perovskite solar cell based devices to achieve

long-term stability because of the presence of amino group nitrogen in the backbone of PTAA based polymers which prevent the delocalization of electrons between adjacent phenyl units and decreases the conjugation length (cross conjugation), thus resulting into an anti-oxidative ability and thus a higher stability under ambient conditions.^{68,101}

2.2.2.2.2 P3HT-based HTMs

P3HT is the most popular among thiophene-based polymers, being a conjugated polymer and showing a good solubility, high stability, and a relatively high hole mobility.¹⁰² P3HT based polymers are good candidates for PSCs application, even though, in the primary work the performance of a device having P3HT HTMs was low, mainly due to low hole mobility $3 \times 10^{-4} \text{ cm}^2 \text{ V}^{-1} \text{ s}^{-1}$ and the fast recombination behavior at HTM/perovskite interface.^{101,103}

The first device based on P3HT as HTM and $\text{CH}_3\text{NH}_3\text{PbBr}_3$ as perovskite active layer obtained a very low PCE of 0.52%.¹⁰⁴ Although, the improvements, still the low hole mobility of P3HT is a big issue for the efficiency of PSCs devices which could be partially resolved using LiTFSI and or *t*-BP.^{105–107} The efficiency of PSC was increased from 5.6% to 14.2% when Li-TFS and *t*-BP were added to the HTM as dopants, Li-TFSI/*t*-BP additives demonstrated better hole mobility than the P3HT without additives because of the extra hole transport by Li-TFSI/*t*-BP mediated hole

conduction.¹⁰⁵ Recently, Seo and others⁹⁷ reported a double-layered halide structure (DHA) in PSCs using P3HT as HTM obtaining a certified PCE of 22.7% in the undoped state. The introduction of the wide band gap halide (WBH) layer into the perovskite structure effectively reduced the charge recombination at the HTM/perovskite interface and increased the self-assembly of P3HT, resulting in the remarkable improvement in the obtained PCE. In addition, the DHA-based PSCs showed good long-term stability, preserving nearly 80% of its initial efficiency after 1008 h at relative humidity of 85% without encapsulating and 95% of its initial efficiency for 1370 h under sun irradiation after encapsulation.

The effect of regioregularity (RR) and molecular weight on the performance of and stability of PSCs was investigated and it was found that the higher the molecular weight of the P3HT, the higher efficiency of the devices and that a P3HT with lower RR will form a film with a face-on arrangement onto perovskite, thus enhancing the cell efficiency.¹⁰⁸

2.2.2.2.3 PEDOT:PSS- based HTMs

PEDOT:PSS polymers have been widely used as HTMs in inverted PSCs as it has high work function, excellent conductivity and high transparency.¹⁰⁹ As we mentioned before PEDOT is one of the first HTMs used for perovskite solar cells. Further development in the crystallinity and grain size of the perovskite layer using solvent

annealing, moisture-assisted film growth and single-step spin-coating methods resulted in PSC devices with efficiencies of 15.6%, 17.1% and 18.1% respectively.^{110–}

112

2.2.3 Chemical Doping

Doping is an important tool to increase the efficiency of devices in organic electronic by increasing the conductivity, reducing the ohmic loss in charge transport parts and injection barriers at the interface with the electrodes, and controlling the energy levels.^{113,114} P-dopants in organic semiconductors work by adding mobile charge carriers which are created by electron acceptors, that remove electrons from the HOMO to generate holes in the HTM (Figure 10).^{115,116} Various numbers of p-type semiconductors have been introduced today and in Figure 11 the structures of the most used ones are shown. Moreover, the use of dopants is giving serious problems for the cell stability because of the sophisticated oxidation procedure and undesired ion migration. For example, the hygroscopic character of LiTFSI leads to the recruiting of moisture from the air and the formation of pinholes into the HTM layer, resulting in the chemical degradation of the perovskite layer, which negatively affects the stability of the solar cell device.^{49,117} Also, tBP can interact with perovskite active layer and could dissolve it.^{118,119}

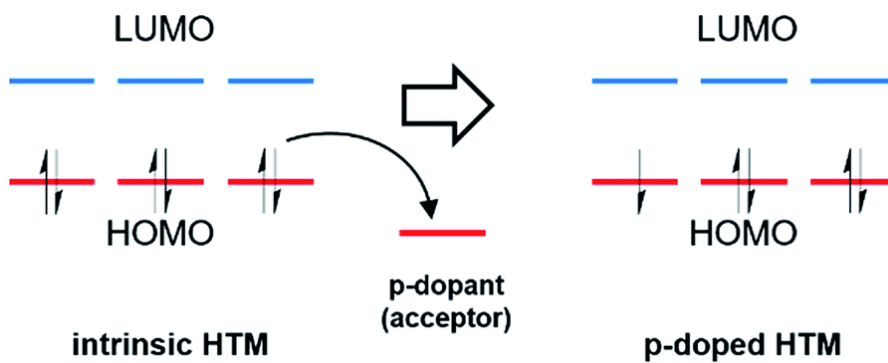


Figure 10. Schematic illustration of the molecular p-type doping mechanism, where the dopant is an acceptor.

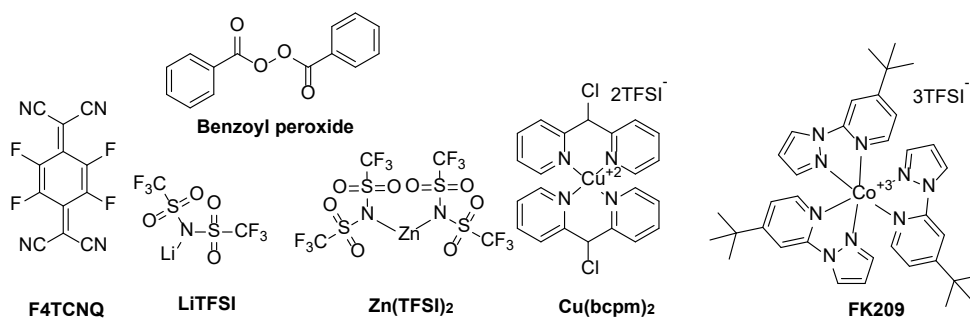


Figure 11. Structure of most used p-dopants.

3 PHENOTHIAZINE

3.1 Phenothiazine as a building block in organic semiconductors

Since the beginning of organic photovoltaics, various numbers of small molecules and polymers were produced based on different building blocks having electron donating or withdrawing properties. Most of them have a rigid coplanar structure which improves electron delocalization and enhance co-facial π - π stacking in the solid phase state, thus increasing the charge transport in the devices. However, this often is accompanied with higher order crystallinity and aggregation, which reduce the solubility in the processing solvents and negatively affect the charge mobility, leading to lower performance of the photovoltaics device.^{120,121} To solve this problem not-planar scaffolds are needed to be introduced which can give reasonable conformational twist and less coplanar conjugated backbone. Furthermore, the presence of a not-planar scaffold can introduce useful properties which are critical for high performing Organic Solar Cells (OSCs) such as solution-processability, film-morphology, and desired aggregation.

Phenothiazine (PTZ) is well known as an electron-rich not-planar heterocyclic compound which contains sulfur and nitrogen.¹²² As showing in Figure 12 the phenylene rings of PTZ have the aspect angle of 21° as they are folded along the S...N

vector. Phenothiazine is well known as a building unit in dye synthesized solar cells, organic light-emitting diodes and organic thin-film transistors due to its ability to decrease molecular aggregation because of the non-planar butterfly conformation together with the good thermal and electrochemical properties, easy energy levels tunability, commercial availability and low price.¹²² Due to the low hole bulk mobilities and its non-planar geometry, phenothiazine building units have not been fully explored as a building blocks for organic solar cells.¹²³

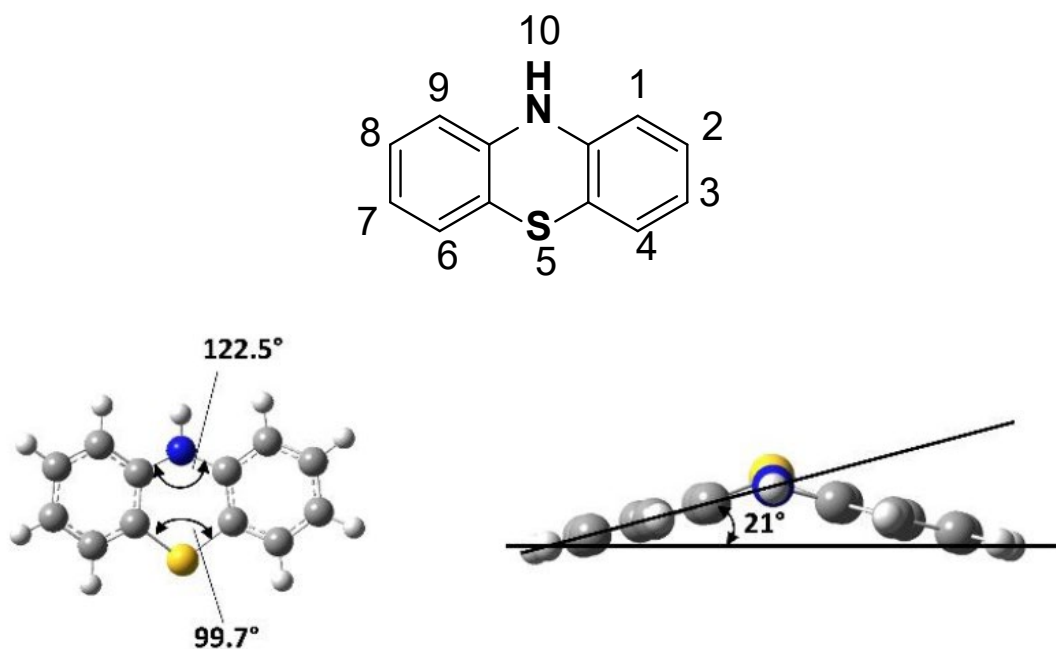
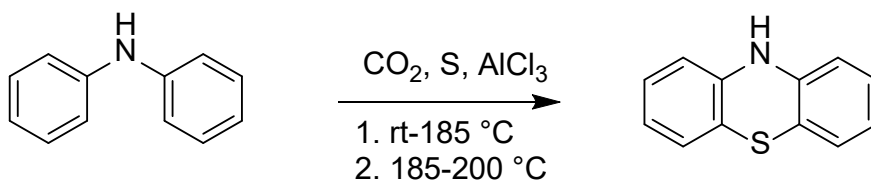


Figure 12. Chemical structure of phenothiazine and top and side view of DFT optimized geometry structure.

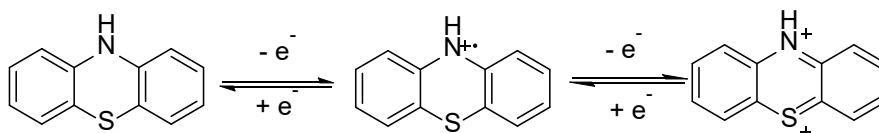


Scheme. 1 Synthesis of phenothiazine.¹²²

As shown in Scheme 1 phenothiazine is usually prepared by reacting sulfur with diphenylamine in presence of AlCl_3 .¹²² One of the most important advantages of phenothiazine molecule that it can be functionalized with various substituents at position C-2, C-3, C-7, C-8 and N-10 leading to the tuning of its electrochemical and photo-physical properties. In most cases, the N-10 position is decorated for solubility processing proposes by using alkyl, aryl or aralkyl. Commonly, positions at carbon C-3 and C-7 are the most used for the substitution with electron withdrawing or electron donating groups, to tune the molecular properties and to afford the desired semiconductors. Typically, electrophilic substitution reactions such as halogenation and formylation take place at positions C-3, C-7. Phenothiazine is mono- or di-halogenated at these positions to generate aryl halides which are a fundamental reagent in palladium-catalyzed coupling reactions (Stille, Suzuki, Heck or Buchwald) with aryl-tin, aryl-boron, aryl-alkene or amine respectively. In addition to that, PTZ is an aromatic S-heterocycle having a sulfur which can show different oxidation states such as (sulfide, sulfoxide, and sulfone) which could be achieved easily through oxidation and reduction reactions.

3.2 Properties of Phenothiazine derivatives

10H-phenothiazine is an electron rich heterocyclic compound, containing sulfur and nitrogen. Phenothiazine has the ability to give a stable radical cation with deep color because it undergoes a reversible one-electron oxidation process with low potentials.¹²⁴ Also, a dicationic species can be obtained by a further one-electron oxidation (see Scheme 2).¹²⁵ Cyclovoltammetry is used to measure both the oxidation steps related to both one and two electron transfer ($E_{1/2}^{0/+1} = 270$ mV and $E_{1/2}^{+1/+2} = 770$ mV)¹²⁶, and the presence of the radical cation can be detected by UV-Vis¹²⁷, EPR¹²⁸ and Raman spectroscopy.¹²⁹ As a matter of fact, phenothiazine based compounds have promising applications in material science as electron donating units in electronically conducting charge-transfer materials¹³⁰ and as electrophoretic sensors in supramolecular systems for photoinduced electron transfer (PET).^{131–133} Due to their low oxidation potential, phenothiazines are capable of acting as electron donors in fluorescent donor-acceptor chromophores, which are very useful for organic light-emitting diodes applications.^{134,135} and for electrooptical and nonlinear effect base applications.¹³⁶



Scheme 2. Two steps one-electron oxidation of PTZ and corresponding radical cation and dication.

3.2.1 Phenothiazine Based Hole Transporting Materials for PSCs

To have a better performance of the perovskite solar cells, the properties of the hole transporting materials should be improved. Therefore, many studies were performed on the HTMs and perovskite active layer in view of obtaining stable and commercially available perovskite solar cells.¹³⁷ HTMs are an important part for the PSCs to improve the efficiency and stability of the devices.¹³⁸

To commercialize the PSCs, a lot of research groups are working on the development and enhancement of the HTMs properties. Recently, phenothiazine based HTMs have brought the attention of many researchers.

In 2018, Xiaojuan Zhao et al.¹³⁹ have reported three new HTMs based on dithienopyrrolobenzothiadiazole (DTPBT) core, and terminated with triphenylamine (TPA), phenothiazine (PTZ) and octyloxy-triphenylamine ($C_8H_{13}O$ -TPA), giving the HZ1, HZ2 and HZ3 HTMs respectively (Figure 13). The highest performance was shown by HZ2, the HTM bearing phenothiazine as an end group, with a PCE of 14.2 % (which is close to the PCE of the state-of-the-art Spiro-OMeTAD in the same conditions, 14.9 %) , J_{sc} of 20.43 mA cm^{-2} , V_{oc} of 1.026 V and FF of 68% and having a better stability of 280 h without encapsulation under 20% relative humidity. The HZ1 and HZ3 HTMs showed efficiencies of 7% and 10.2% respectively.¹³⁹

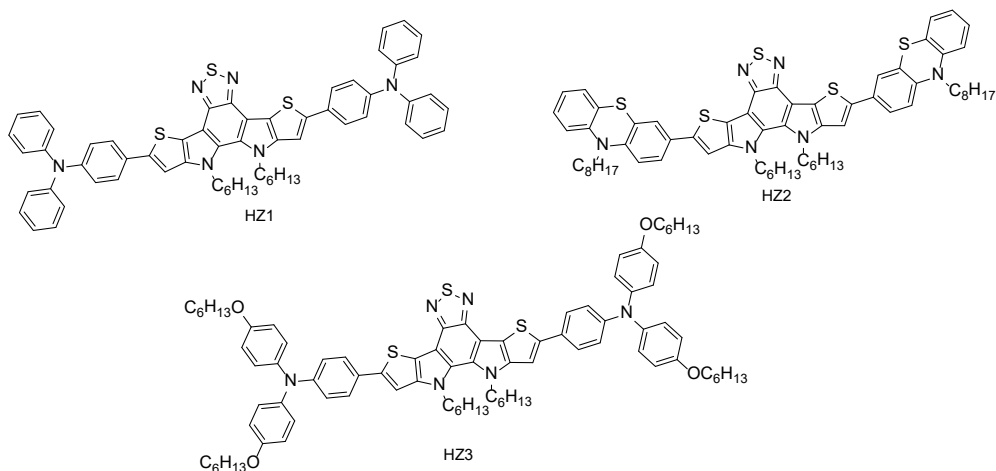


Figure 13. Chemical structures of the HZ1, HZ2 and HZ3 HTMs.¹³⁹

In 2018, Fei Zhang et al.¹⁴⁰ reported three new HTMs based on phenothiazine core attached through double bonds (conjugation bridge) with the 4,4'-dimethyltriphenylamine, N-ethylcarbazole (linked at its carbon in position 3) and 4,4'-dimethoxytriphenylamine groups (Figure 14). The HTMs Z28, Z29 and Z30 showed the HOMO energy level values of -5.39 eV, -5.44 eV, -5.27 eV, respectively, while the perovskite active layer has a VB energy level of -5.5 eV. The space charge limited current method was used to measure the hole mobility values of the new HTMs giving $6.18 \times 10^{-5} \text{ cm}^2\text{V}^{-1}\text{s}^{-1}$ for Z28, $6.82 \times 10^{-6} \text{ cm}^2\text{V}^{-1}\text{s}^{-1}$ for Z29 and $6.70 \times 10^{-5} \text{ cm}^2\text{V}^{-1}\text{s}^{-1}$ for Z30. Z30 gave the highest PCE of 19.17% (with spiro-OMeTAD showing a PCE of 19.66% in the same conditions) and J_{sc} of 23.53 mA cm^{-2} , V_{oc} of 1.114 V and FF of 0.73%, also demonstrating that this HTM has a higher stability than that of Z28 and Z29 under ambient air and relative humidity of 40% in the dark without

encapsulation (1108 h) and under continuous sunlight soaking without encapsulation (600 h). The Z28 and Z29 HTMs, however, gave PCE of 17.77% and 14.65% respectively, showing that the use of the phenothiazine as a core scaffold is undoubtedly promising.

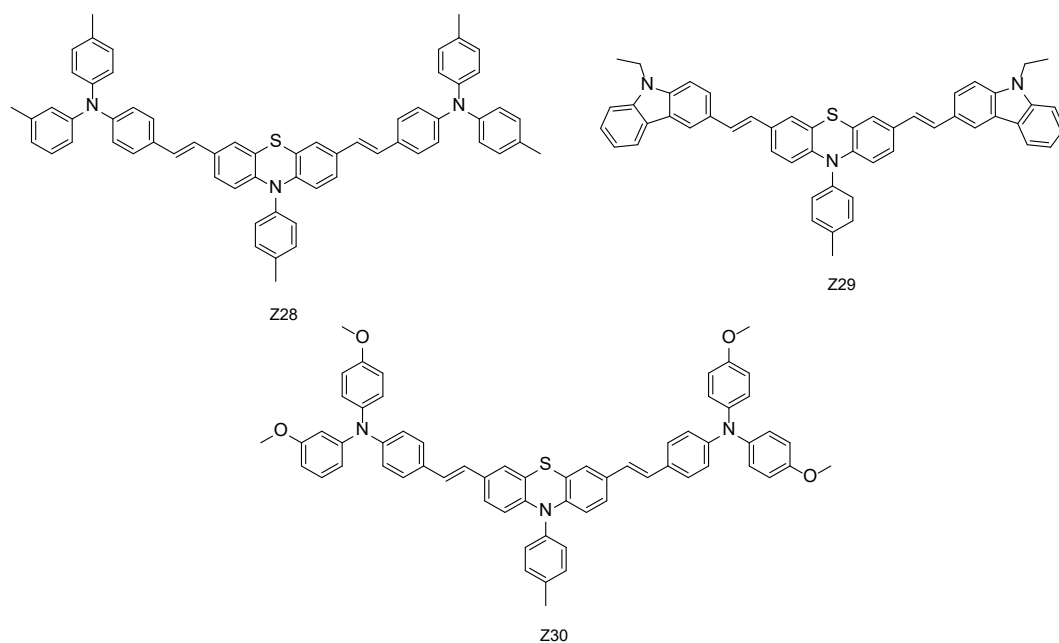


Figure 14. Chemical structures of the Z28, Z29 and Z30 HTMs.¹⁴⁰

In 2017, Grisorio et al.¹⁴¹ have synthesized two new HTMs based on Phenothiazine core PTZ1 and PTZ2 (Figure 15) They found that a very small variation of the molecular structure showed a strongly effect on the photovoltaic performance of the PSC. The difference between the two HTMs is simply the presence of a phenyl as a spacer between the phenothiazine and the amino nitrogen in PTZ2 with respect to PTZ1. The HTMs have HOMO of -4.77 eV and 5.15 eV for PTZ1 and PTZ , respectively.

The PCE of PTZ1, PTZ2 and Spiro-OMeTAD were 2.1%, 17.6% and 17.7% respectively. PTZ2 ($J_{sc}=2.11\text{mA}/\text{cm}^2$, $V_{oc}=1.11\text{V}$ and $FF=0.75$) showed to approach an efficiency not so far from to the state-of-art Spiro-OMeTAD and incredibly higher than PTZ1, simply due to extension of conjugation.

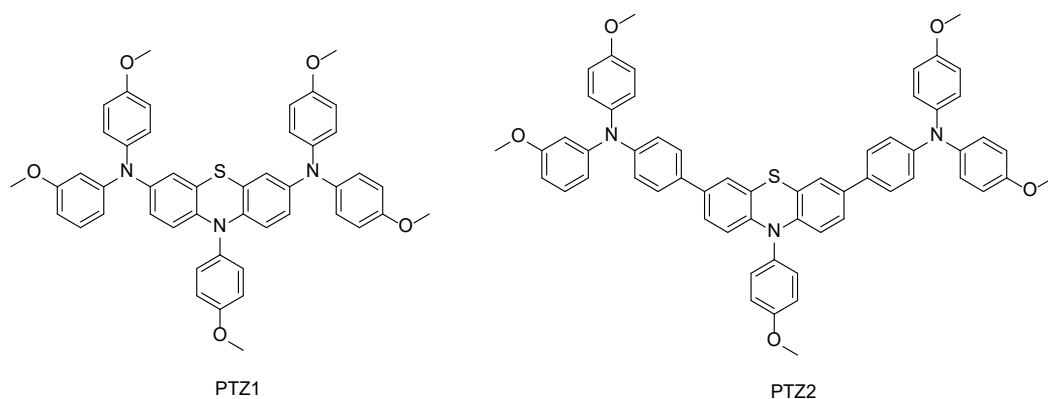


Figure 15. Chemical structures of the PTZ1 and PTZ2 HTMs.¹⁴¹

In 2019, Salunke et al.¹⁴² have designed and synthesized two new HTMs based on phenothiazine molecule AZO-I and AZO-II (Figure 16) via facile, eco-friendly and cheap Schiff base chemistry and low-cost precursors. The PCE of AZO-I, AZO-II and Spiro-OMeTAD are 14.3%, 16.6% and 19.3%, respectively. It was found that devices based on AZO-II were more stable than AZO-I and the state-of-art Spiro-OMeTAD, as it retained 91% of their initial efficiency after 60 days, while, devices based on AZO-I and Spiro-OMeTAD retained 68% and 86%, respectively. Both of the HTMs AZO-I and

AZO-II have similar values of HOMO energy level of 4.97 eV and 4.94 eV but different hole mobilities of $2 \times 10^{-6} \text{ cm}^2\text{V}^{-1}\text{s}^{-1}$ and $2 \times 10^{-5} \text{ cm}^2\text{V}^{-1}\text{s}^{-1}$, respectively. The better results of AZO-II are probably related to its symmetric structure, while AZO-I is asymmetric.

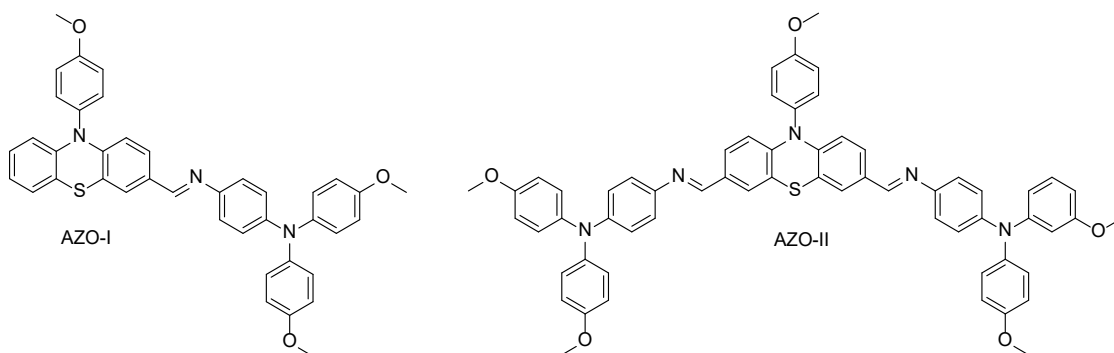


Figure 16. Chemical structures of the HTMs AZO-I and AZO-II HTMs.¹⁴²

Lately, Ding et al.¹⁴³ have developed two new phenothiazine-5,5-dioxide (PDO) based HTMs PDO1 and PDO2 (Figure 17). In PDO1 the 10-N position was substituted with anisole while for in the PDO2 it was substituted with 4,4'-dimethoxytriphenylamine. The 4,4'-dimethoxydiphenylamine is the final substituent group on the phenothiazine for both HTMs. These HTMs were synthesized via Buchwald-Hartwig amination, radical substitution with bromine, followed by the oxidation of sulfur atom and, finally, by a Buchwald-Hartwig cross coupling. The PCE obtained by PDO1, PDO2 and Spiro-OMeTAD are 16.7%, 20.2% and 19.8%. PDO2 gave a better performance than PDO1 as the 4,4'-dimethoxytriphenylamine is a

stronger electron-donating unit comparing to the anisole unit. PDO2 also slightly overcame the state-of-art Spiro-OMeTAD, indicating that it is a promising HTM for PSCs. PDO1 is the oxidized form of PTZ1 shown above¹⁴¹ and has a higher PCE of 16.7% comparing to 2.1 of PTZ1. This is due to the introduction of the sulfone group which changes the molecule structure to a D-A HTM, tunes the energy level, gives excellent charge mobility, thus dramatically improving the device performance. The oxidized phenothiazine core (PDO) also shows a more planar geometry and a strong molecular stacking.

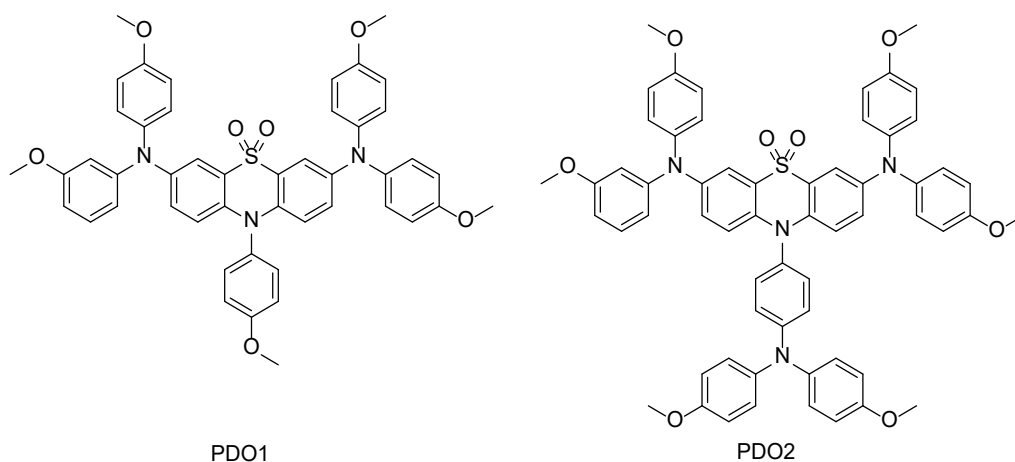


Figure 17. Chemical structures of the PDO1 and PDO2 HTMs.¹⁴³

In 2019, Tsang's group¹⁴⁴ developed a D- π -D skeleton containing phenothiazine as dopant-free hole transporting materials (BDT-PTZ and BDT-POZ) (Figure 18). The concept of the molecular design is to have two donor units connected through a

fused benzodithiophene core leading to better electron donating character and hole mobility. The two HTMs were prepared through the Suzuki cross coupling reaction. The recorded PCE of devices based on dopant-free BDT-PTZ, BDT-POZ and PTAA are 18.26%, 19.16% and 17.85%, respectively. Both the new HTMs have a better behavior than the state of art PTAA HTM.

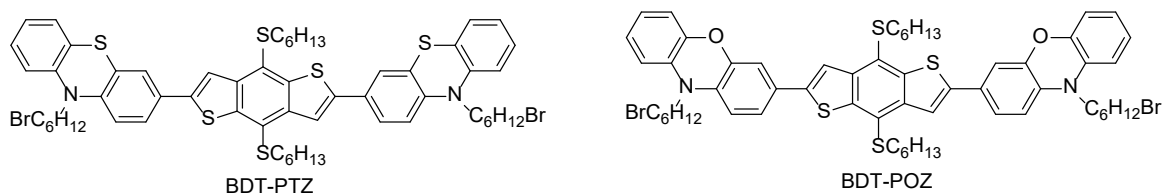


Figure 18. Chemical structure of the BDT-PTZ and BDT-POZ HTMs.¹⁴⁴

Liu et al.¹⁴⁵ developed a new dopant-free HTM based on phenothiazine core unit, PTZ-TPA (Figure 19), with an efficiency of 14.3% recorded without any dopant. In the same conditions, the dopant-free Spiro-OMeTAD gave a very low efficiency (7.39%). According to the long term stability measurements, PTZ-TPA based solar cells are more stable than Spiro-OMeTAD based devices under air exposure. The easy synthesis, the appropriate energy levels and the high hole mobility are making PTZ-TPA a promising alternative HTM to Spiro-OMeTAD for large scale production of stable and high performance perovskite solar cell devices.

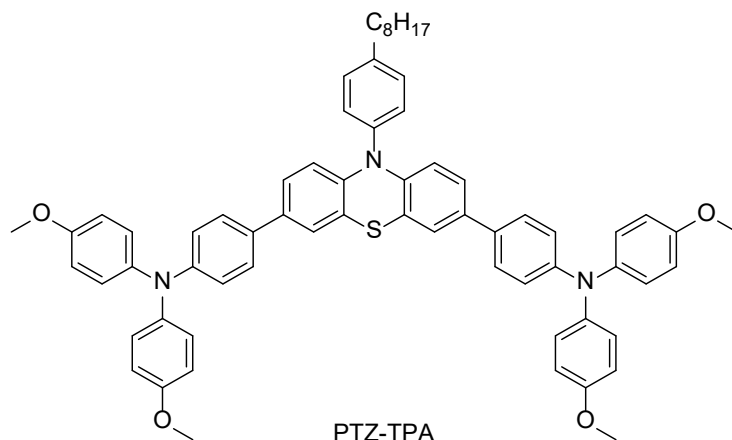


Figure 19. Chemical structure of the PTZ-TPA HTM.¹⁴⁵

In 2019, Maciejczyk et al.¹⁴⁶ prepared two new HTMs based on the triphenylbenzene core TPB(2-MeOTAD) and TPB(2-TPTZ) Figure 20. The use of phenothiazine increased the solubility and decreased the cost of the new HTM TPB(2-TPTZ). The new HTMs were prepared from low cost and commercial starting material 1,3,5-tris(2-bromophenyl)-benzene, which could also be prepared via aldol condensation from 2'-bromoacetophenone and SiCl_4 . This compound was then reacted with the proper terminal groups by Buchwald-Hartwig amination, giving good yields (73% and 50%) and very low total cost of 12.98 \$/g and 3.09 \$/g respectively for the final HTMs TPB(2-MeOTAD) and TPB(2-TPTZ), comparing to Spiro-OMeTAD (around 100 to 400 \$/g). The efficiencies of TPB(2-MeOTAD), TPB(2-TPTZ) and Spiro-OMeTAD were 12.14%, 4.32% and 19.04%, respectively.

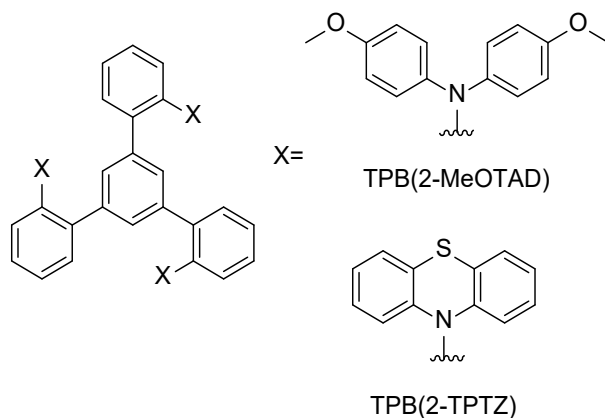


Figure 20. Chemical structures of the TPB(2-MeOTAD) and TPB(2-TPTZ) HTMs.¹⁴⁶

To obtain low-cost HTMs, Robertson et al.¹⁴⁷ had developed a series of HTMs based on spiro[fluorene-9,9'-xanthene] core, SFX-TCz, SFXTAD, SFX-MeOTAD, and SFX-TPTZ (Figure 21). The novel HTMs were prepared using Buchwald-Hartwig coupling giving very good yields. SFX-MeOTAD HTMs gave the best PCE of HTMs series of 12.4% which is close to spiro-OMeTAD in the same conditions (PCE 13%).

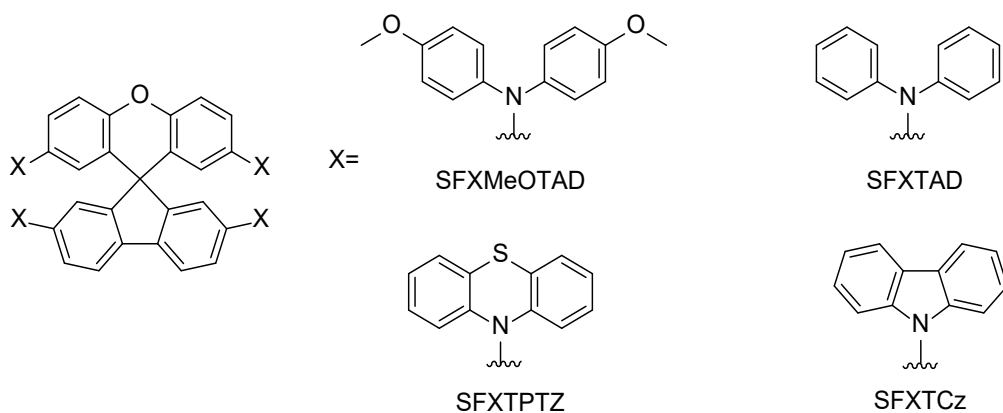


Figure 21. Chemical structures of the SFXMeOTAD, SFXTAD, SFXTPTZ and SFXTCz.¹⁴⁷

Liang et al.¹⁴⁸ have designed and synthesized two SFX-centered compounds tetrasubstituted with phenothiazines at the positions 2,2',7,7'- (SFX-PT1) and 2,3',6',7'- (SFX-PT2) respectively, as well as one spiro-centered compound Spiro-PT (Figure 22). It has been demonstrated that SFX-centered HTMs have higher LUMO levels, larger Stokes shift, higher thermal stability and hole mobility than that of spiro-centered HTMs. As a result, SFX-PT1 containing the SFX core and 2,2',7,7'- tetrakis (N-phenothiazyl) substitutes have the highest LUMO energy level, Stokes shift, T_d , T_g and hole mobility. They believe that SFX-centered phenothiazine substituted HTMs can be used as efficient candidates to substitute the state-of-the-art Spiro-OMeTAD if their solubility can be enhanced.

The hole mobilities of SFX-PT1, SFX-PT2 and Spiro-PT are estimated to be $2.08 \times 10^{-3} \text{ cm}^2\text{V}^{-1}\text{s}^{-1}$, $2.76 \times 10^{-4} \text{ cm}^2\text{V}^{-1}\text{s}^{-1}$ and $1.29 \times 10^{-4} \text{ cm}^2\text{V}^{-1}\text{s}^{-1}$, respectively. The hole mobility of SFX-PT1 is higher than that of Spiro-PT and Spiro-OMeTAD ($2.0 \times 10^{-4} \text{ cm}^2\text{V}^{-1}\text{s}^{-1}$). This indicates SFX-PT1 could be a promising HTM and can contribute to the better performance of PSC devices.

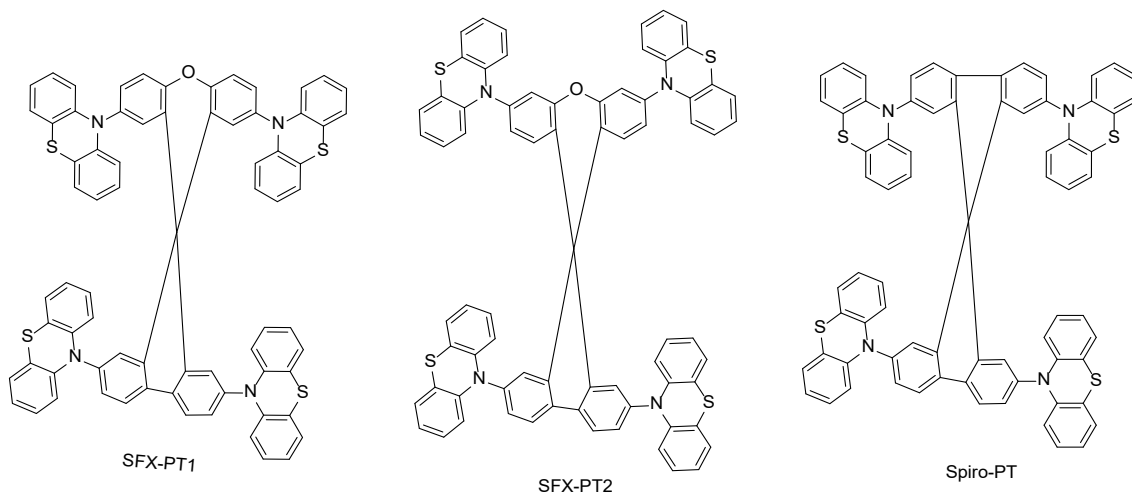


Figure 22. Chemical structures of the SFX-PT1, SFX-PT2 and Spiro-PT HTMs.¹⁴⁸

In 2021, Zhai et al.³⁰ prepared and investigated the impact of spatial molecular structure of phenothiazine based monomer and dimer HTMs PTZT and D-PTZT (Figure 23) on their photoelectrochemical and physicochemical properties. It was found that PTZT, having better hole mobility than D-PTZT showed a higher PCE than D-PTZ (18.74% vs 15.48%), also slightly higher than Spiro-OMeTAD (18.45%).

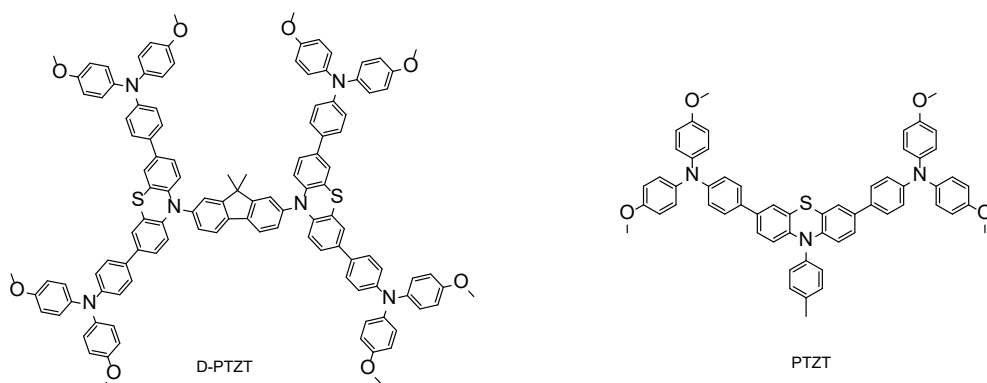


Figure 23. Chemical structure of the D-PTZT and PTZT HTMs.¹⁴⁹

4 TRANSPARENT TANDEM SOLAR CELLS

The main goal of the project on which this thesis is based, is to develop a transparent photovoltaic (PV) system to convert selective ranges of light spectral wavelength in the UV and NIR region while excluding the visible region to reach colorless and fully transparent solar cell devices. To achieve this goal, an innovative approach have been followed based on hybrid tandem UV-perovskite solar cell (UV-PSC) with NIR-dye-sensitized solar cell (NIR-DSSC). The main goal of the overall project is to obtain full transparency and PCE of 14% with device lifetime of 25 years.

4.1 Absorption of light irradiation in the UV-region (<450nm) and the NIR part (>700nm) portions of the solar spectra.

Currently, most PV devices absorb light in the visible region of the light spectrum which indicates why these devices are not transparent. The opsin and rhodopsin receptors contain the three types of cones of retina are sensitive around 555nm and 500nm at shadow (Figure 24). To obtain the transparency to human eyes, the project will focus on developing and integrating UV efficient PSC with $\lambda < 450$ nm and near IR-DSSC with $\lambda > 700$ nm to obtain a fully transparent tandem solar cell (Figure 24).

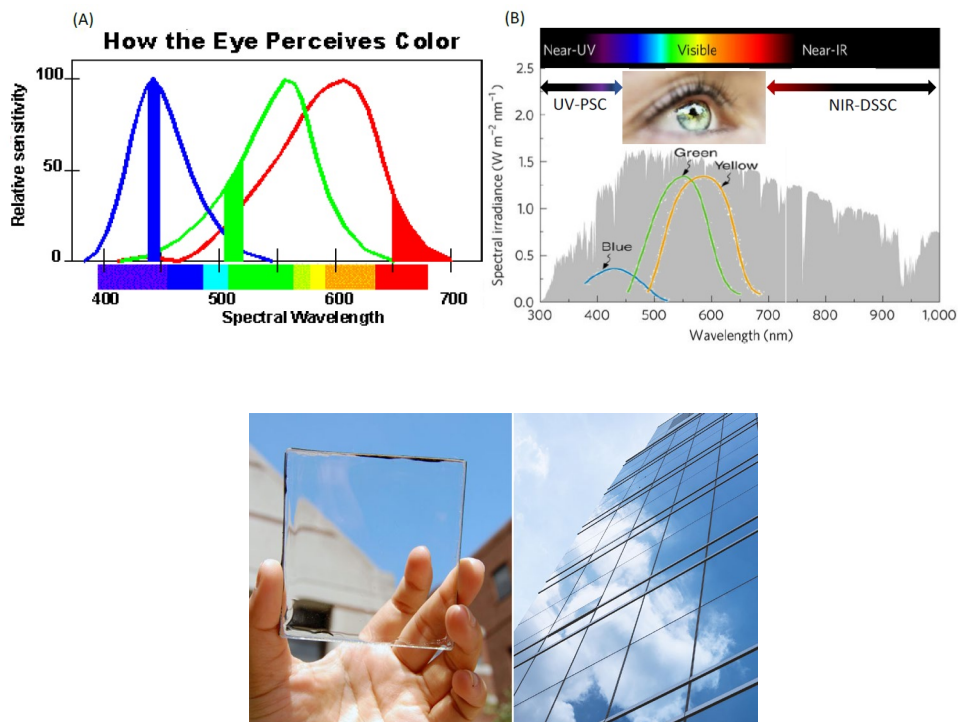


Figure 24. (A) Absorption threshold and sensitiveness of the three families of cones composing human retina, (B) Solar spectrum at A.M.1.5G conditions vs. the spectra position of UV-perovskite solar cells and NIR-dye sensitized solar cells (Modified from ref. 150).¹⁵⁰

4.2 Transparent Hole Transporting Materials

Recently, a lot of attention has been devoted to transparent semiconductors for tandem solar cells applications.^{151,152}

Mostly inorganic HTMs are used as transparent hole transporting materials such as CuSCN ,^{153,154} CuI ,¹⁵⁵ NiO_x ,^{156,157} MoO_x ,¹⁵⁸ CuGaO_2 ,¹⁵⁹ and $\text{Sr}_3\text{Cu}_2\text{Sc}_2\text{O}_5\text{S}_2$.¹⁶⁰ In the case of organic transparent HTMs, currently PTAA and Spiro-OMeTAD are the most used compounds.^{83,84,161}

However, PTAA and Spiro-OMeTAD have limitation for commercialization in the future because of their high synthesis and purification cost.^{70,162}

In fact, in order to bring PSCs to commercialization it is required to synthesize highly efficient and low-cost new HTMs to replace PTAA and Spiro-OMeTAD to improve the photovoltaic efficiency and performance of perovskite solar cells-based devices, while maintaining a reasonable cost.¹⁶³

One of the most challenging issues is the development and design of transparent organic HTMs, because it is important to extend the π -conjugation to minimize the reorganization energy and also to gain larger electronic coupling between the neighbor molecules in the molecular packing structure, but the extension the π -conjugation causes the red shift (bathochromic shift) in the light absorption of the molecules.¹⁶⁴ Also, tuning the HOMO energy level with the active layer is a key factor for high performance PSCs devices¹⁶⁵ since it is important to tune the energy levels of HTM with the perovskite active layer.¹⁶⁵

5 METHODOLOGY DEVELOPMENT

5.1 An overview

The main task of the thesis project is about the synthesis, characterization, and selection of transparent Hole Transporting Materials (HTMs) for perovskite solar cells (PSC) having tailored properties and a proper energy levels alignment with the perovskites developed by other partners, according to existing projects on perovskite solar cells and tandem cells involving them.

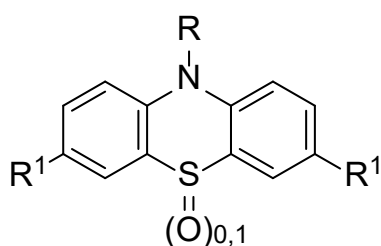
As a matter of fact, the HTMs are highly conjugated systems (small molecules or polymers) providing fast charge extraction and transport to avoid the recombination of photogenerated excitons at the interface between the HTM and the perovskite.

This extended conjugation path of HTMs often makes them colored. The main task of the thesis project is to obtain light-selective transparent photovoltaic devices, for which HTMs with high transmittance in the visible region are required. The proposed materials should warrant an average visible transmittance (AVT) > 85% in the visible range and, at the same time, should provide a power conversion efficiency of 6% at least in perovskite solar cells.

To ensure transparency, a wide band gap (i.e. an absorption below 450 nm) is required. Beside transparency, the more important feature of a HTM is the energy of its HOMO level, that should be relatively high to be easily oxidized, being thus

prone to extract holes efficiently from the perovskite (PSK) layer with which it is in contact. However, to assure the PSC to work properly, the HOMO and LUMO energies should be higher than the perovskite valence band and conduction band, respectively. In fact, the difference between the HTM LUMO energy level and the perovskite conduction band should be large enough to prevent the electron backflow from perovskite to the HTM which is an undesired process, that can result in a substantial performance reduction. These requirements could be obtained by the engineering of the molecular structure of the HTMs through the introduction of specific functional groups on a central core. The literature on molecular HTMs is enormous^{13,77} and different combinations of heterocycles and functional chemical groups have been proposed. Among them, the class of triaryl amines showed to be highly efficient and most HTMs are based on this structural element.^{13,75,77} As a matter of fact, the reference small molecule and polymer HTMs, spiro-OMeTAD and Polytriarylamine (PTAA) belong to this class. Searching for a different and new scaffold that could comply with the project's requirements, the phenothiazine unit seems to be an interesting heterocycle to be used as main scaffold for transparent materials since its peculiar structure breaks the conjugation at the nitrogen level resulting in a limited or no absorption above 450 nm. The phenothiazine was thus chosen as the main scaffold, which was then modified by: (i) introducing alkyl or aryl groups on the nitrogen atom, (ii) functionalizing the 3 and 7 positions with several

different pendant groups and (iii) oxidizing the phenothiazine sulphur atom (Figure 25). All these modifications have led to the tuning of the HOMO energy level, which is essential to allow the energy matching with the perovskite valence band in order to obtain an effective extraction of holes. The electrochemical, optical, and thermal characterizations of the proposed materials helped to select the best materials to be proposed for the preparation of perovskite solar cells.



R = alkyl, aryl, substituted aryl

R¹ = H, Br, aryl

Figure 25. General structure for the proposed HTMs.

The investigation involved the synthesis and the structural, electrochemical, optical, and thermal characterization of three different series of phenothiazine-based HTMs for applications in (semi)-transparent perovskite solar cells. Particularly, the various characterizations helped to select among the different series of HTMs the best candidates for the photovoltaic application and, finally, the one which was selected as the most reliable HTM. Selected HTMs showed a very high AVT, close to 90%; a

value much higher compared to the targeted values (85%) and comparable with the literature standards. Additionally, once implemented in the devices, the most performing HTMs provided overall efficiency over 7% and a remarkably high V_{oc} (1.65 V) proving limited internal energy losses.

5.2 Development of phenothiazine-based hole transporting materials

The phenothiazine has been chosen as the base scaffold to build new HTMs as it is cost effective and easy to be functionalized at 3 and 7 positions. Moreover, the presence of nitrogen allows a functionalization, while the sulphur can be useful both for further oxidation (*vide infra*) and for the possible interaction with the lead contained in the perovskite (i.e., leading to a better interface between the active layer and the HTL). This kind of interaction is very important in the PSCs, since it can result better surface morphology and crystallinity and contributes to the improvement of the stability and performance of the device.^{166,167} Based on this scaffold three main classes of derivatives were prepared. The main difference was the substitution pattern of the phenothiazine nitrogen (Figure 25). The series **1** contains a hexyl (alkyl) group on the phenothiazine nitrogen while the series **2** contains an aromatic moiety, the 4-butoxyphenyl group. The series **3** is a further derivative of the series **2**, since in this case the sulphur is oxidized to a sulfoxide moiety. The modification of the functionalization of nitrogen (series **1** and **2**) should not have a sizeable impact on the energy level of the systems but it is expected to play a role in the deposition of the HTM on the PSK layer and on the packing of the former. On the other hand, the oxidation of the S atom will lead to a severe stabilization of the core, leading to deeper HOMO (i.e., less easily oxidizable

molecules). Several compounds belonging to these series were prepared and characterized, to find the best material and conditions to fulfil the project needs.

First of all, the general synthetic strategy and the approach to the optimization of reaction conditions will be presented.

5.3 Synthetic Strategy

In this thesis three series of small molecule HTMs will be presented, along with their characterization. Before discussing the characterization and the application of those HTMs, it is opportune to introduce the chemistry of the phenothiazine and the synthetic strategy used to obtain the different classes of compounds. The three series are shown in Figure 26, where it can be immediately appreciated that they contain a central phenothiazine, surrounded by two lateral substituents. The functionalization at the ring nitrogen makes the difference between series **1** (alkyl) and series **2** and **3** (aromatic), while series **3** differs from series **2** since the phenothiazine sulfur atom was oxidized to sulfoxide. While the intermediates can be prepared by using literature methods we tried to adapt and optimize the synthesis to the specific compounds, when possible. The challenges encountered during the functionalization of phenothiazine and the final Suzuki cross-coupling are described

below, along with suggestion on how to improve the methods to facilitate the purification.

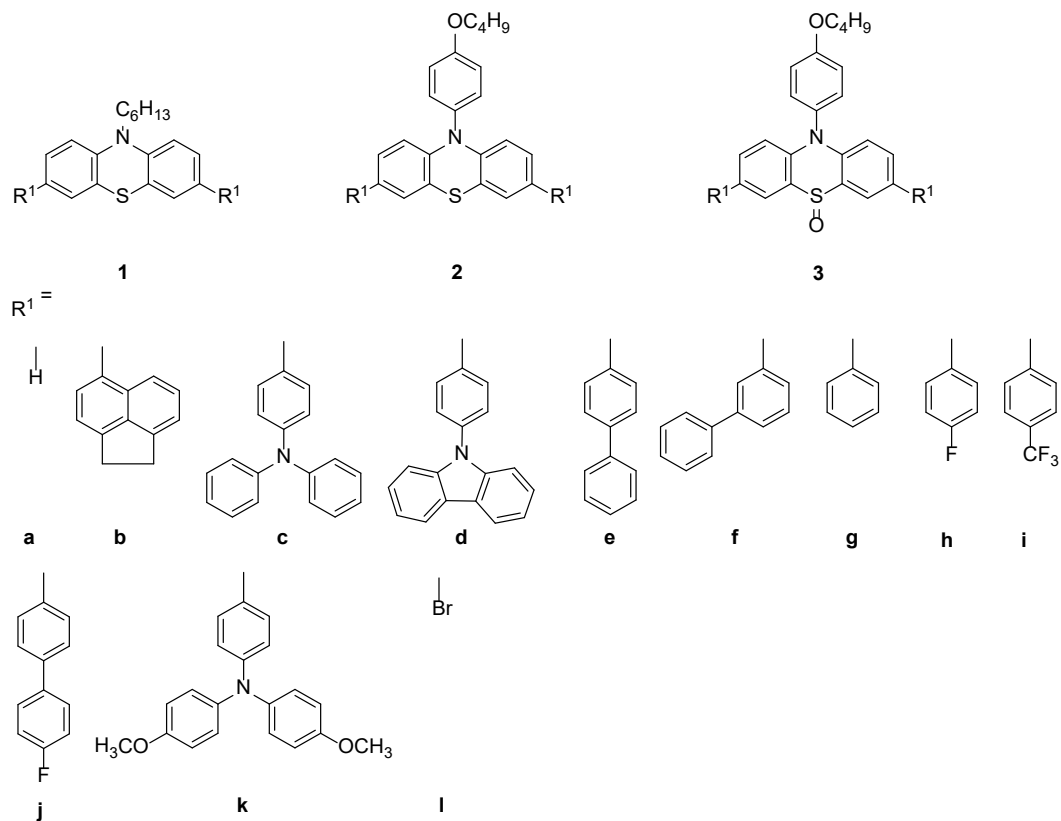


Figure 26. Structure of the three different series of HTMs.

5.3.1 Scaffolds core preparation

Here the preparation of the compound **1I** and **2I** (Figure 27) is described as the intermediate for the preparation of the series **1** and **2**. The main ways to obtain compound **1I** are in principle two, which are reported here below. The route 1

proposes to brominate first the phenothiazine and after to alkylate the heterocyclic nitrogen.

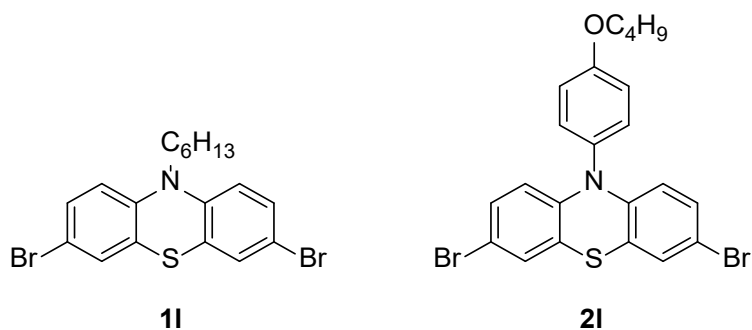
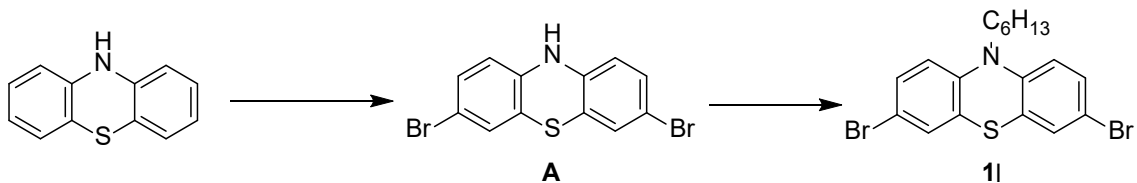


Figure 27. Compounds **1I** and **2I**, as the fundamental intermediates to prepare series **1** and **2**.

5.3.1.1 Scaffold **1I**

Route 1 was proposed to brominate first the phenothiazine and after to alkylate the heterocyclic nitrogen.

5.3.1.1.1 Route 1:

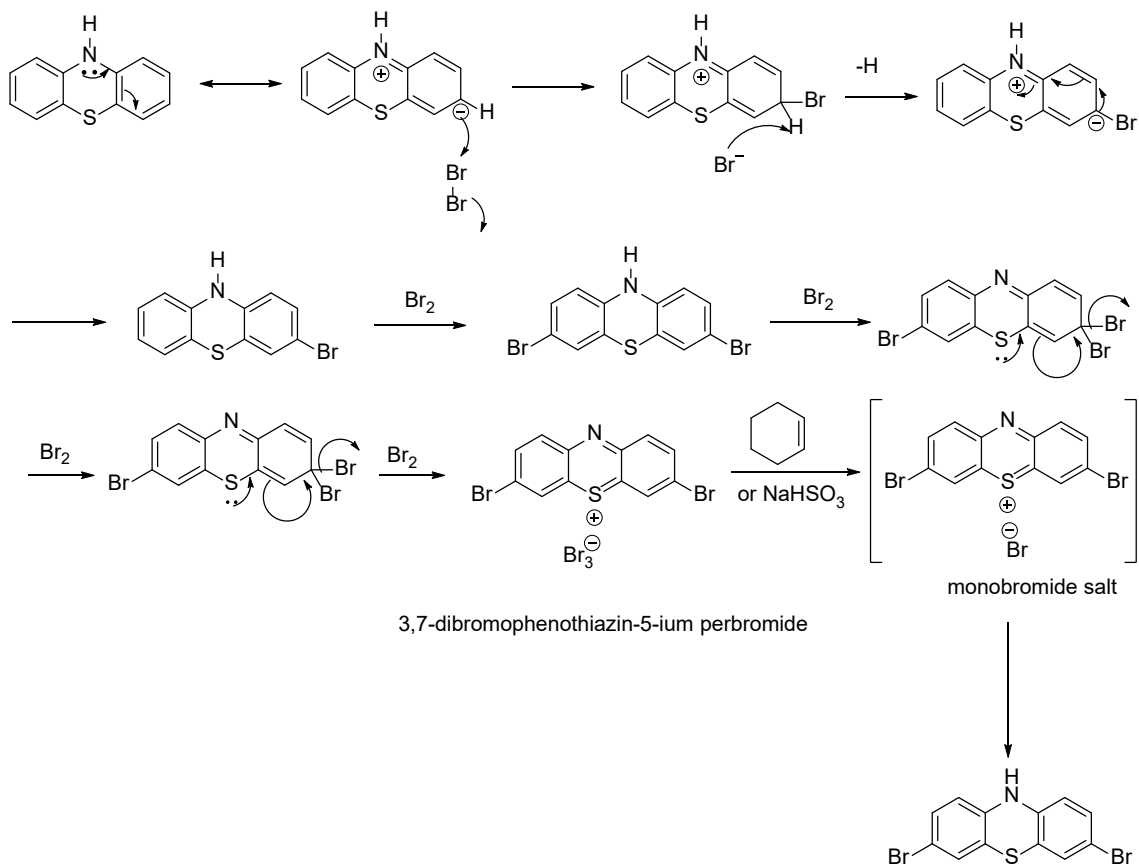


Scheme 3. Route 1 to compound **1I**.

In principle this way should be interesting, since the first intermediate, **A**, can be used to produce several scaffolds, by simply changing the alkylation/arylation reagent to functionalize the phenothiazine nitrogen.

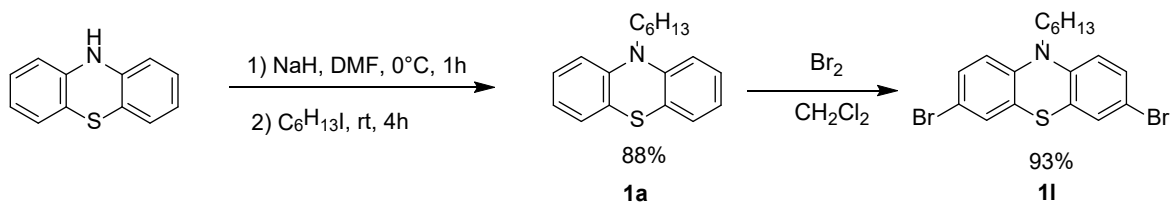
While being more interesting for the above reasons, route 1 was a bit complicated from the practical point of view. At first, we tried to brominate the phenothiazine using NBS as bromine source, but the reaction did not work as expected. Further, we tried using bromine as the brominating agent, but the intermediate was not pure enough due to the formation of mono and dibromophenothiazine derivatives (Scheme 3) which were impossible to separate. However, we tried to alkylate this material, hoping to get rid of impurities (monobrominated phenothiazine and other impurities) after the second step but, still, we could not obtain a final pure material, nor by crystallization nor by chromatography. Finally, due to these practical complications, we decided to resort to route 2 (Scheme 5).

During the bromination step using bromine it was not easy to obtain the dibromophenothiazine. In this process the formation of phenothiazine perbromide salts also occurs as in the mechanism shown in Scheme 4 and the work up needs to be performed using sodium sulphite and it takes 2 to 3 hours. The final product was difficult to be purified from the small quantity of impurities.



Scheme 4. Mechanism for the bromination of the phenothiazine.¹⁶⁸

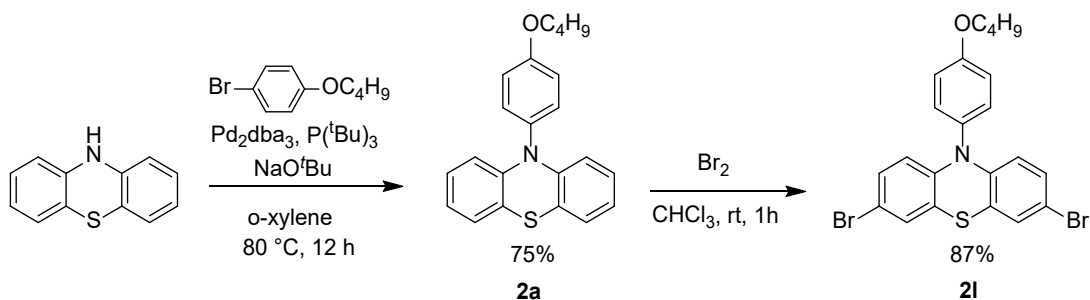
5.3.1.1.2 Route 2:



Scheme 5. Route 2 to compounds **1a** and **1l**.

The sequence of route 2 is related to route 1 simply by switching the order in which the reaction steps are performed as described in scheme 5. This gave an easier way to get the final material in a pure form and high yields. Therefore, we can suppose that in the route 1, probably the presence of the NH group can be the source of side reactions, i.e, the ipso-bromination that can bring to the perbromide salt,^{168,169} or at least it can influence the bromination reaction, giving small quantities of impurities (unwanted mono-brominated phenothiazine and degradation products) that could not be further separated.

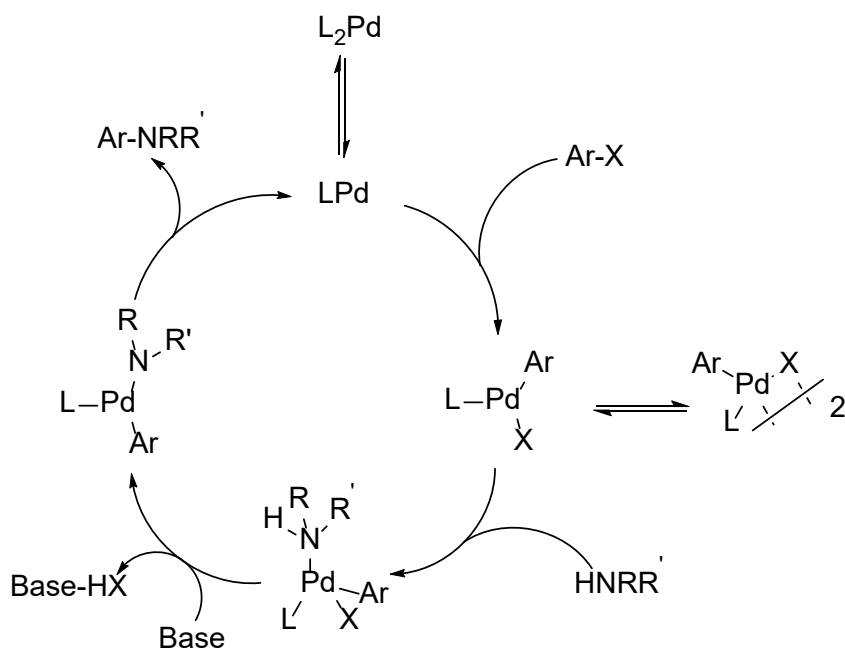
5.3.1.2 Scaffold **2I**



Scheme 6. Synthetic pathway to intermediates **2a** and **2I**.

Intermediate **2I** was prepared in 2 steps, starting from phenothiazine, by using the Buchwald-Hartwig cross coupling reaction to functionalize the heterocyclic nitrogen, followed by bromination. Since the preparation of the dibrominated phenothiazine **A** in route 1 for the preparation of **1I** was not successful, the strategy for the

preparation of **2I** was based directly on the route 2 approach. This synthetic pathway worked well and with good yields. The first step was accomplished by a Buchwald-Hartwig protocol, with Pd₂dba₃ as catalyst, P(tBu)₃ as ligand and NaOtBu as base, in o-xylene at 80°C for 12h. The product **2a** was obtained in very good yield 75 %. This kind of reaction works with a mechanism as that reported in scheme 7. As one can see, a LPd(0) complex can undergo the oxidative addition by the Aryl halide (Ar-X) followed by the addition of the Amine (HNRR'). This complex reacts with the base which extracts the proton of the amine, thus activating the complex towards the last step, the reductive elimination which expels the final product (a further substituted amine, Ar-NRR'), restoring the LPd(0) complex.



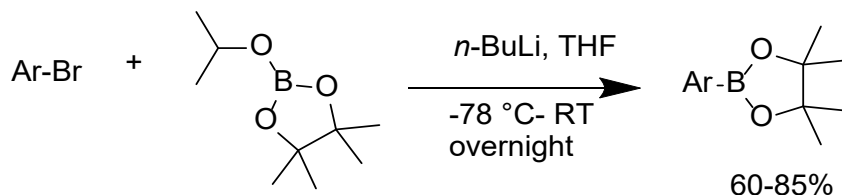
Scheme 7. Mechanism of the Buchwald-Hartwig reaction.¹⁷⁰

5.3.2 Preparation of Arylboronate reagents

Boron element ($2s^2 2p^1$) can engage in three sp^2 hybridized bonds, resulting in a trigonal planar geometry. Boron compounds are highly electrophilic, having an empty p-orbital orthogonal to the plane, inexpensive and readily prepared. They have a broad functional-group tolerance, are relatively stable and generally environmentally benign. Some are thermally stable and inert to water and oxygen, thus easy to handle (especially for industry). Besides, they can easily transmetalate with a variety of metal compounds under exceptionally mild reaction conditions, especially versatile with palladium(II) complexes. This has allowed the Suzuki-Miyaura reaction to develop into the most widely applied transition metal catalyzed C-C bond forming reaction to date.

To exploit the scaffolds to build final HTMs, the bromine of the scaffold can be substituted with aryl-based substituents. Many cross-coupling reaction can be exploited (e.g., Suzuki, Buchwald Hartwig, Stille protocols), depending on the kind of reagents one wants to use. The Suzuki protocol is attracting because it is simple and easy to perform. Thus, starting from arylbromides, many boronated reagents were produced to be used in the cross coupling with the phenothiazine scaffolds. We planned to introduce as many substituents as possible on the phenothiazine scaffolds. Apart from commercial reagents, being boronic acids or esters (mainly boronic acids), we needed to prepare some of them. We chose to prepare boronic

esters because they are more stable and easier to be purified. We used a general borylation reaction based on bromine-lithium exchange using *n*-BuLi, followed by transmetalation with the boron compound, as reported below in Scheme 8.



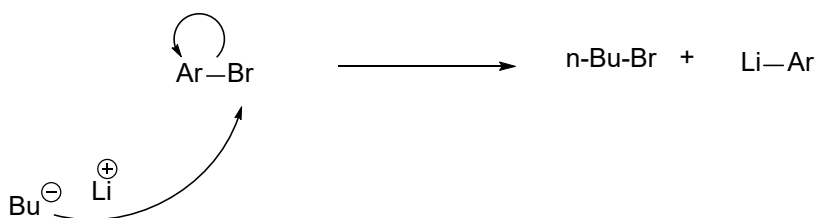
Scheme 8. General borylation reaction used for the preparation of some intermediates.

5.3.2.1 Lithium-Bromine exchange

The first step is based on the Li-Br exchange on the Aryl bromide. While quite old, two mechanisms were hypothesized.

5.3.2.1.1 The Gilman's Mechanism

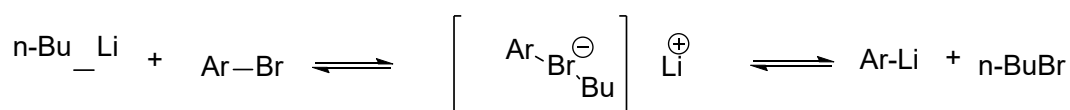
Gilman proposed a mechanism which suggests a nucleophilic attack of the butyl carbanion on the bromine atom and the formation of the lithium aryl salt:¹⁷¹



Scheme 9. Gilman mechanism for the lithium-bromide exchange.

5.3.2.1.2 The Wittig's mechanism

The mechanism proposed by Wittig postulated a reversible formation of an "ate-complex" (a term coined by Wittig), which further decomposed to the bromobutane and the aryl lithium salt (Scheme 10).¹⁷²

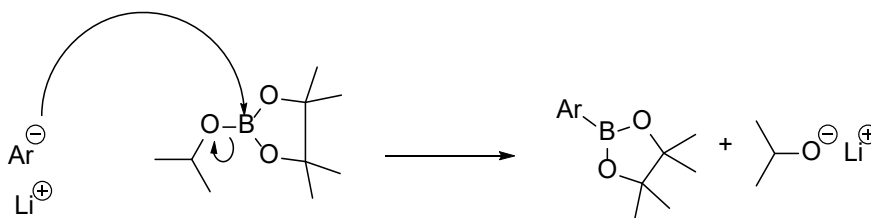


Scheme 10. Wittig mechanism for the lithium-bromide exchange.

5.3.2.2 Transmetalation

As the reactivity of C-Metal bond generally increases with the increasing the ionic character of the C-M bond, the percent ionicity (ionic character) is related to the electronegativity difference (EN) of the C-M bond (Table 1). One can note that the lithium can give the higher percent ionicity of the C-M bond.

Thus, the Aryl lithium salt reacts with the boronic ester 2-isopropoxy-4,4,5,5-tetramethyl-1,3,2-dioxaborolane (Scheme 11) when the anionic aryl electron rich group attacks the boron. At the same time, the isopropoxy group is expelled as an anion, giving a lithium salt.



Scheme 11. Mechanism for the transmetallation step.

Table 1. Electronegativity vales and ionic character of some metallic elements and carbon.

Element	Li	Mg	Ti	Al	Zn	Cu	Si	Sn	B	C
EN*	0.97	1.23	1.32	1.47	1.66	1.75	1.74	1.72	2.01	2.50
%Ionicity	43	35	30	22	15	12	12	11	6	--

*Allred/Rochow electronegativity (EN).

5.4 HTMs Synthesis

The HTMs, being both small molecules or polymers, were prepared starting from the dibromophenothiazine scaffold shown above, and using either Suzuki or Buchwald-Hartwig cross coupling reactions.

5.4.1 HTM Small Molecules

All HTMs were prepared by Suzuki cross coupling reaction, using the above phenothiazine scaffolds and the aryl boronic acid or esters.

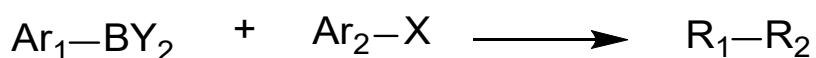
5.4.1.1 Suzuki coupling

The Suzuki reaction is an organic cross coupling reaction for C-C bond formation, where the coupling partners are an organo-halide and organo-boron species, and palladium(0) complexes are used as catalyst.^{173–175}

The first publication was released in 1979¹⁷³ by A. Suzuki. The Suzuki coupling reaction is now a classic method for researchers and industry for they synthesis of fine chemicals, pharmaceuticals, nature products and polymers (Scheme 12).^{176,177}

The impact of this and similar reactions was enormous in all practical organic chemistry related fields: pharmaceutical, agrochemical, organic electronics, etc.¹⁷⁸

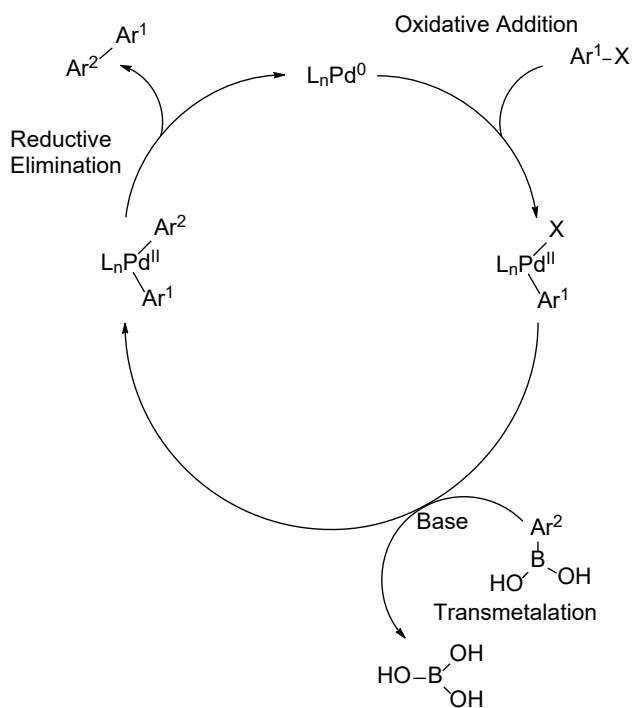
Due to the wide applicability of Pd-catalyzed cross-coupling reactions, A. Suzuki, R.F. Heck and E. Negishi were awarded the Nobel prize in Chemistry in 2010, for their contribution in the discovery and development of this class of reactions.¹⁷⁹ Some of the advantages of Suzuki coupling are low toxicity, facile access to the organoboron species, mild reaction conditions and their chemo-selectivity.¹⁸⁰



Scheme 12. General scheme for the Suzuki reaction.

The mechanism of the reaction is shown in Scheme 13. The $\text{L}_n\text{Pd}(0)$ complex undergoes the oxidative addition by the $\text{Ar}^1\text{—X}$ aryl halide giving a Pd(II) complex. This

complex gives the base-assisted transmetalation with the $\text{Ar}_2\text{-B(OH)}_2$. The halogen and the boric acid are expelled during this step. As a result of the transmetalation, a $\text{L}_n\text{Pd(II)Ar}^1\text{Ar}^2$ complex was produced, which finally gives the $\text{Ar}^1\text{-Ar}^2$ coupling product and restores the $\text{L}_n\text{Pd(0)}$ catalyst.

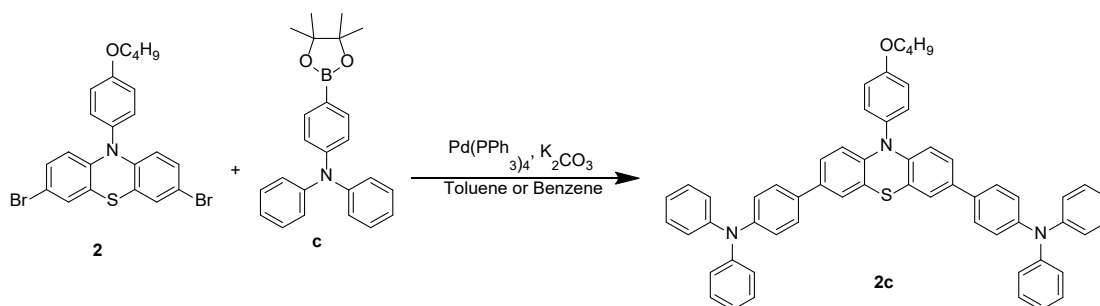


Scheme 13. Catalytic mechanism of the Suzuki coupling reaction.

5.4.1.2 Optimization of conditions for the Suzuki Coupling reaction.

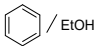
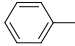
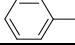
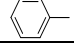
We tried to apply different Suzuki reaction conditions. We used the preparation of the HTM **2c** as a test reaction (Scheme 14). The reaction was first performed

following the original Suzuki protocol, in benzene/ethanol (1:1) at 130°C, but working under MW irradiation with an excess of boronic ester over the bromide of 1.1, obtaining a yield of just 16% (Table 2).



Scheme 14. Optimization reaction for HTM **2c**.

Table 2. Optimization of conditions for the Suzuki reaction for the preparation of the HTM **2c**.

Entry	2 (eq)	c (eq)	Aliquot	Solvent	Time	Temp.	Yield
1 ^{a, b}	1	2.20	-	 / EtOH	1 h	130 °C	16%
2 ^{a, b}	1	2.70	-		1 h	130 °C	30%
3 ^c	1	2.70	20%		12 h	110 °C	80%
4 ^d	1	2.40	20%		12 h	110 °C	87%

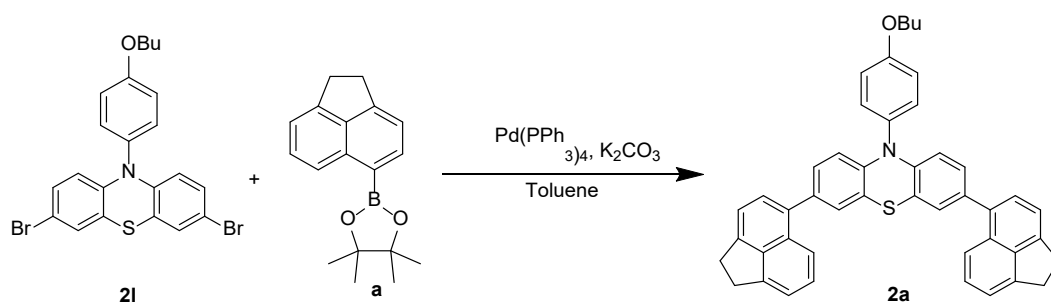
Conditions used in all entries: Catalyst: Pd(PPh₃)₄ 0.05 eq.; Base: K₂CO₃, 6.30 eq. ^a: Microwave irradiation, ^b: Reaction scale on 0.8 millimole of starting material; ^c: Reaction scale on 3.4 millimole of starting material; ^d: Reaction scale on 8.7 millimole of starting material; Yield: Isolated yield.

By changing the reaction conditions using toluene as a solvent (entry 2) and increasing the boronic ester / bromine ratio to 1.35, we got 30% of yield, which is minimal improvement over the use of benzene (entry 1). It was evident that to obtain a high yield it would be needed a further increase of time and/or of

temperature. In particular, the increase of temperature can also increase the risk of decomposition and the production of large quantities of impurities, while the increase of time is unpractical when using microwaves since they are used to shorten the reaction time and in general the microwave driven reactions take from a few minutes to 1-2 h at maximum. Besides, in the case of a scale up, the microwave method is not the option of choice since it is difficult to warm correctly large volumes of solution. Thus, we resorted to the classical heating (entry 3). Since it was reported in the literature that the use of Aliquat as an additive (sometimes it is referred as a co-catalyst) can increase the reaction rate we set-up the reaction of entry 3 at a 3.4 mmol scale, using 20% of Aliquat at a 110°C for 12h¹⁸¹. This reaction was successful and, after work up and precipitation with methanol from a concentrated dichloromethane solution the HTM **2c** was obtained in a 80% yield. This was a remarkable result, slightly improved when the reaction scale was increased to 8.7 mmol by reducing the boronic ester excess to 1.2, obtaining a 87% yield.

When we tried to apply the same conditions defined for **2c** to the synthesis of **2a** (Scheme 15) the yield was lower, 67% (Table 2). We rapidly tried a reaction to analyze this case and to ascertain if there were some other modifications applicable to the protocol. Some reactions were performed again under microwave by raising the temperature (entry 1 and 2) and the boronic ester /bromine ratio (entry 1 and 3), but the product obtained was always impure and virtually impossible to be

purified. Once again, the classical heating method was preferred. Another aspect to be studied was the quantity of Aliquat 336 additive to be used. Just 2 drops of Aliquat 336 were used into a reaction on a 0.2 mmol scale performed at 110°C for 1h, thus obtaining a yield of 71%, while when the reaction was performed on a 4-time larger scale, 0.8 mmol, the yield was lower and the product was impossible to be purified, once again. This meant that the Aliquat 336 additive could not be reduced below 20%. As a final result on this specific compound, the maximum yield was lower than in other case and ranged just below 70%. To obtain the product in large quantities, it seems that the classical heating method is working better than microwaves and that a 20% quantity of Aliquat 336 is needed as shown in scheme 17.¹⁸²



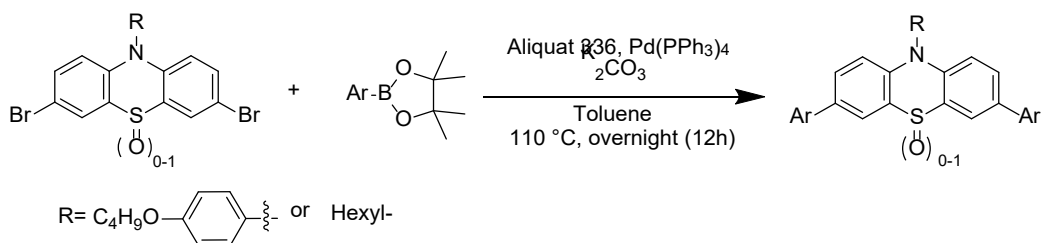
Scheme 15. Optimization reaction for HTM 2a.

Table 3. Optimization conditions for the Suzuki reaction for the preparation of the HTM **2a**.

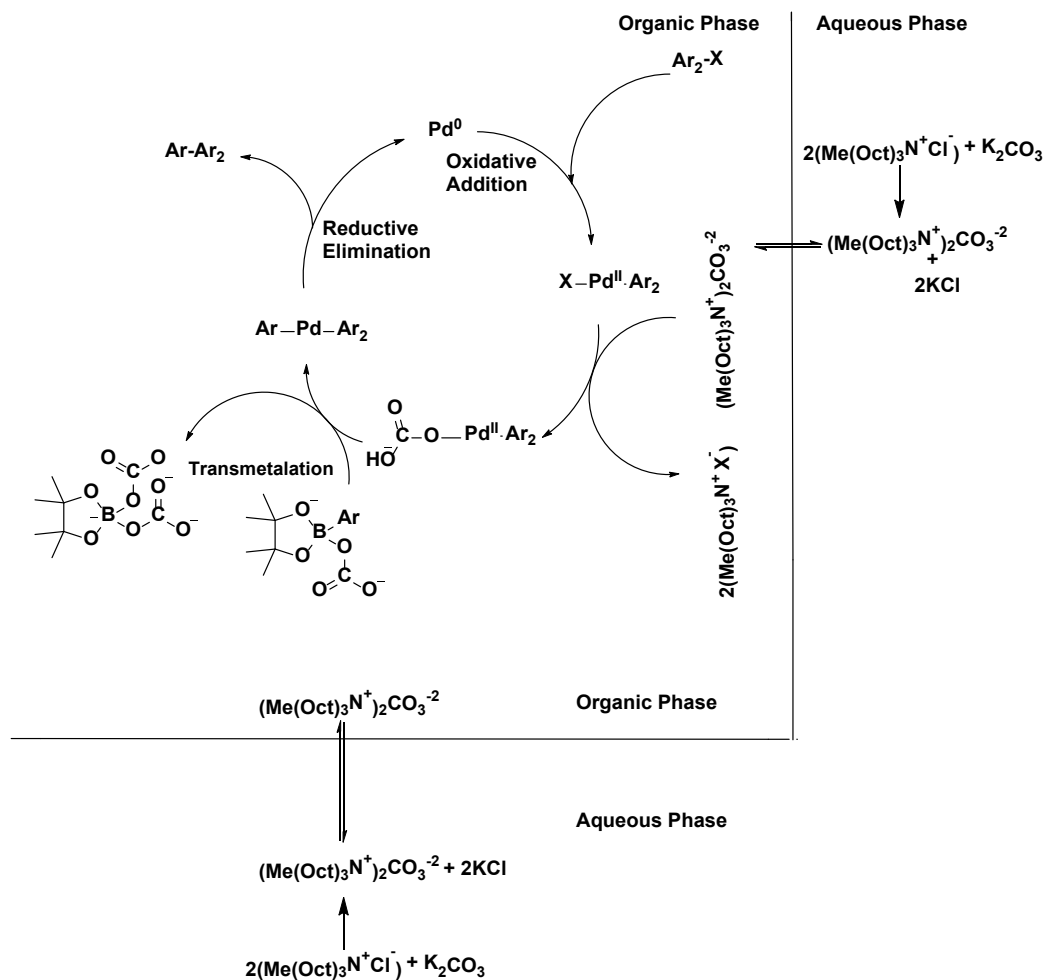
Entry	2 (eq)	a (eq)	Aliquat	Solvent	T(°C)/Time(h)	Y%
1 ^{a, b}	1	2.2	---	Toluene	130/1	- ^c
2 ^{a, b}	1	2.2	---	Toluene	160/1	- ^c
3 ^{a, b}	1	2.7	---	Toluene	140/1	- ^c
4 ^{a, b}	1	2.7	2 drops	Toluene	100/1	71
5 ^{a, d}	1	2.7	2 drops	Toluene	100/1	- ^c
6 ^d	1 ^d	2.7	20%	Toluene	100/12	67

Conditions used in all entries: Catalyst: 0.05 equivalent of Pd(PPh₃)₄; Base: 6.30 equivalent of K₂CO₃. ^a: Microwave irradiation; ^b: 0.2 millimole scale; ^c: Isolated product contains non-separable by-product; ^d: 0.8 millimole scale; Y: Isolated yield. Note: Entries 1 to 5 were done under microwave irradiation.

The application of the same conditions (Pd(PPh₃)₄ 0.05 eq., K₂CO₃ 6.3 eq., Aliquat 336 20%, toluene 110°C, 12h) on the scaffold **1** gave **1c** in a 94% yield and **1a** in 67% in only 4 h. As a general final remark, this work opened the way to the preparation of a potentially large series of HTMs based on phenothiazine scaffolds. The two series **1** and **2** were developed by using the boronic acid or ester derivatives under the above conditions. The yield of the series **1**, **2** and **3** ranged in between 49% and 95%.



Scheme 16. Optimized conditions for the Suzuki coupling reaction.



Scheme 17. Catalytic cycle mechanism of Suzuki coupling reaction in the presence of Aliquat.¹⁸²

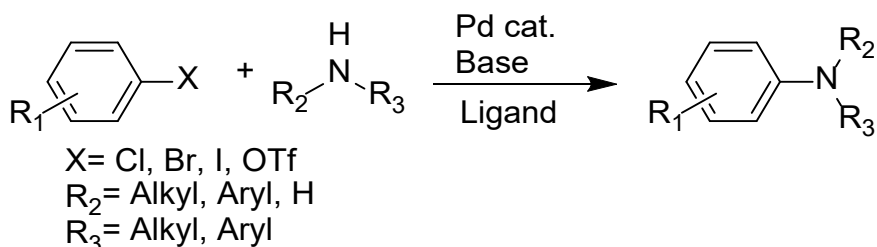
5.4.2 Polymeric HTMs

All polymers were prepared using the Buchwald-Hartwig coupling polymerization, by using the dibrominated scaffold **11** and differently substituted anilines.

5.4.2.1 The Buchwald–Hartwig amination

The Buchwald-Hartwig cross coupling is widely used in organic synthesis for carbon-nitrogen bond formation through palladium-catalyzed cross coupling reaction of aryl halides with amines.⁶⁰ In the last decades, Buchwald amination has become a fundamental tool in the organic chemistry for the C(sp²)-N bond formation.^{61–64} The present nature of aryl amines and related heterocyclic compounds in pharmaceuticals, agrochemicals, natural products and organic molecules related to material science has pushed the development of better methodologies and catalysts, which now are widespread in both academic research and industrial processes.^{65–69} Previously, the C(sp²)-N bond was obtained through nucleophilic aromatic substitutions (S_NAr) or via copper-mediated reactions reported by Goldberg⁷⁰ and Ullmann⁷¹ in the 20th century. However, these methods have drawbacks, as they suffer from narrow substrate scope and require long reaction time, toxic solvents, high temperature and in the case of Ullman coupling, also high copper loading and, last but not least, often the yield are not high. Some of these disadvantages have been overcome in the last decade by using copper-based catalysts which often bear chelating ligands.^{72–75} In 1983, the use of Pd-complexes for C(sp²)-N bond formation was introduced by Migita and others, who reported that Pd-complexes of P(o-tol)₃ catalyze the C(sp²)-N bond formation of

aryl amines from aryl bromides and aminostannanes.^{76,77} The withdraw backs related to both the use of toxic aminostannanes and the narrow substrate scope obtained in this work were later overcome by Stephen L. Buchwald and John F. Hartwig, who reported in 1994 an improved protocol of the amination of aryl bromides and aminostannanes^{78,79} and in 1995 a Pd-catalyzed tin-free coupling of amines with arylbromides (Scheme 18).^{80,81} The mechanism of the Buchwald amination was discussed before in Scheme 7.

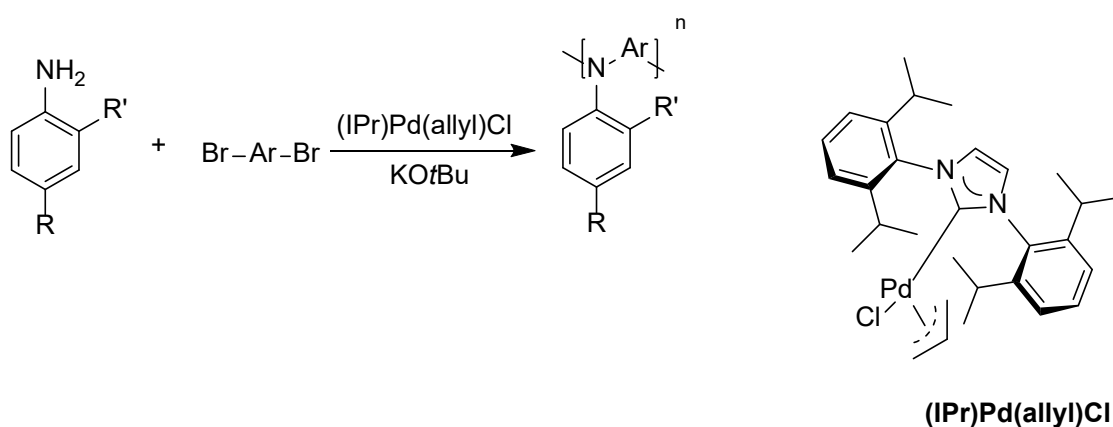


Scheme 18. General protocol of the Buchwald-Hartwig reaction.

5.4.2.2 The Buchwald-Hartwig polymerization

While the Buchwald-Hartwig reaction was strongly improved during the next decades, it was also studied to perform polymerizations. The application of this reaction to obtain polymers was pushed by the widespread application of organic HTMs in organic electronics. The two most reliable and well performing HTMs, a

small molecule (spiro-OMeTAD) and a polymer (polytriarylamine, PTAA), were both belonging to the polytriarylamine class. The urge for new, cheaper, and outperforming HTMs was a strong motivation to develop better synthetic methods that could be adapted also for polymerizations and to control the characteristics of the final product. The best conditions to obtain polytriarylamines with a high degree of control on the structure and molecular weight of the final polymers were obtained by Sprick et al.¹⁸³ They have prepared a library of PTAA based molecules via (NHC)-Pd catalyzed Buchwald amination polymerization of anilines and dibromo arene. They demonstrated that by adding fused ring structures into the polymer backbone and replacing the pendant phenyl groups with electron-withdrawing fluorine or electron-donating methoxy group can influence the molecular weight of the resulting polymer.



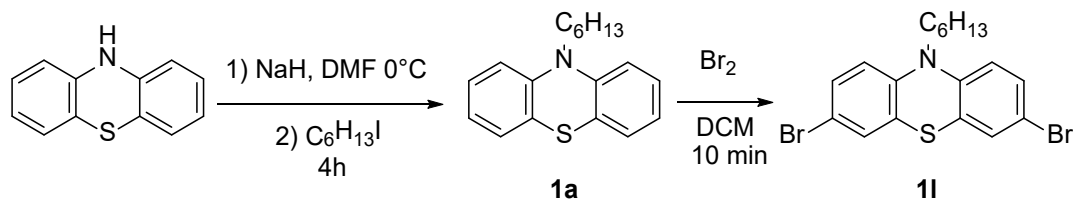
Scheme 19. General Scheme of the Buchwald Polymerization.

6 SYNTHESIS AND CHARACTERIZATION OF SMALL MOLECULE BASED HTMs

6.1 Series 1

6.1.1 Synthesis

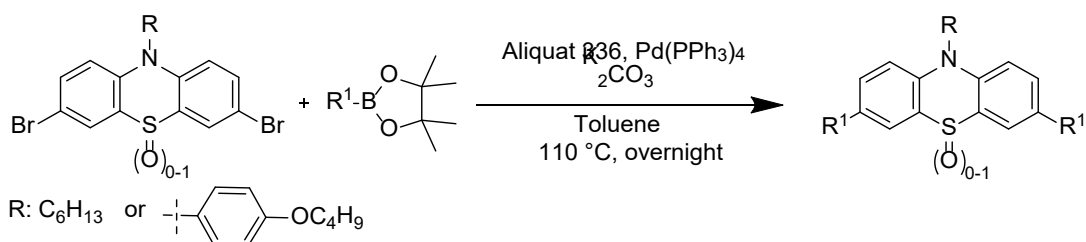
The organic molecules to be used as HTMs need to be soluble in organic solvents, in order to be deposited by spin coating of their solutions on the perovskite. To ensure the solubility, often alkyl chains are used, thus we planned to introduce a hexyl chain on the phenothiazine nitrogen (Scheme 20).



Scheme 20. Synthetic pathway to obtain the HTMs **1a** and **1l**. The HTM **1l** is also an intermediate to obtain the other HTMs of the series.

The compound **1a** was obtained by simple alkylation of phenothiazine with sodium hydride and 1-iodohexane in DMF from $0^\circ C$ to room temperature in just a few hours of reaction. Starting from **1a**, the dibromo derivative **1l** was obtained by a fast bromination (5-10 min) with bromine and dichloromethane and was both an HTM

by itself and an intermediate. The reactions to obtain **1a** and **1l** were performed up to a scale of 20 g and 10 g of starting material, giving a yield of 90 % and 93 % respectively. This proves the scalability of the proposed approach. Compound **1l** was then used in a Suzuki reaction as the key starting material to obtain the whole library of series **1** HTMs by cross-coupling with the boronic acids or boronic esters of the aryl moieties to be used as substituents on the main scaffold. The Suzuki protocol is a robust reaction which is also less harmful than others cross-coupling protocols. The cross coupling was thus performed using Pd(PPh₃)₄ as catalyst in presence of Aliquat 336 as a co-catalyst and potassium carbonate as base, in toluene at reflux for 12 h (Scheme 21). Those conditions were found to give good yields for **1a**, **1b**, **1c**, **1d**, **1e**, **1f** and **1k** of 90%, 67%, 94%, 74%, 67%, 57% and 80%, respectively. The reaction conditions were maintained also to prepare the HTMs of the series **2** and **3**.



Scheme 21. General synthetic method used for all the HTMs belonging to the three series **1**, **2** and **3**.

6.1.2 Characterization

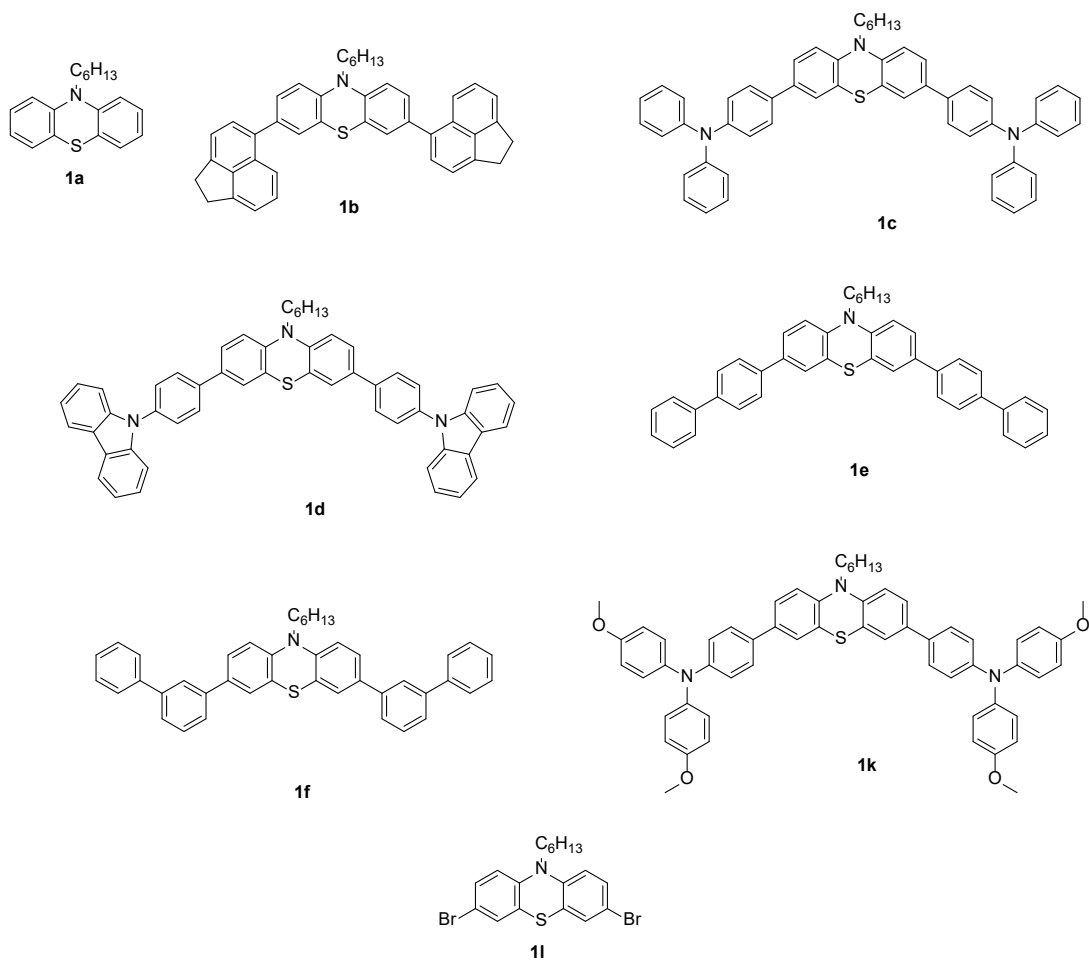


Figure 28. Chemical structures of the series 1 HTMs.

6.1.2.1 Absorption and emission through UV-Vis and Fluorescence spectroscopy

For the series **1** the compounds **1a**, **1b**, **1c**, **1d**, **1e**, **1f**, **1k**, **1l** were prepared. These products were characterized by UV-Vis (Figure 29) and fluorescence spectroscopy (Figure 30) to assess the transparency of the HTMs and to calculate their band gap. Notably, all compounds show wide bands, and only **1d** showed a fine structured band as a characteristic for systems based on carbazoles. The data are reported in Table 4. The electrochemical characterization, performed by cyclic voltammetry (CV) in DCM to obtain an estimate of the HOMO energy level of each HTM. Finally, the TGA thermal characterization assessed the thermal stability of the HTMs (Table 4). One should note that the values reported hereafter (and for the other series) are referred to pure materials. As a matter of fact, the employment of dopants (required for efficient charge transport in the working device) could induce some modifications in the measured properties: for example, (i) a slight modification of HTMs energy levels could be expected due to the creation of charge trap state and (ii) a decrease in thermal stability of HTMs, should be considered.

Compared to reference compound **1a** and **1l**, the functionalization in position 3 and 7 lead, except for **1k**, to a more pronounced absorption in the range 350-450 nm (Figure 29); yet this should not negatively impact on the AVT of the proposed

materials, once deposited as HTMs. Indeed, all the proposed materials have a band gap higher than 2.7 eV, completely fulfilling project's requirements.

Table 4. Optical, electrochemical and thermal characterization of small molecule HTMs of series **1**.

Compound	$\lambda_{\text{abs}}^{\text{a}}$ (nm)	$\lambda_{\text{onset}}^{\text{a}}$ (nm)	$\lambda_{\text{em}}^{\text{a}}$ (nm)	HOMO ^b (eV)	B_{g} (eV)	$T_{\text{Stab.}}^{\text{c}}$ (°C)	T_{g}^{c} (°C)
1a *	256	371	452	-5.01	3.3	-	-
1b	305	440	470	-5.40	2.8	375	80
1c	319	450	475	-5.28	2.7	391	88
1d	240	445	480	-5.35	2.8	399	121
1e	291	450	554	-5.39	2.7	395	n.a.
1f	248	436	472	-5.35	2.8	385	43
1k	313	324	472	-5.02	2.8	385	81

*a) Solvent: dichloromethane; b) CV measurements: HOMO determined from $E_{1/2}$ vs Ferrocene as standard; solvent: dichloromethane, supporting electrolyte: TBAPF₆; c) measurements performed under N₂. * the compound was obtained as an oil.*

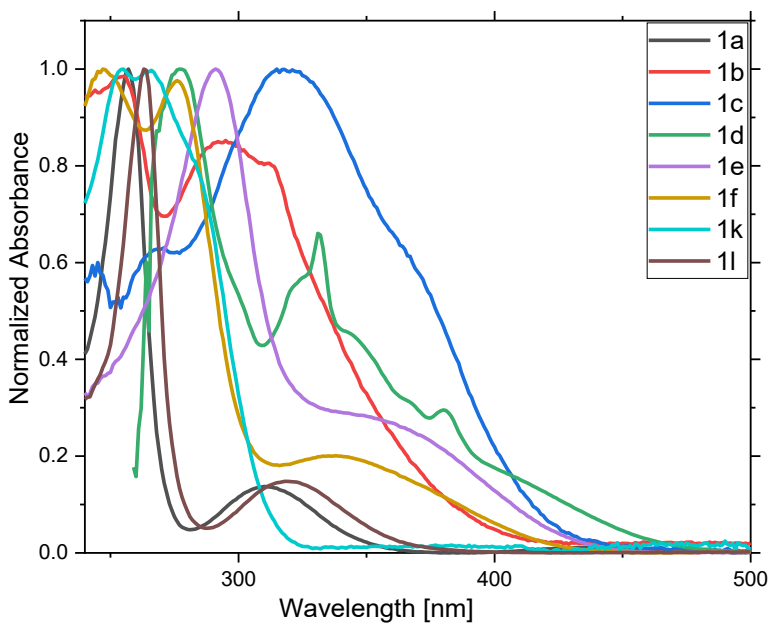


Figure 29. Absorption spectra in DCM for the compounds of the series **1**.

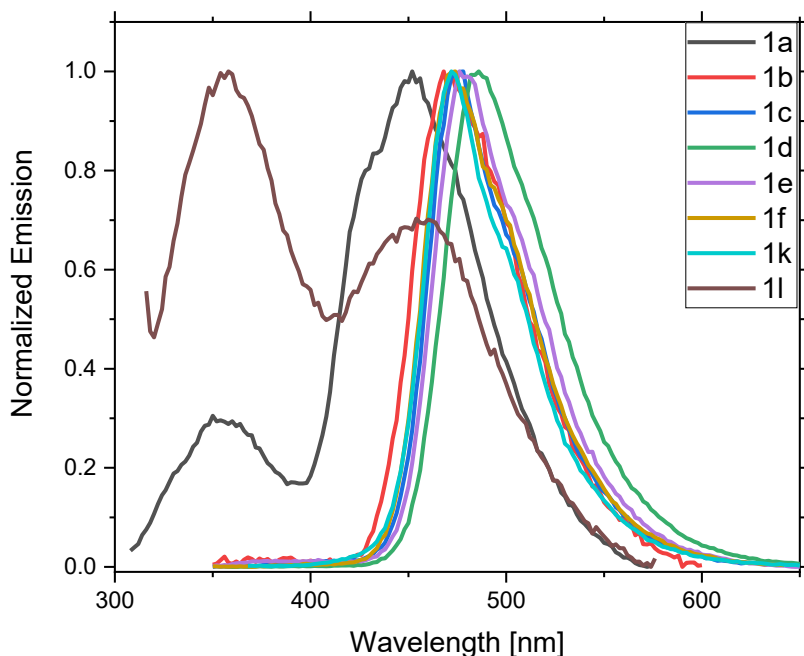


Figure 30. Fluorescence spectra in DCM for the compounds of the series **1**.

6.1.2.2 Electrochemical characterization through cyclic voltammetry

The electrochemical characterization, performed by cyclic voltammetry (CV) can be very useful to determine the oxidation potential of the molecule in solution, which is normally taken as a fair estimation for the determination of the HOMO of the molecule. For the CV measurements a glassy carbon electrode, a platinum wire and an Ag/AgCl electrode were employed as working electrode, counter electrode, and reference electrode, respectively; TBAPF₆ (0.1M in DCM) was used as supporting electrolyte and ferrocene as internal standard. The HOMO energy levels were

calculated through the formula $E_{\text{HOMO}} = - (E_{[1/2, \text{ox vs. Fc}^+/\text{Fc}] } + 5.1)$. The molecules of series **1** showed a HOMO around -5.40 eV which was raised a bit by the introduction of the triphenylamine substituent (**1c**, -5.31 eV), as expected by its electron donating ability, or by the absence of any substituents (**1a**, - 5.01 eV) (Figure 31).

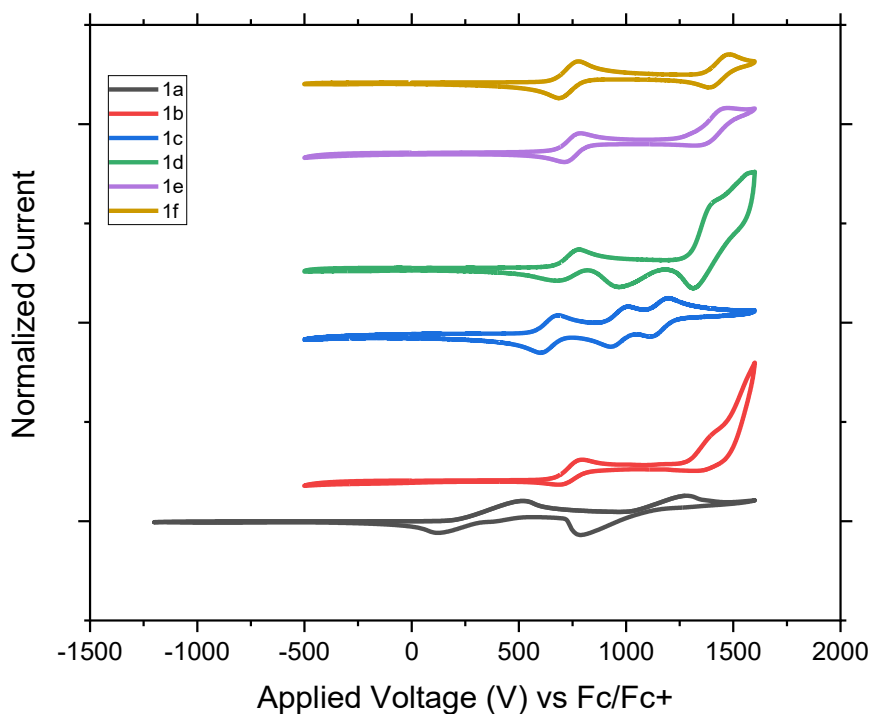


Figure 31. Electrochemical measurements (CV, Cyclic Voltammetry) for compounds of the series **1**.

6.1.2.3 Thermal Stability through TGA and DSC

The thermal stability of all the HTMs (considered as the temperature at which the material lost the 5% of its initial weight) was remarkable, with very high values for **1c** and **1e**, approaching 400°C (Figure 32). The compounds showed a T_g ranging in between 43°C - 121°C (Figure 33). A very low or very high T_g (i.e. outside of the working temperature experimented by the device) can be useful for final devices since they should not be affected by the heating occurring during operative conditions.

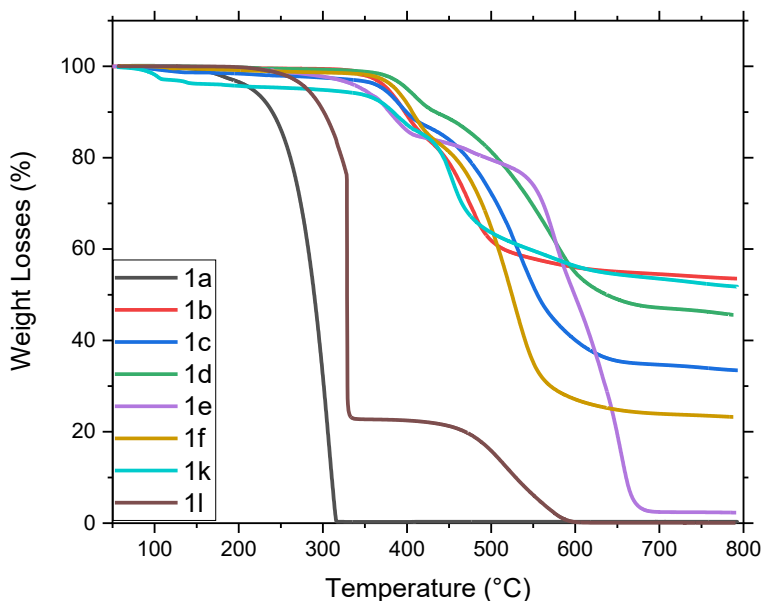


Figure 32. TGA graphs of the compounds of the series **1**.

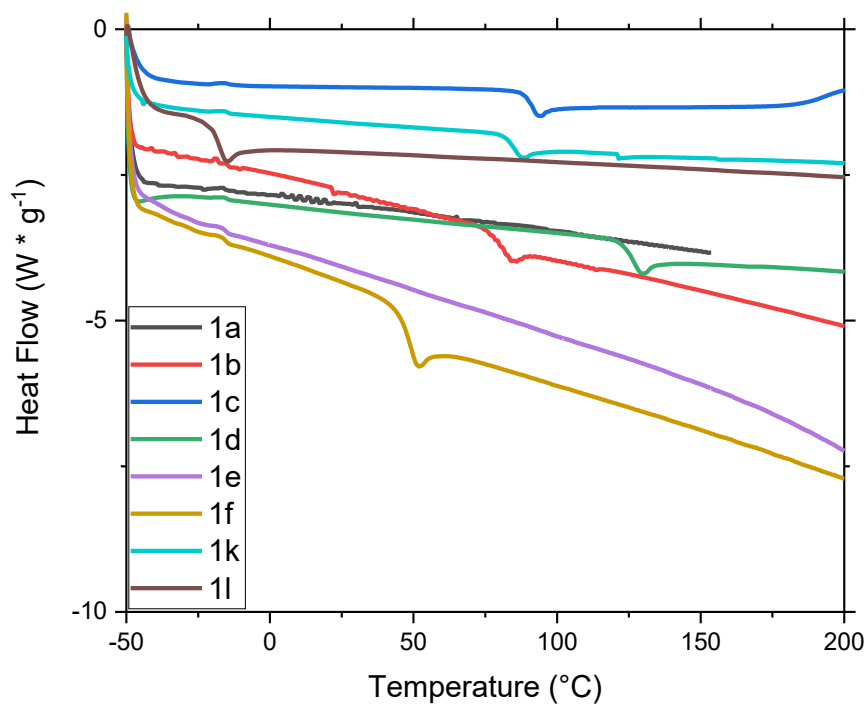
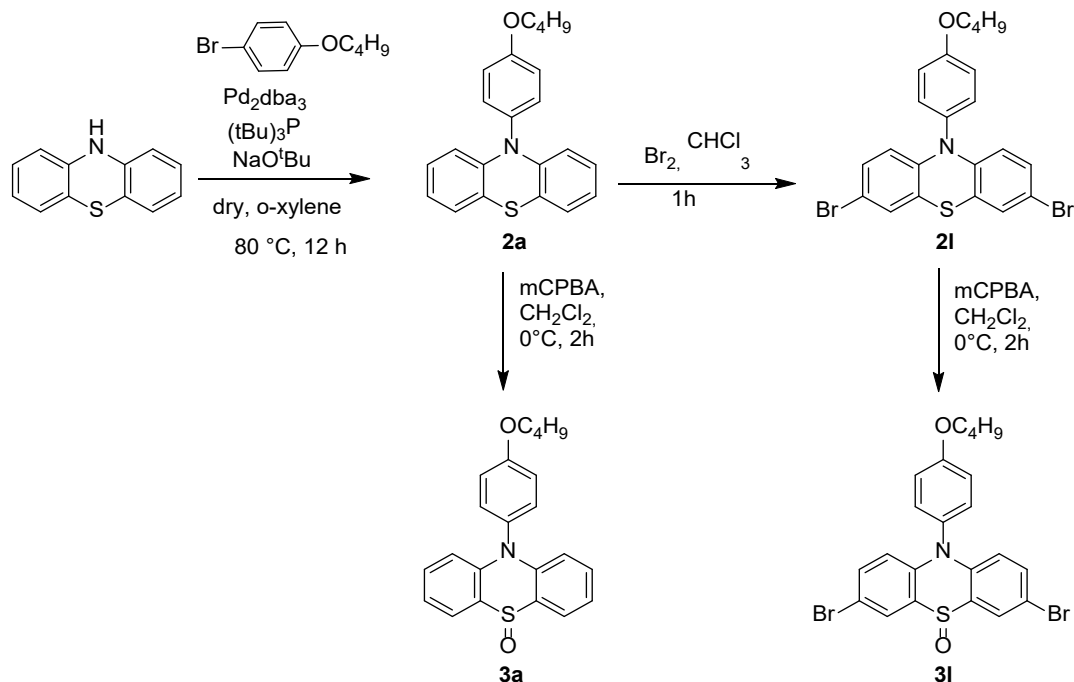


Figure 33. DSC graphs of the compounds of the series 1.

6.2 Series 2 and 3

6.2.1 Synthesis

Based on the first series **1** it was of interest to replace the alkyl moiety onto the nitrogen of phenothiazine with an aromatic one. This modification introduces a triarylamine-like nature directly into the central core. Since both phenothiazine and triarylamine compounds are easily oxidized, this kind of structure should be an opportunity to further tune HTMs electronic properties. On this basis, the scaffold for the series **2** was prepared by inserting a 4-butoxyphenyl group (Scheme 2 2). The selection of butoxy-substituted moieties would improve the solubility of the whole materials. This scaffold was further modified by the sulfur oxidation to give a sulfoxide. This modification heavily changes the heterocyclic nature, from electron donor (series **2**) to electron acceptor (series **3**), thus lowering the HOMO energy level consistently (*vide infra*).



Scheme 22. Synthetic pathway to obtain the HTMs **2a**, **2I**, **3a** and **3I**. The HTMs **2I** and **3I** are also intermediates to obtain the other HTM of those series.

Analogously to series **1**, the first step was the functionalization of the phenothiazine nitrogen, in this case with an aromatic substituent. The reaction was performed following the Buchwald-Hartwig protocol, with 4-bromobutoxybenzene, Pd₂dba₃ as catalyst, the tri(tert-butyl)phosphine) ligand and sodium tert-butoxide as base, in xylene at 80 °C for 12h. The HTM **2a** was obtained with a 75% yield. This compound was easily converted into the dibromo derivative **2I**, as we did for the case of **1I**, with a 95% yield. These two reactions were performed up to a scale of 5 g of starting material, to be ready for a possible scale-up. The series **3** is based on the compound **3a**, which can be obtained directly from **2a** as a sulfoxide, by the sulphur oxidation

performed with *m*-chloroperbenzoic acid at 0°C for 2h. In order to obtain the dibromo derivative **3l**, the best approach was to oxidate the compound **2l** to **3l**, instead of oxidating first **2a** to **3a** followed by bromination to **3l**. Starting from compounds **2l** and **3l** as starting materials and by applying the reaction already reported in Scheme 23 for the HTM of series **1**, several compounds were obtained: **2a-2l** and **3a, 3c, 3d, 3i** and **3l**.

Table 5. Optical, electrochemical and thermal characterization of small molecule HTMs of series **2** and **3**.

Compound	Yield%	$\lambda_{\text{abs}}^{\text{a}}$ (nm)	$\lambda_{\text{onset}}^{\text{a}}$ (nm)	λ_{em}	HOMO (eV)	B_{g} (eV)	$T_{\text{stab.}}^{\text{c}}$ (°C)	T_{g}^{c} (°C)
2a	80	325	396	448	-5.35	3.2	281	-5.6
2b	67	305	440	468	-5.41	2.8	388	108
2c	80	322	460	468	-5.34	2.8	407	115
2d	88	293	455	477	-5.48	2.8	403	142
2e	64	297	460	478	-5.38	2.7	425	95
2f	72	281	450	465	-5.32	2.8	407	64
2g	42	283	449	462	-5.36	2.8	355	48
2h	30	254	436	459	-5.35	2.8	345	47
2i	50	290	465	482	-5.43	2.7	380	61
2j	44	296	461	478	-5.34	2.7	402	88
2k	84	329	460	476	-5.01	2.7	409	103
2l	97	330	424	461	-5.52	2.9	332	n.a
3a	80	267	361	488	-5.95	3.4	297	n.a
3c	50	365	413	424	-5.60	3.0	378	129
3d	46	345	386	415	-5.62	3.2	418	178
3i	40	341	376	415	-5.55	3.3	299	101
3l	90	287	369	387	-6.13	3.4	277	n.a

a) Solvent: dichloromethane; b) CV measurements: HOMO determined from $E_{1/2}$ vs Ferrocene as standard; solvent: dichloromethane, supporting electrolyte: TBAPF₆; c) measurements performed under N₂.

6.2.2. Characterization

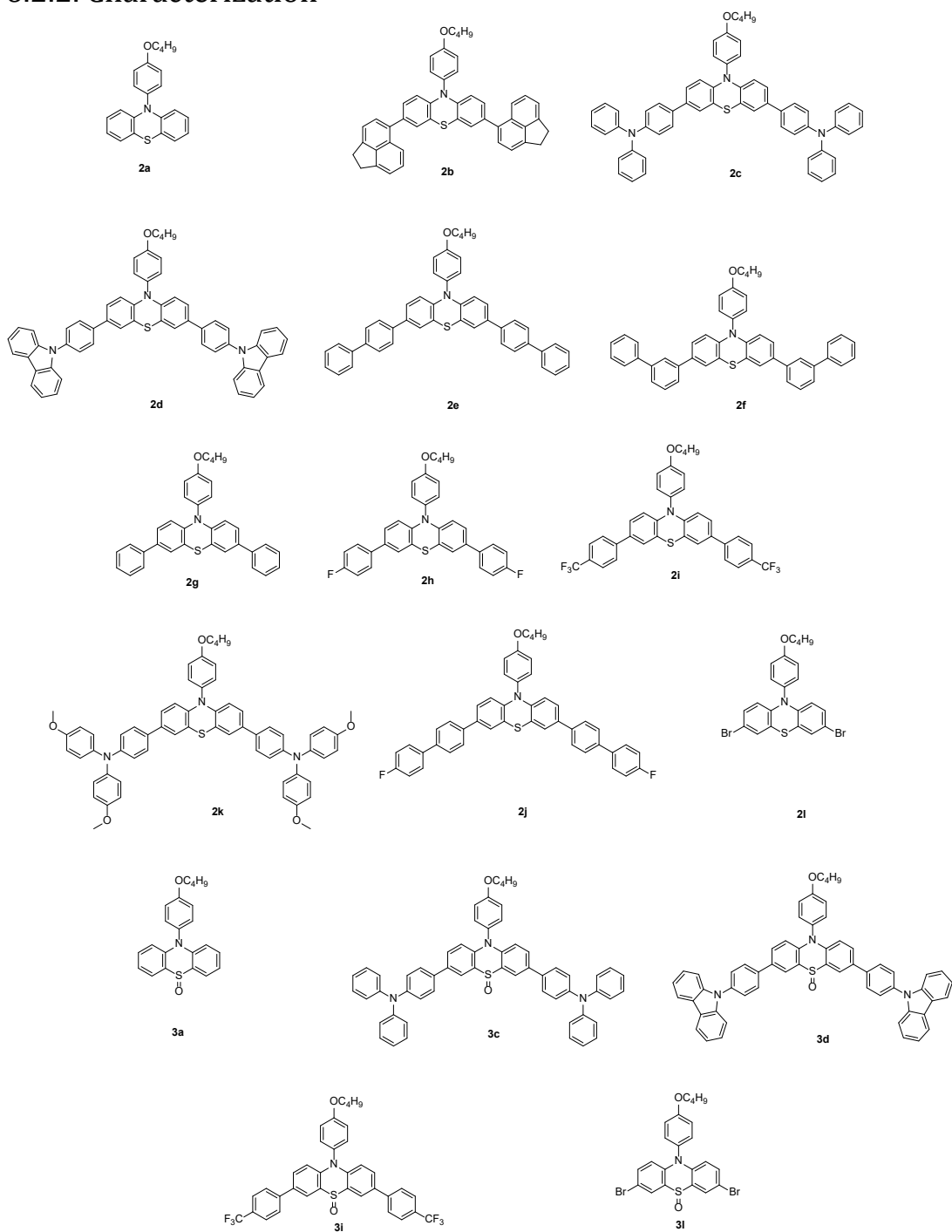


Figure 34. Chemical structures of the series 2 and 3 HTMs.

6.2.2.1 Absorption and emission through UV-Vis and Fluorescence spectroscopy

As already demonstrated for series **1**, even in the case of series **2** and **3** the UV-Vis measurements showed that nearly all compounds fulfill the transparency requirements, having practical null absorption above 450 nm (Figure 35 and Figure 37, Table 5). Only a few compounds slightly exceeded this limit, up to 460 nm (**2c**, **2e**, **2k**) and 465 nm (**2j**), but showing minimal absorption at that wavelength. In general, the absorption of compounds of the series **3** are shifted towards the UV region, at lower wavelengths, due to the oxidation of the sulphur atom. The band gap is also high, at least 2.7 eV for series **2** and even 3.0 eV for series **3**. A such high band gap ensures transparency and the blocking of the back electron transfer from the perovskite to the HTM, thus limiting recombination processes at the interface.

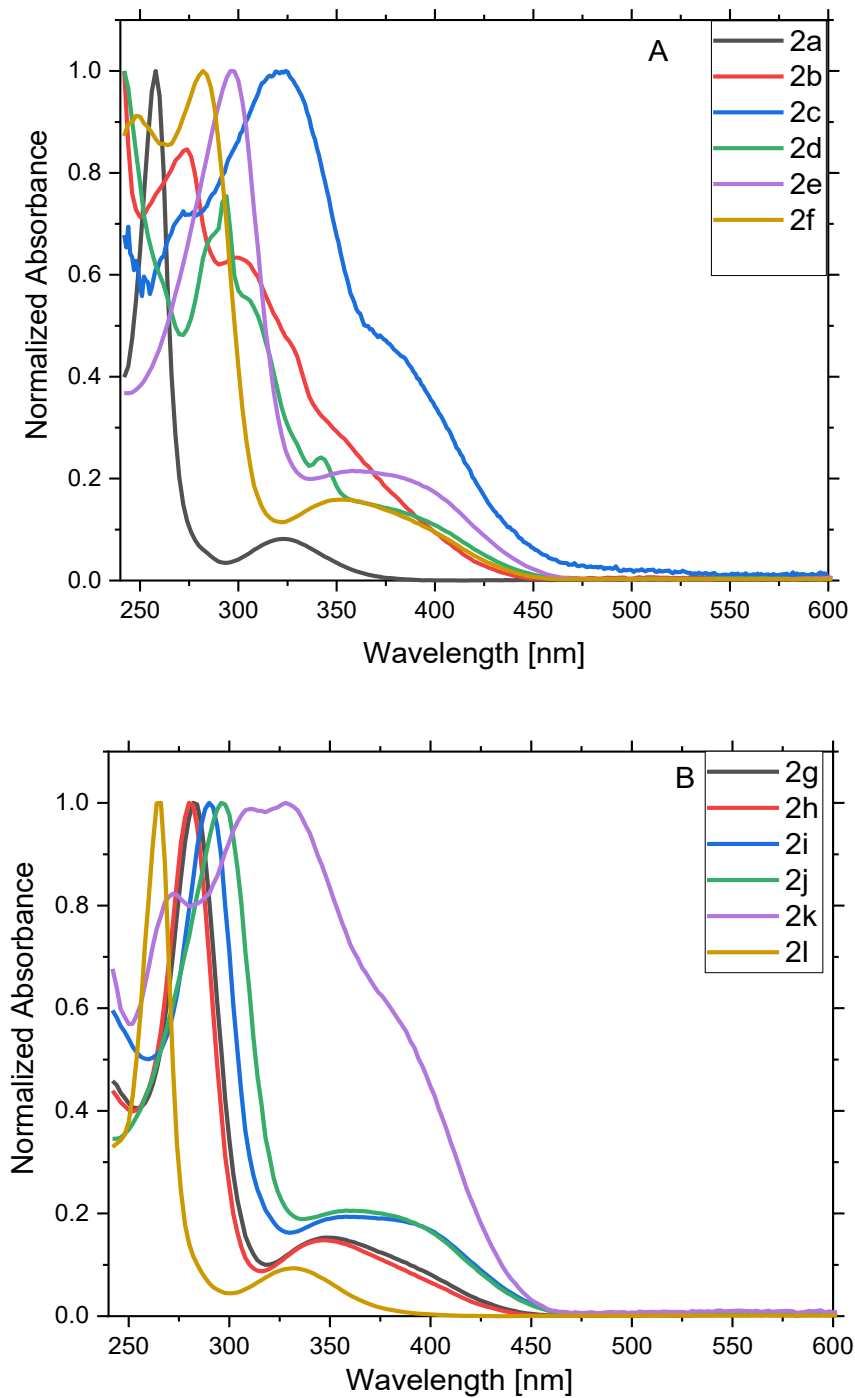


Figure 35. Absorption spectra in dichloromethane for the compounds of the series **2**.

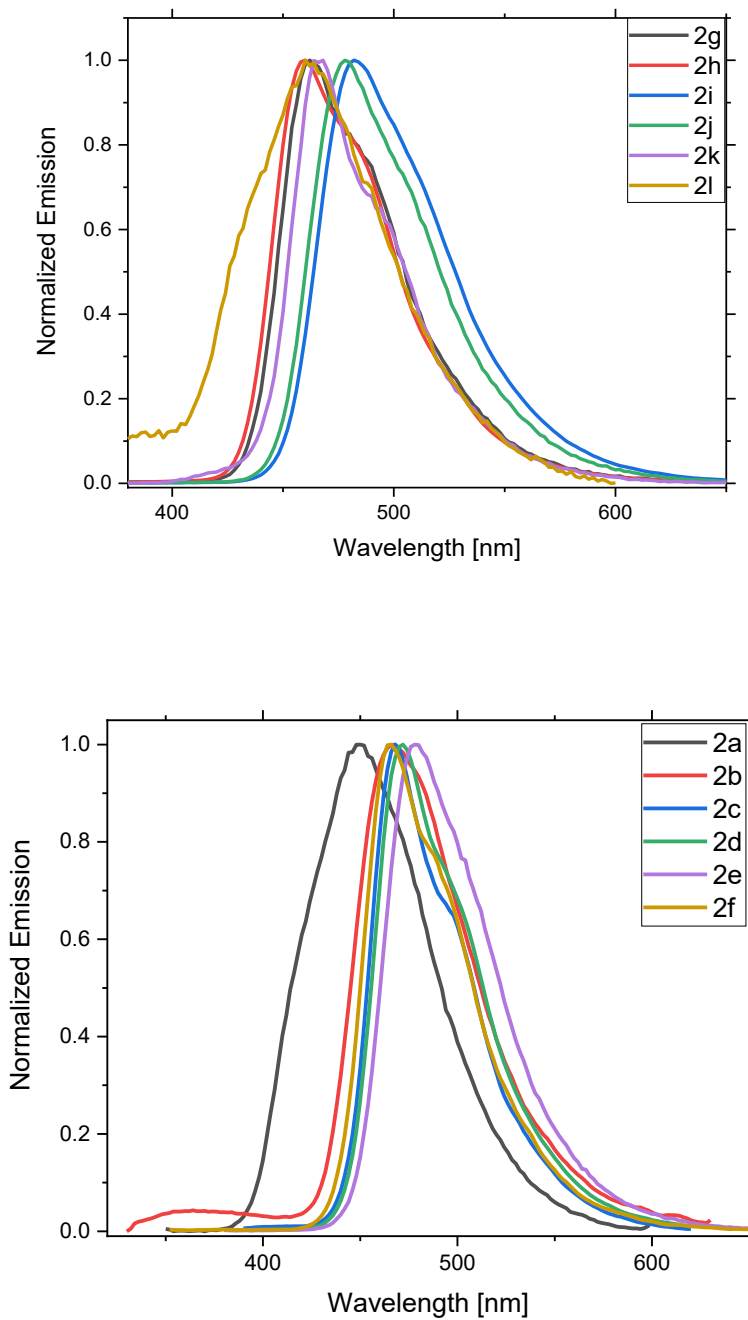


Figure 36. Absorption spectra in dichloromethane for the compounds of the series **2**.

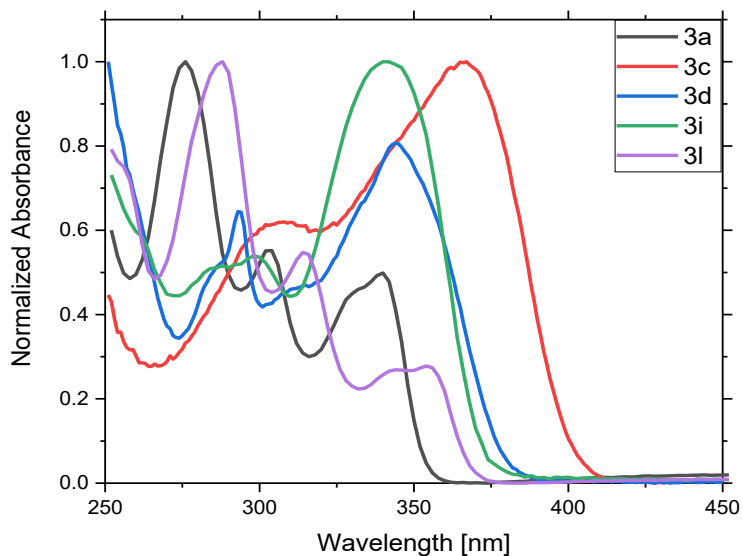


Figure 37. Absorption spectra in dichloromethane for the compounds of the series **3**.

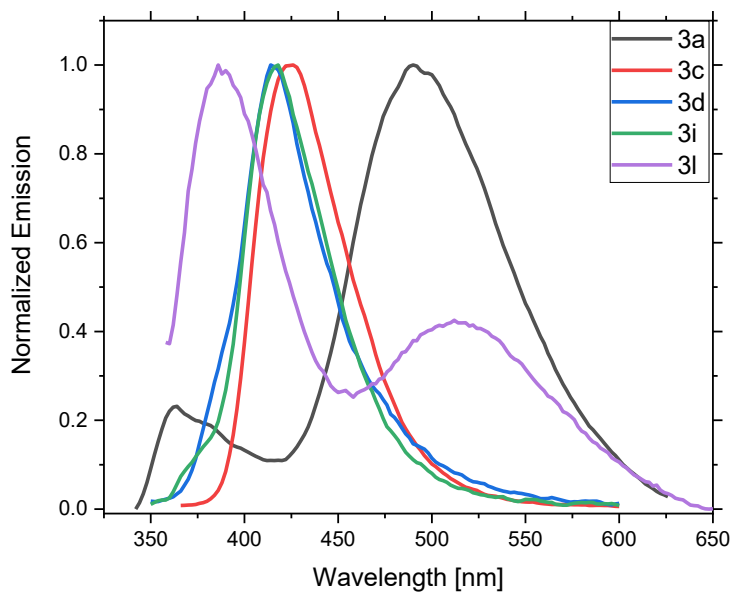


Figure 38. Emission spectra in dichloromethane for the compounds of the series **3**.

6.2.2.2 Electrochemical characterization through cyclic voltammetry

The electrochemical characterization showed that most substituents, namely for the compounds **2d-2h** and **2j**, made minimal modification to the HOMO of the unsubstituted reference material **2a** (HOMO at -5.35 eV), while in a few cases a more important effect in tuning the HOMO was found (Figure 35). In particular, the compound **2c** showed that the triarylamine substituent slightly raised the HOMO (HOMO at -5.34 eV). Other two substituents, the acenaphthene in **2b** and the trifluoromethylphenyl group in **2i** contributed to lower the HOMO (to -5.41 eV and -5.43 eV, respectively). A remarkable lowering of HOMO was obtained by the compound **2l** (-5.52 eV), bearing two bromine atoms. While the presence of halide atoms can sometimes be detrimental due to the formation of hole traps, the low HOMO of **2l** can be interesting to better match the valence band of wide band gap perovskites proposed within the project, especially those with mixed halides, such as MAPbI_{1-x}Br_x or MAPbBr_{1-x}Cl_x ones.

The series **3** was proposed just to further lower the HOMO (Figure 36) and extend the energy level tuning, aiming at finding the best matching with the perovskites used by the project partners. The HOMO of the few compounds prepared, namely **3a**, **3c**, **3d**, **3i** and **3l**, showed well lower HOMO energy levels, ranging in between -5.60 / -6.13 eV. The oxidation of the phenothiazine sulfur accounted for a reduction of 0.6 eV of the potential vs their series **2** counterpart (-5.35 eV for **2a** and -5.95 eV

for **3a**), which is consistent with the totally different nature of the scaffold (electron donor for **2a** and electron acceptor for **3a**). The use of the triphenylamine substituent in the compound **3c** raised the HOMO by 0.35 eV vs **3a** (to -5.60 eV), but with a 0.26 eV lowering vs **2c** (-5.20 V). The effect of the carbazole in **3d** was almost similar to that the triphenylamine group. Once more, the presence of the two bromine substituents lowered the HOMO and **3l** reached a very low energy level (-6.13 eV).

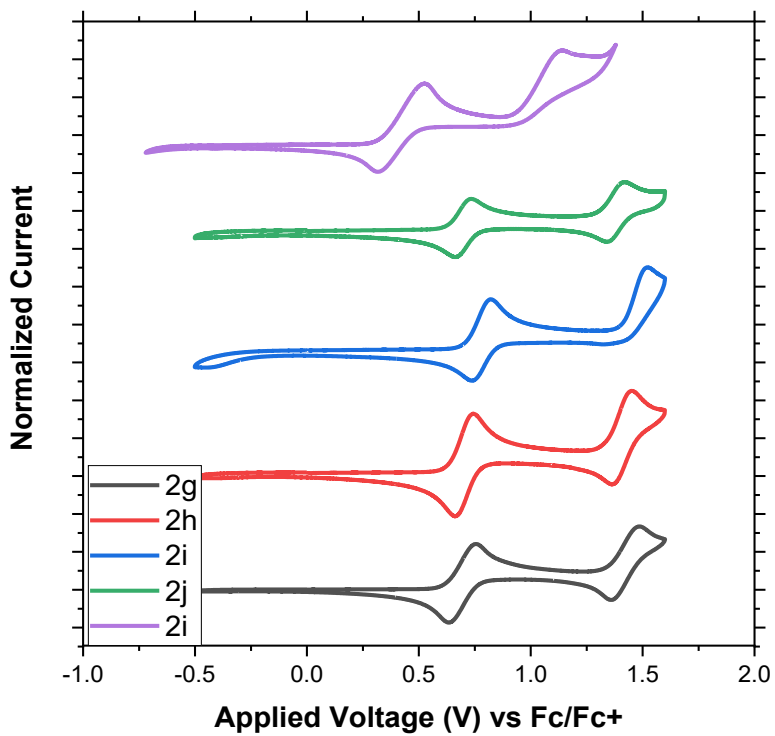
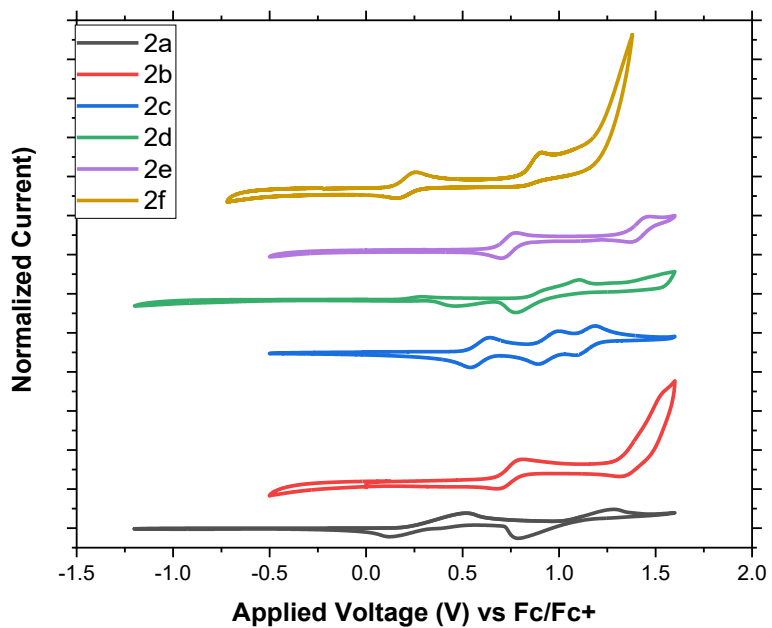


Figure 39. Cyclic voltammograms for the compounds of the series 2.

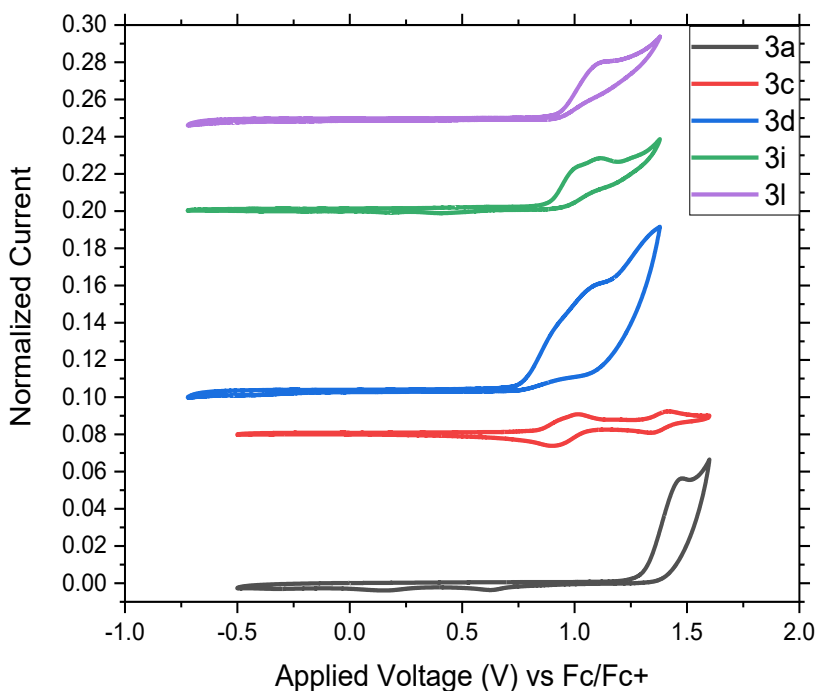


Figure 40. Cyclic voltammograms of the series **3**.

6.2.2.3 Thermal characterization

All HTM series, **1**, **2** and **3** showed an excellent thermal stability, in most cases in the range 350-425°C (Figure 41 and Figure 42). This is mandatory to survive the device production process and, even more important, to not jeopardize the device stability under operative conditions. Most of the compounds showed a T_g (Figure 43 and 44) in the range -6 °C of **2a** to 178°C with **3d**. According to device performance data obtained from **EPFL** (PCE of 7.5 % and the highest V_{oc} ($V_{oc} = 1.65$ V), vide infra), compound **2c** is the best candidate having T_g value of 115°C (Figure 43).

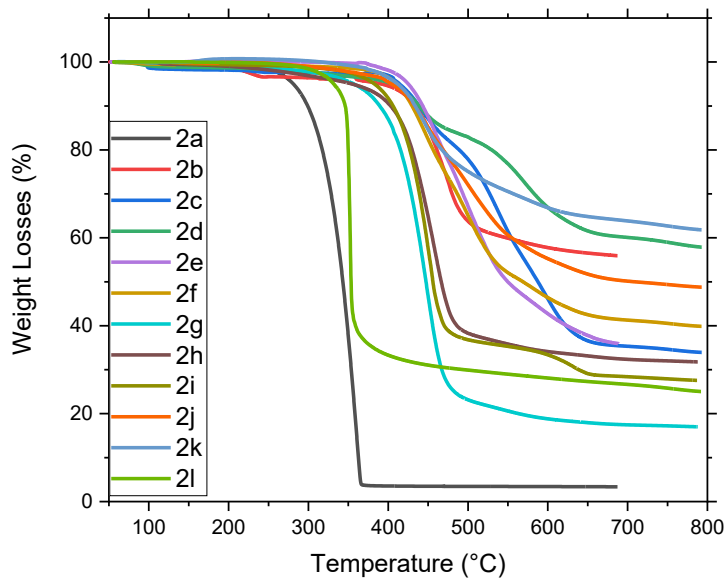


Figure 41. TGA of Series 2.

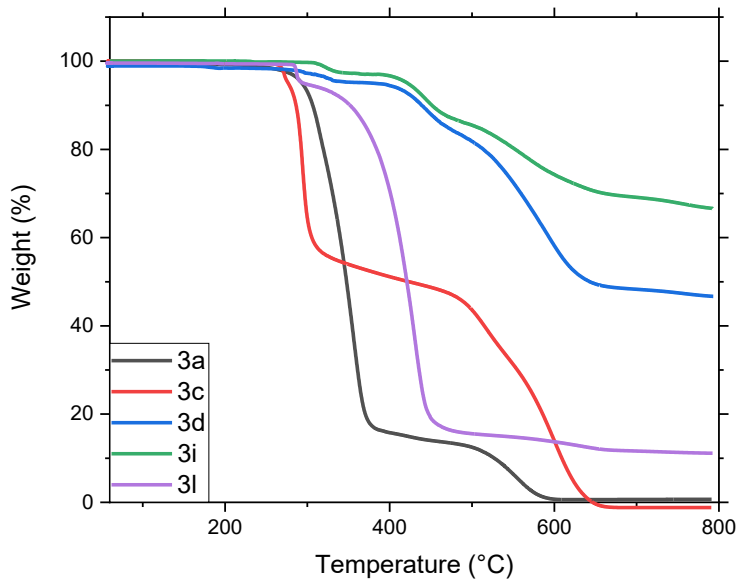


Figure 42. TGA of series 3.

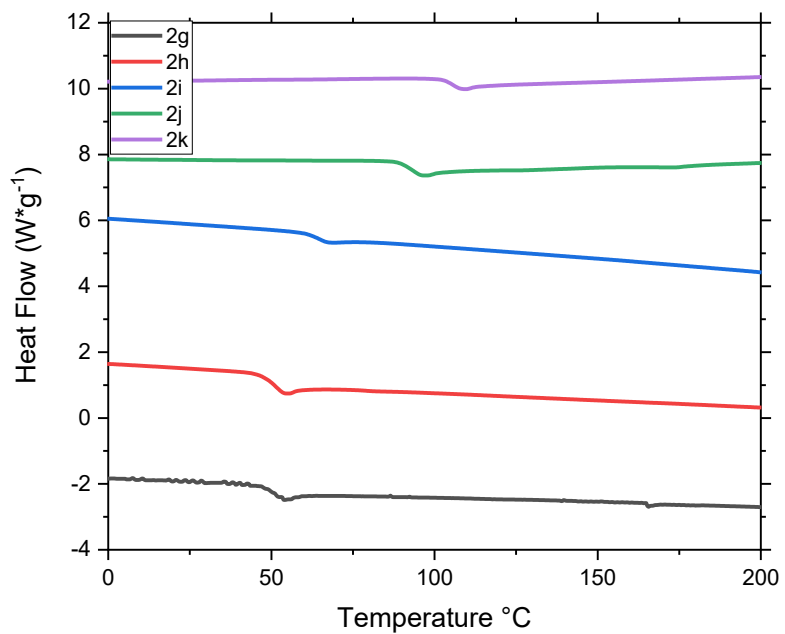
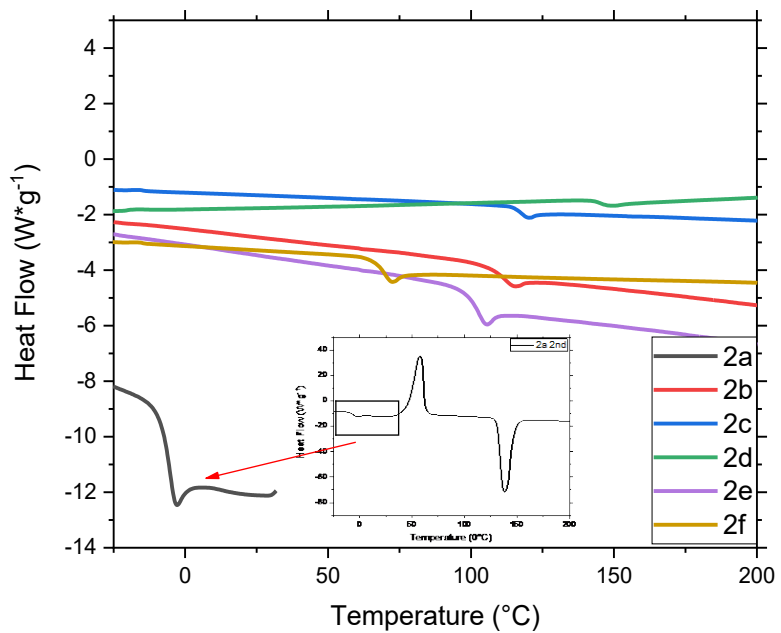


Figure 43. DSC second heating cycle of series 2.

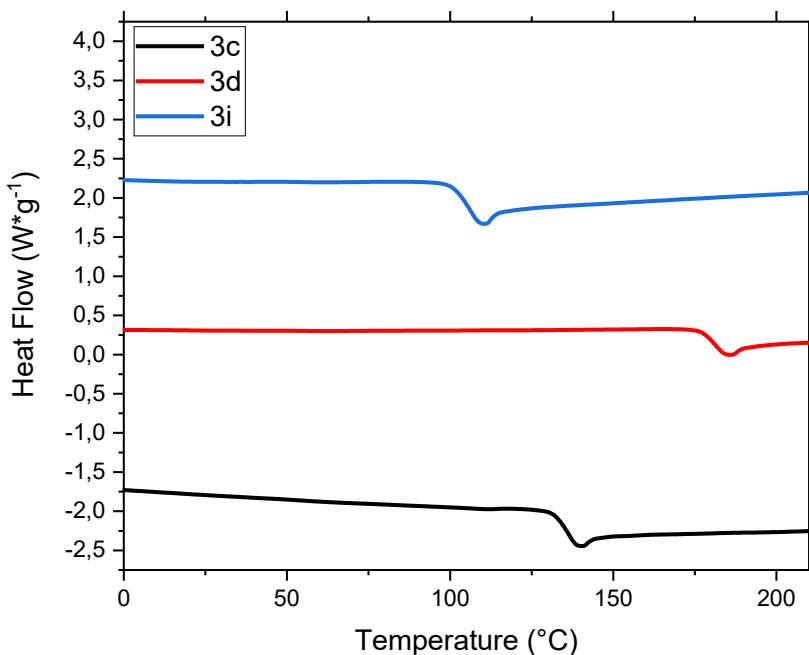


Figure 44. DSC second heating cycle of series **3**.

6.3 Conclusions

As a result, for the series **2** and **3**, a total of 17 HTMs were produced, in which the HOMO energy level could span from -5.20 eV to -6.13 eV, providing a wide library of materials, having tailored properties, to be tested in complete perovskite devices.

The choice of best compounds strongly depends on the nature of the absorbing layer, i.e., the perovskite absorber, since the HTM should match the perovskite energy level. From the point of view of transparency all the compounds meet the requirements. As far as the HOMO energy level, several compounds are compatible

with the level of the perovskite MAPbBr₃, selected by the partners, which have a valence band located at around -5.8/ -6.0 eV (Figure 45). Since also compound **3a** (HOMO at -5.95 eV) is well working in cells based on this perovskite (*vide infra*), it seems reasonable that the matching of energy level is well achieved.

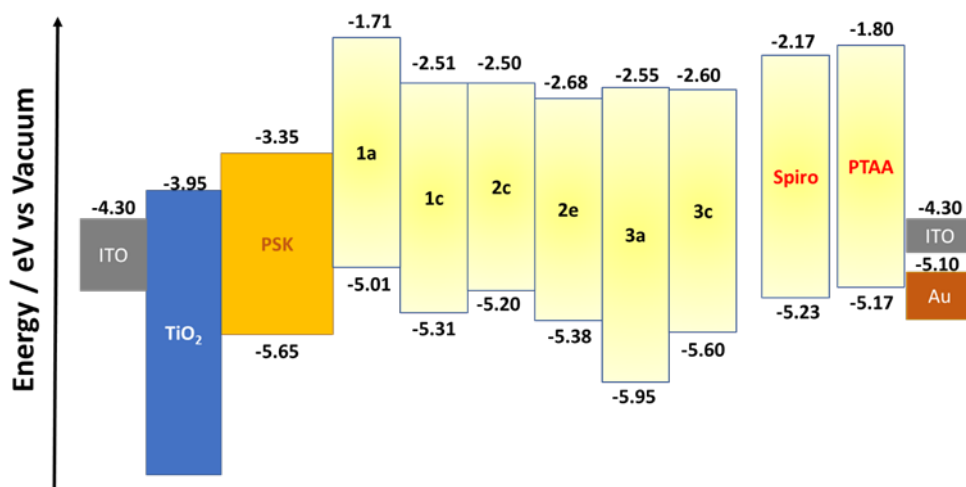


Figure 45. Frontier Molecular Energy Levels of selected HTMs compared to commercial one and the ones of other PSCs components.

To further prove the transparency of selected molecules (even in comparison with standard HTMs) we performed (with the help of partners at CHOSE) some absorption measurements of the deposited films. HTM films were deposited by spin coating on a glass slide. This approach was selected to avoid any spurious contribution to the absorption due to the other layers (ETL, PSK, etc.); one should note that the behavior in the final device could be slightly different depending on optical losses at the

interface (i.e. the glass/HTM one could not be compared to the PSK/glass one). Nevertheless, data reported showed that for compounds **2c** and **2e** an AVT values close to 90% could be found, higher compared to the reference (PTAA) and with only 1% loss compared to the bare glass. These results proved that a HTM with a $T > 85\%$ (much higher indeed) has been developed.

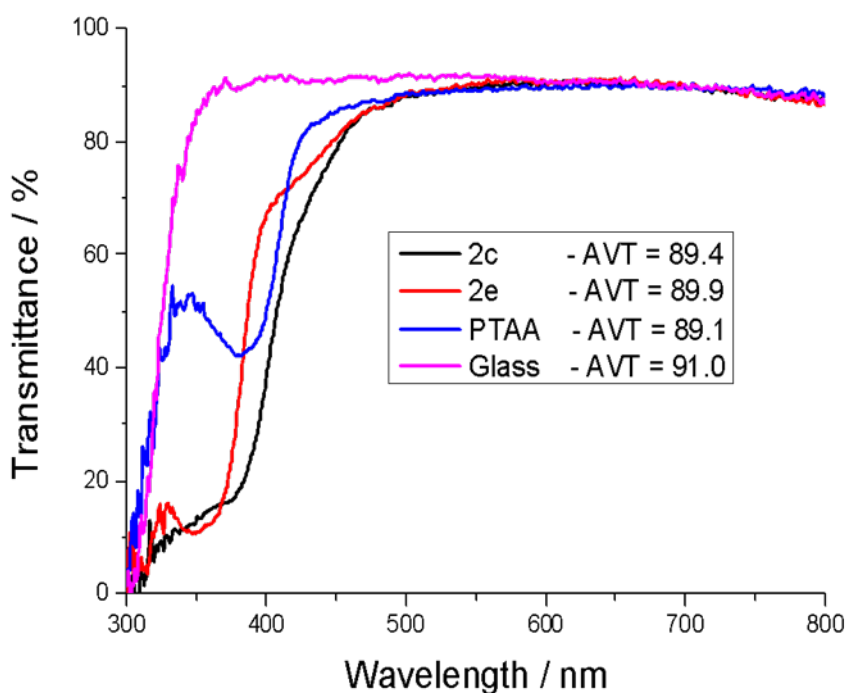


Figure 46. Transmission spectra of thin films of selected HTMs and the reference glass.

Material **2c** was selected as HTM to perform an initial screening on MAPbBr₃ based wide band gap perovskite devices. The perovskite composition has been described in a dedicated deliverable whereas the device architecture is the following:

Glass/FTO/CompactTiO₂/mesoporousTiO₂/MAPbBr₃/NPACl/Spiro HTL/Gold. The photovoltaic efficiencies reported are really promising, being highly reproducible (Table 6) and showing a limited hysteresis (see Figure 47 a); indeed, the latter is greatly reduced during the working period of the device as proved by the slight increase in PCE during the MPP tracking (Figure 47). IPCE measurement (Figure 47) further confirm the good performance of the devices and the cut-off at 540 nm.

Table 6. Photoelectrochemical parameters of PSCs employing **2c** as HTM.

Cell	V _{oc} / V	J _{sc} / mA*cm ⁻²	FF	PCE %
1	1.661	6.26	0.598	6.22
2	1.597	5.99	0.658	6.30
3	1.626	5.23	0.653	5.55
4	1.625	5.81	0.637	6.02
5	1.632	6.26	0.644	6.77
6	1.617	6.11	0.636	6.27
7	1.650	5.76	0.587	5.58
8	1.642	5.86	0.56	5.39
9	1.653	5.87	0.593	5.76
10	1.647	5.89	0.569	5.52
11	1.651	5.91	0.610	5.95
12	1.655	6.01	0.587	5.83
13	1.656	6.02	0.598	5.98
14	1.658	5.97	0.543	5.37
15	1.654	5.87	0.535	5.24
Averaged	1.642	5.92	0.601	5.85
Deviation	0.015	0.16	0.031	0.34

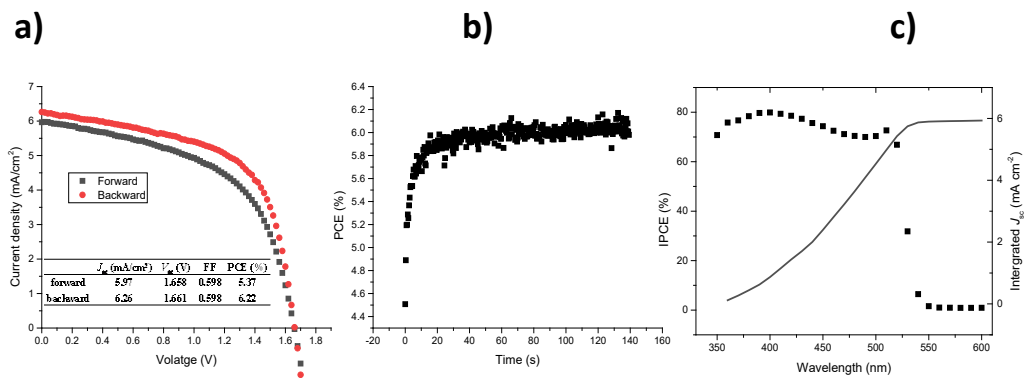


Figure 47. Photoelectrochemical characterization of a PSK devices with **2c** as HTM: (a) JV curves, (b) Maximum Power Point tracking and (c) IPCE spectrum. The selected device was the one having the higher V_{oc} (i.e. 1.66 V).

From further tests performed with optimized materials by the partners at EPFL, it appeared that in the series **2** the best performing compound is **2c** and **3a** in the series **3**. As an example, the best performances were achieved by the compounds **2a**, **2c** and **3a** that reached photovoltaic efficiencies (PCE) of 6.5%, 7.5% and 7.7%, respectively. Also important for the project targets is the achievement of an open circuit voltage (V_{oc}) of 1.65 V (Figure 48). This is not yet reaching the initially proposed target ($V_{oc} = 1.8$ V) but since the power output is higher than the target (PCE at least 6%), this could be sufficient for the project needs.

As specified above, the devices made by the partners at the EFPL employed gold as performing back electrode. Yet, gold is not transparent and to fulfil project's objectives it should be replaced by a transparent back contact. At this purpose, partners at CHOSE (Center For Hybrid And Organic Solar Energy, University of Tor

Vergata, Rome, Italy) built up a cell using indium tin oxide glass (ITO) to replace gold obtaining very promising (albeit lower) efficiency, showing a PCE close to 5% and a V_{OC} higher than 1.40 V. The lower efficiency compared to gold-based device are likely due to not optimized HTM/Back contact interface. This point is under investigation to obtain very efficient semi-transparent PSCs to be implemented in tandem devices.

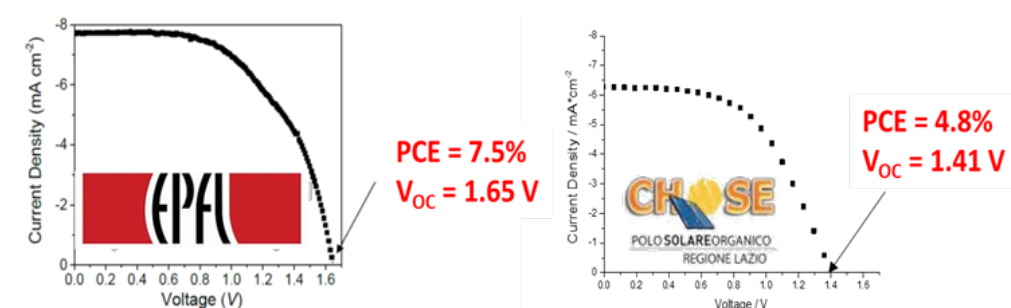


Figure 48. Photovoltaic characterization for the devices based on compound **2c**, best compound selected among the HTMs of the project.

6.4 Effect of slight modifications of the triphenylamine unit on the HTMs properties and performance

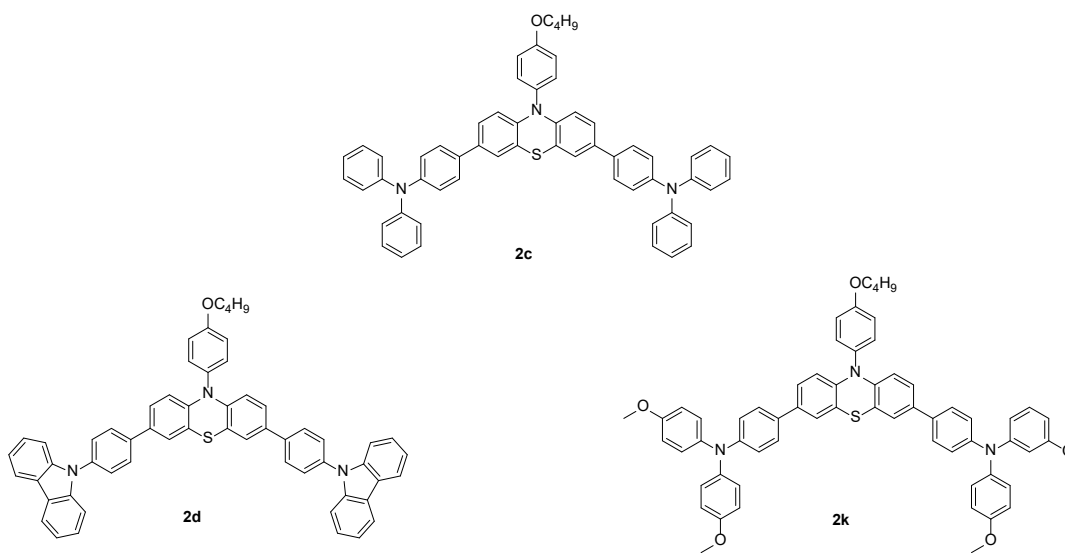


Figure 49. Chemical structures of the **2c**, **2d** and **2k** HTMs.

6.4.1 Absorption and emission through UV-Vis and Fluorescence spectroscopy

The recorded UV-Vis Spectra (Figure 50) of **2c**, **2d** and **2k** exhibit absorption peaks in the ultraviolet region (<350 nm) as result of electronic transition occurring due to the interaction of radiation with the three HTMs. The optical band gap of the HTMs can be calculated through the intersection point of the absorption curve with the baseline.¹⁸⁴ For **2c**, one main absorption peak occurs centered at 323 nm with two shoulder peaks one at 271 nm and the other one at 382 nm. In the case of **2d** we

found a blue shifted spectra due the presence of carbazole unit instead of TPA unit. We observed 3 main peaks, the main one at 236 nm, the second one at 293 nm with two shoulder peaks at 283 nm and 309 nm and the third peak at 343 with a further shoulder peak at 384 nm. The blue shift of **2d** comparing to **2c** is due to the extra chemical bond between the phenyl units of the carbazole lead to noticeable hypochromic effect on the absorption of UV-Vis. The optical band gaps (E_g) of **2c**, **2d** and **2k** are 2.81 eV, 2.86 eV, respectively.

When analyzing **2k** behavior, we got three main peaks at 272 nm, 310 nm, and 328 nm with a shoulder peak at 381 nm. It appears that the presence of the methoxy groups at the two para positions in the diphenylamine unit lead to three main peaks instead of one peak as in **2c** molecule, in which the methoxy groups at para positions are lacking. Besides, the presence of the methoxy group in para position leads to a red shift effect on the UV-Vis spectra, which was also reported in literature.¹⁸⁵

The recorded fluorescence spectra for **2c**, **2d** and **2k** are showing peaks at 467 nm (shoulder peak at 494 nm), 472 nm (shoulder peak at 496 nm) and 467 (shoulder peak at 494 nm), respectively. It is clear that the presence of a chemical bond between two phenyl units in carbazole (with respect to a diphenylamine) leads to a slight red shift in emission spectra as it forms a more polar excited state comparing to the ground state.

The three HTMs **2c**, **2d** and **2k** showed Stokes shifts of 144 nm, 235 nm, and 132 nm, respectively, and these values are relatively high comparing to the Stokes shift value of Spiro-OMeTAD which is only 33 nm. These high values of stokes shift indicates that the three HTMs can undergo large geometrical change upon excitation and thus a good molecular flexibility of the excited state. This can improve the pore filling the HTM in mesoporous systems like mesoporous TiO₂ in DSSCs or among perovskite grains in PSCs.¹⁸⁶

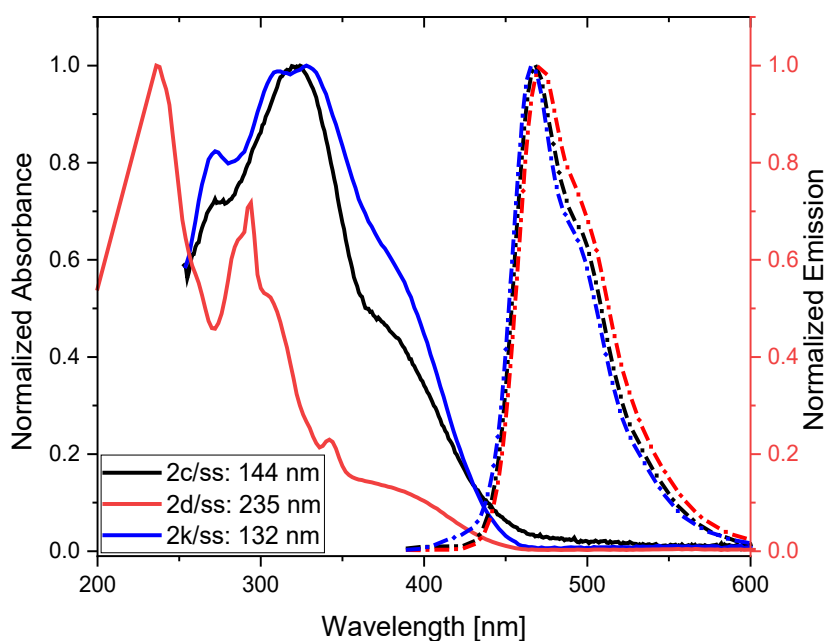


Figure 50. UV-Vis and fluorescence spectra of the **2c**, **2d** and **2k** HTMs.

6.4.2 Electrochemical characterization through cyclic voltammetry

The oxidation potential of the HTMs were obtained through cyclic voltammetry (Figure 51). Generally, there is a relationship between the open circuit voltage (V_{oc}) of the perovskite solar cell and the energy level matching of the HTM and the perovskite. Provided that the HOMO of the HTM is higher in energy than the perovskite CB, the lower the HOMO of the HTM the better, and the better the energy level matching the higher the open circuit voltage. When the HTM HOMO energy level is very close to the valence band of the perovskite, a low V_{oc} is obtained. This is often due to a real mismatch of the levels, since in the solid-state film the HOMO of the HTM can be slightly downshifted and can be even lower than the perovskite CB, thus hampering the correct hole transfer from the perovskite to the HTM. As a matter of fact, to obtain a good energy level matching, the HOMO energy level should be 0.2 eV higher than the perovskite valence band (VB), which ensures a thermodynamic driving force for the process of hole mobility to take place rapidly.

The highest occupied molecular orbitals (HOMOs) energy levels of the HTMs **2c**, **2d** and **2k** were obtained using cyclic voltammogram (CV) as indicated in figure 47 through the formula $E_{HOMO} = (E_{[1/2, ox vs. Fc^+/Fc]} + 5.1)$. Regarding these data, the HOMO values of the HTMs **2c**, **2d** and **2k** are -5.34 eV, -5.48 eV and 5.01 eV, respectively. It is so clear why **2c** is giving the best V_{oc} of 1.63 V which is close to the value of the state of art Spiro-OMeTAD, (-5.22 eV)¹⁸⁷.

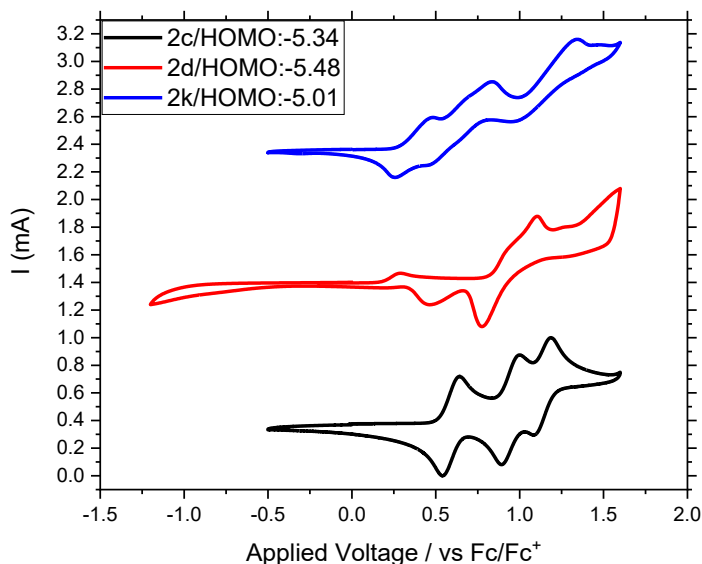


Figure 51. Cyclic voltammograms of the **2c**, **2d**, **2k** HTMs.

6.4.3 Thermal Stability through TGA and DSC

Glass transition (T_g) is a valuable tool to assess the stability of perovskite solar cells. It is important to obtain HTMs with high glass transition as one of the reasons of the fast degradation of the PSCs is the transformation of the metastable amorphous state of the HTM during the operation of the device. The obtained results of T_g , T_m , and T_{stab} are summarized in Table 7 and Figure 53. From the graphs in Figure 54, during the 1st heating cycle (red color downside), **2c** exhibited only a sharp endothermic melting point at 208 °C (melting point is the point where the crystallinity order is destroyed) which proves the pure crystallinity of **2c**. For **2d** and **2k** in the first cycle only a molecular relaxation was observed, which appeared as a weak endothermic transition near the glass transition at 142 °C and 103 °C for **2d**

and **2k** respectively. This confirms the amorphous state of the **2d** and **2k**. It seems that the simple presence of an additional bond connecting two phenyl moieties in the phenylcarbazole unit (**2d**), compared to the normal triphenylamine unit (**2c**), induces a more amorphous character for **2d** vs **2c**, this is because the additional bond strongly limit the freedom of movement of the end group, leading to a structure which are less flexible that also remains partially interactive after higher molecular movement, which leads finally to an amorphous structure.¹⁸⁸ As a result, the presence of the methoxy groups at 4- and 4'- positions in the 4,4'-dimethoxytriphenylamine unit makes **2k** to behave as an amorphous HTM These DSC data indicates that a minimal change in the structure of the triphenylamine substituent on phenothiazine core can severely affect the morphology of the HTMs in the solid state.

After cooling the isotropic liquid in the cooling cycle, in the second heating cycle the T_g values were evidenced at 115 °C, 143 °C and 103 °C for **2c**, **2d** and **2k**, respectively (Figure. 53). For, **2c** the melting point disappeared in second heating cycle and the HTMs became amorphous with a T_g of 115 °C. The higher glass transition of **2d** (143 °C) comparing to of **2c** (115 °C) emphasizes the structural differentiation of phenylcarbazole unit and triphenylamine unit. The chemical bond among the 2 phenyl units in the carbazole, results into a substance with high level of organization and structure in the liquid form phase comparing to triphenylamine, leading to more

rigid molecules which should present more stable and strong intermolecular interactions. This indicates that the intermolecular bonding disruption during the fusion transition is more related to TPA.¹⁸⁸ As a final result, the presence of the methoxy groups at 4- and 4'- positions in the 4,4'-dimethoxytriphenylamine lowers the T_g of **2k** comparing to **2c** which is not substituted with the methoxy groups.

The thermogravimetric analysis (TGA) of **2c**, **2d** and **2k** (Figure 52) showed the temperatures of 407 °C, 403 °C and 407 °C, respectively, at 5% weight loss, which indicates an excellent thermal stability and that the modification of the triphenylamine unit structure does not influence it too much since only a slight decrease of 4 °C was noticed for **2d**. At 800 °C, due to their structural modifications, **2d** and **2k** retained around 60% of the initial weight while **2c** only retained 35% of the initial weight.

Thus, we have demonstrated that a minor change in the triphenylamine substitution unit dramatically influences the molecular geometry and optoelectronic parameters of the HTMs to be used in perovskite solar cells.

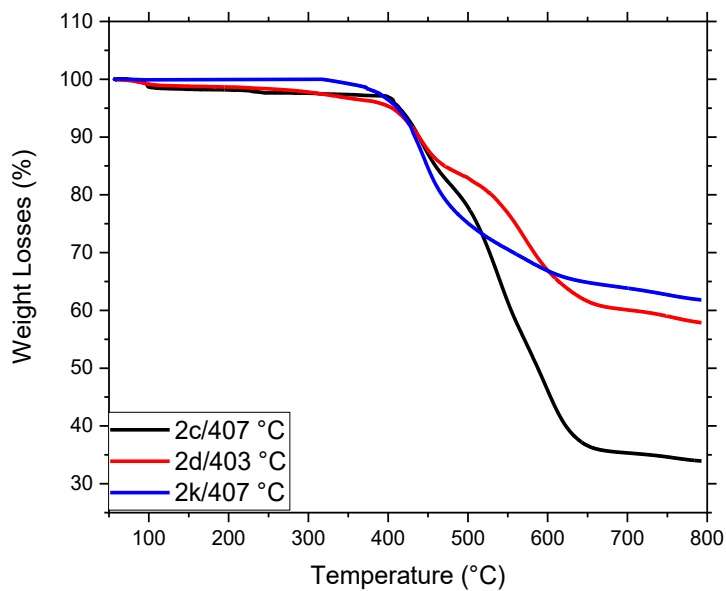


Figure 52. TGA of the 2c, 2d and 2k HTMs.

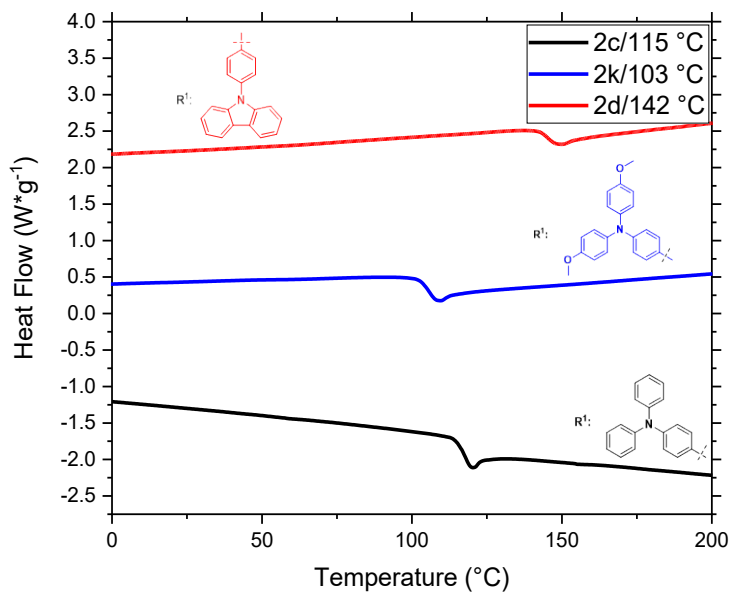


Figure 53. DSC second heating cycles of the 2c, 2d and 2k HTMs.

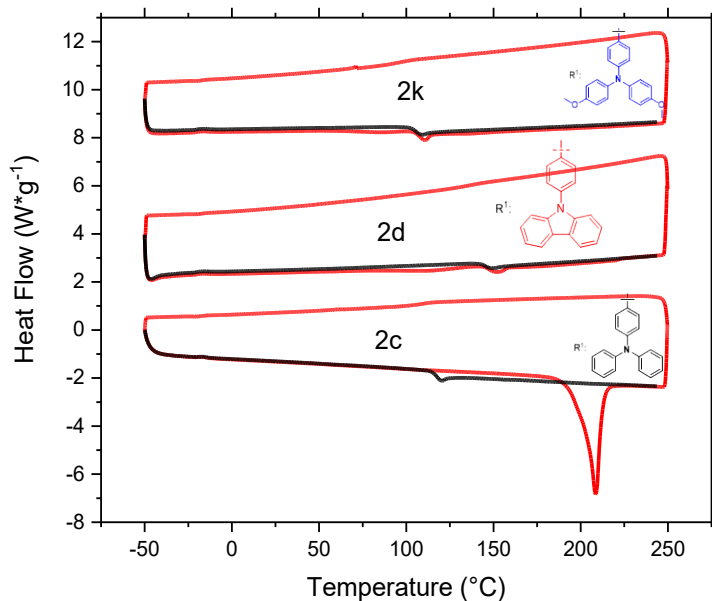


Figure 54. DSC of the **2c**, **2d** and **2k** HTMs, down red color is the first heating cycle and upper red color first is the first cooling cycle, while black is second heating cycle.

6.4.4 Photovoltaic efficiencies of selected compounds **2c**, **2k** and **2d**

HTMs **2c**, **2d** and **2k** were tested on PSCs with MAPbBr₃ perovskites along with the state-of-art standard Spiro-OMeTAD (Figures 55, 56, 57 and 58 for PCE, V_{oc}, FF and J_{sc} respectively). The three compounds performed quite well but their PCEs were lower than Spiro-OMeTAD (Table 7). One can appreciate, however some interesting trend. The best compound was **2k** (achieving 7.9%), having the TPA substituents bearing methoxy group in para position. The HTM **2c**, having a simple TPA substituent showed a slightly lower PCE (6.8%). Even for the case of a low-lying

valence band perovskite the presence of methoxy groups on the TPA moiety afford better PCE, probably due to the stabilizing effect of the methoxy groups on the transient radicals forming during the hole transfer process. Quite surprising, **2d** showed a markedly lower PCE (4.9%). While the further bond through the two phenyl units in carbazole should promote a higher planarity and a better conjugation, this structural feature seems not to help the device to gain better performance. The reason of this behavior is unknown, at this moment.

However, **2c** showed the highest V_{oc} in the series, while it did not show the highest short circuit current. Since a high V_{oc} was one of the most important requirements for purpose of the project, **2c** was the best compound in series **2** to be promoted for large scale PSCs tests.

Table 7. Optoelectronic properties of the **2c**, **2d**, **2k** and Spiro HTMs and their performances.

HTM	FF	V_{oc} (V)	J_{sc} (mA cm^{-2})	PCE (%)
2c	0.63	1.63	6.5	6.8
2d	0.37	1.48	8.6	4.9
2k	0.62	1.49	8.1	7.9
Spiro ¹⁸⁷	0.72	1.62	5.8	9.9

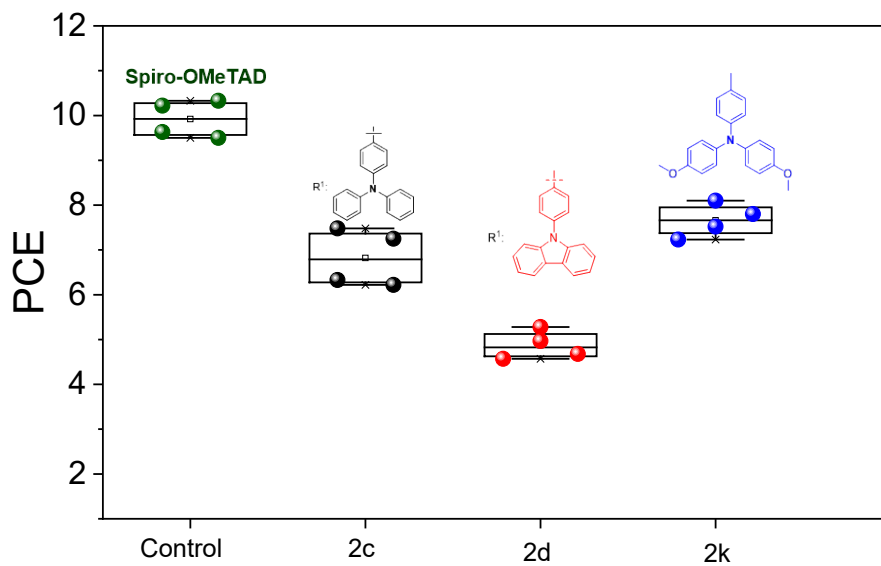


Figure 55. PCE of the Spiro-OMeTAD, 2c, 2d and 2k HTMs.

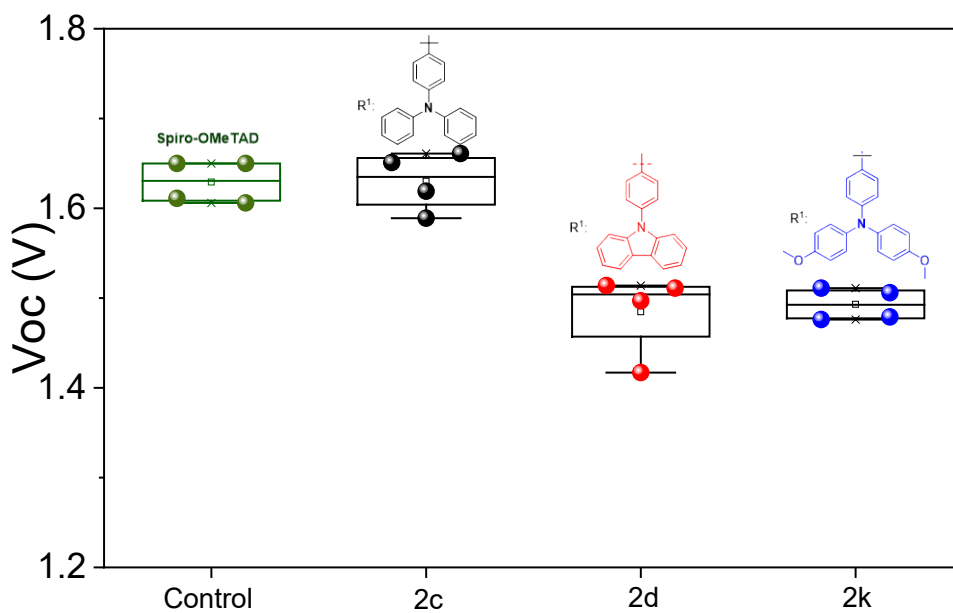


Figure 56. V_{oc} of the Spiro-OMeTAD, 2c, 2d and 2k HTMs.

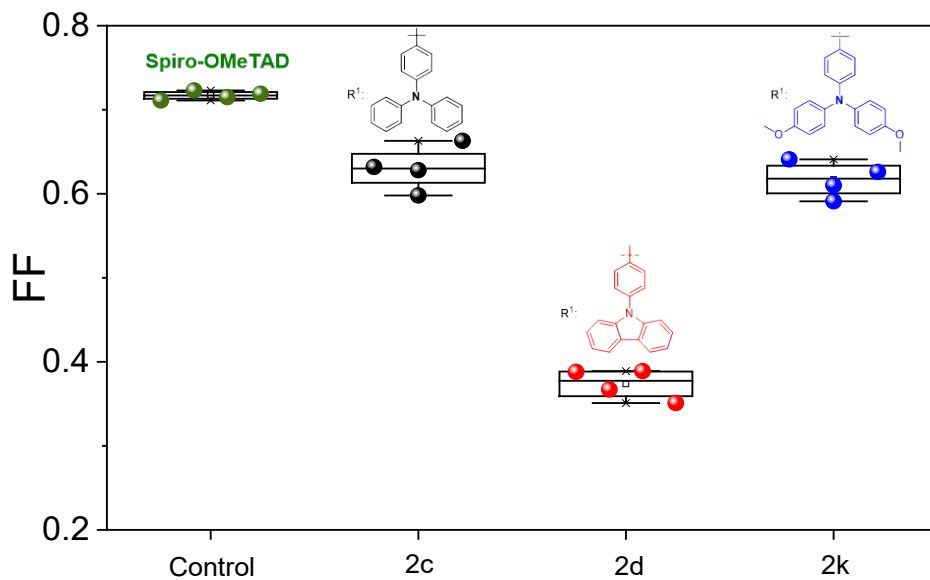


Figure 57. FF of the Spiro-OMeTAD, 2c, 2d and 2k HTMs.

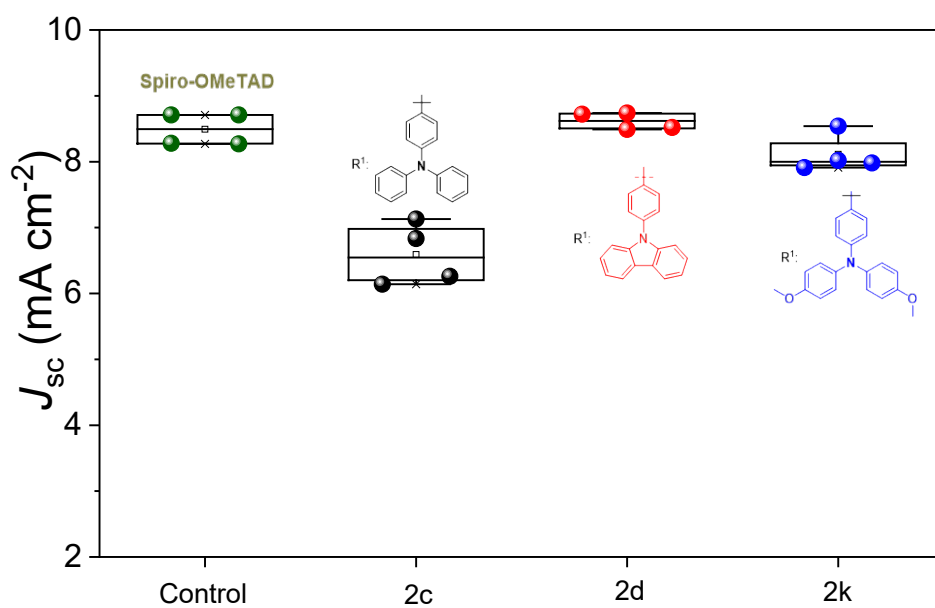


Figure 58. J_{sc} of the Spiro-OMeTAD, 2c, 2d and 2k HTMs.

6.5 Effect of the modification of the phenothiazine core on the properties and performances of HTMs

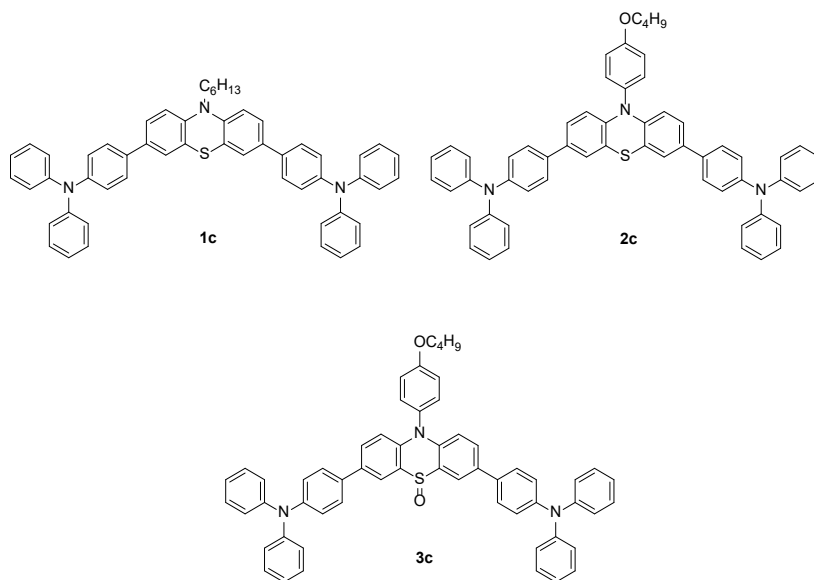


Figure 59. Structures of the **1c**, **2c** and **3c** HTMs.

6.5.1 Absorption and emission through UV-Vis and Fluorescence spectroscopy

The structures of **1c**, **2c**, and **3c** are reported in Figure 59. Normalized UV-Vis absorption and emission spectra of **1c**, **2c**, and **3c** are shown in Figure 60, and all optical data are reported in Table 8. It is worth noting that the three absorption profiles of **1c** and **2c** are slightly different but of **3c** is quite different comparing to **1c** and **2c**. The absorption maximum peaks for **1c**, **2c**, and **3c** HTMs in DCM at 319 nm, 323 nm, and 365 nm respectively are assigned to π - π^* transition of the aromatic rings of triphenylamine. The emission peaks are at 475 nm, 468 nm, and 423 nm,

respectively, for **1c**, **2c** and **3c**. However, according to Figure 60 the maximum absorption peak of **3c** is red shifted while the onset absorption is blue shifted due to oxidation of sulfur heteroatom of the phenothiazine core. As a result, it appears that the oxidation of sulfur is very useful to obtain higher transparency of phenothiazine based HTMs. Stokes shifts of the new HTMs are 156 nm for **1c**, 128 nm for **2c**, and 58 nm for **3c** it is obvious that from **1c** to **2c** we have a slight decrease of 25 nm in the Stokes shift but from **1c** to **3c** it appears that we have a huge reduction of the Stokes shift of 98 nm, this could lead to a better pore filling for ability **1c** and **2c** than **3c** possibly leading to higher hole mobility.¹⁸⁶ It appears that all the new HTMs do not absorb in the visible region.

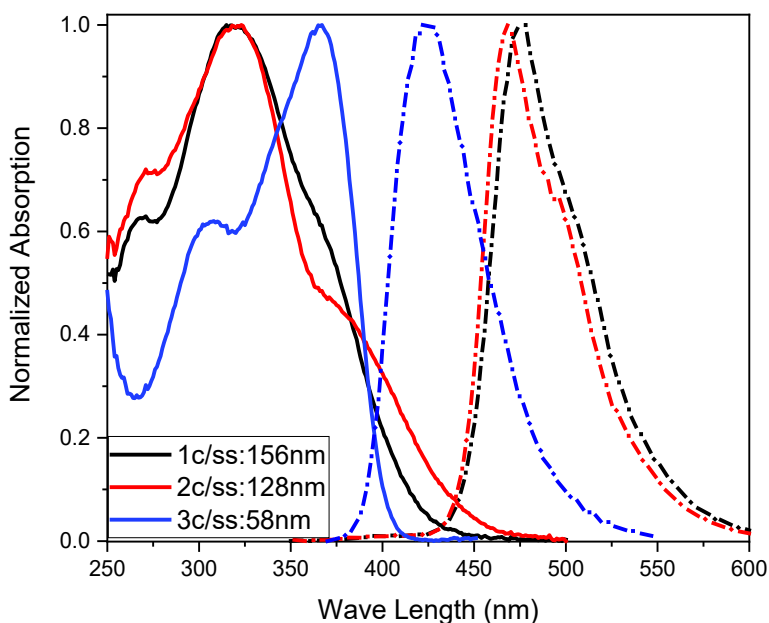


Figure 60. UV-Vis and Fluorescence of the **1c**, **2c** and **3c** HTMs.

6.5.2 Electrochemical characterization through cyclic voltammetry

The oxidation potential of the HTMs should be tuned with respect to the energy levels of the perovskite to obtain a high open-circuit voltage (V_{oc}) of the solar cell device and to ensure an efficient hole mobility kinetic. The highest occupied molecular orbitals (HOMOs) energy levels of the new PTZ based HTMs **1c**, **2c**, and **3c** were measured using cyclic voltammograms (CVs), which are indicated in Figure 61. According to electrochemical data, the HOMO energy levels of the new HTMs have been estimated as -5.28 eV for **1c**, -5.34 eV for **2c**, and -5.61 eV for **3c** in solution, whereas the HOMO energy level value of the spiro-OMeTAD is -5.20 eV. This lower HOMO of **3c** could be important to obtain higher V_{oc} in PSCs devices and, possibly, with specifically deep CB perovskites, but the relatively higher HOMO of **1c** and **2c** could lead toward faster hole transfer between the HTM and the perovskite.¹⁸⁹

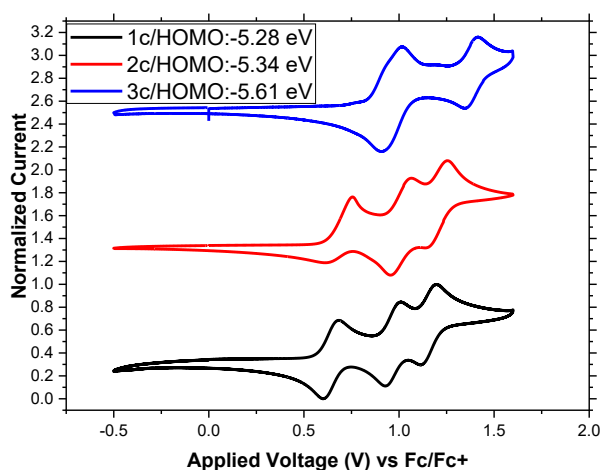


Figure 61. Cyclic Voltammograms of the **1c**, **2c** and **3c** HTMs.

6.5.3 Thermal Stability through TGA and DSC

The glass transition temperature (T_g) is one of the most important factors for the assessment of the stability of PSCs. One of the causes of the rapid degradation of PSCs performances is the transformation of a metastable amorphous state of the hole transporting material during the operative conditions to which the solar cell should normally survive.¹⁹⁰ The obtained results of T_g , T_m , and T_{stab} are summarized in Table 1 and Table 2. From Figure 64, during the 1st heating cycle, **1c** exhibited a glass transition accompanied by enthalpic relaxation and followed by an exothermal crystallization before the endothermic melting point. This confirms its amorphous character. In the case of **2c**, in the first heating cycle only the endothermic melting point was obtained, thus confirming its crystallinity due to the replacement of the hexyl-chain with the butoxyphenyl group. This indicates that the substitution pattern of the nitrogen of the phenothiazine is important: the N substitution with an aliphatic chain (hexyl) is giving an amorphous HTM, while the substitution with an aromatic butoxyphenyl group gives a more crystalline HTM. It was already reported that the crystallinity of the phenothiazine derivatives dramatically increases the hole mobility of HTMs.¹²³ As far as the **3c** HTM is concerned, in the 1st heating cycle a glass transition temperature T_g was noticed, accompanied by an enthalpic relaxation and followed by the endothermal melting point. This confirms its semicrystalline character. These data indicates that the oxidation of the sulfur atom of the

phenothiazine based HTM **2c** to sulfoxide (giving the sulfur monoxide **3c**) is affecting the crystallinity nature of HTM, transforming it from a crystalline to a semicrystalline HTM. During the 2nd heating cycle (Figure 63), the glass transition temperature T_g was found at 88 °C, 115 °C, and 129 °C for **1c**, **2c**, and **3c** respectively. It was found that **2c** is giving a higher value as expected due to its crystalline nature but **3c** which seems to be semicrystalline gave a higher value, even higher than Spiro-OMeTAD which T_g was found at 122 °C. On the basis of these results, it can be concluded that **2c** has a glass transition temperature slightly lower than Spiro-OMeTAD, while **3c** has a higher glass temperature indicating that it is more stable in the amorphous state than the Spiro-OMeTAD making both **2c** and **3c** particularly interesting for photovoltaics applications.^{191,192} Figure 62 shows the thermogravimetric analysis (TGA) of **1c**, **2c**, and **3c**, whose thermal stabilities were found at 373 °C, 413 °C, and 378 °C respectively. Therefore, the introduction of an aromatic unit (such as the butoxyphenyl moiety) instead of an aliphatic unit at the phenothiazine nitrogen is beneficial to the thermal stability of the HTMs, while oxidation of the sulfur atom is not beneficial for the thermal stability but it makes it more stable in the amorphous state.

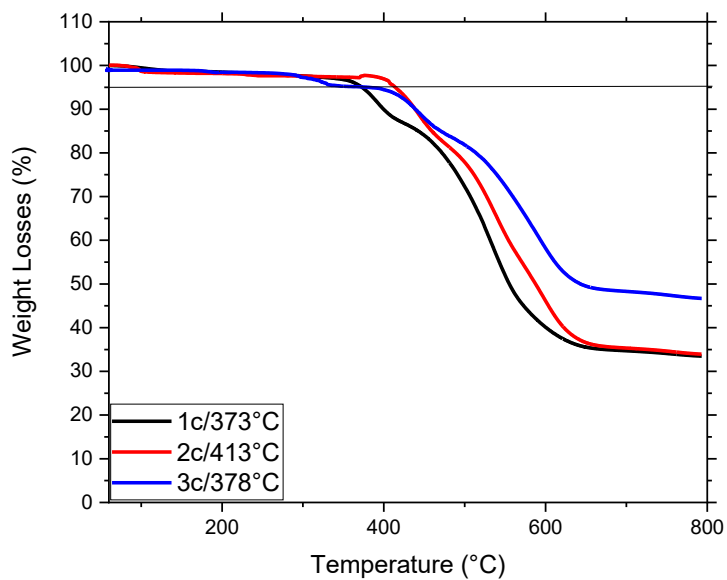


Figure 62. TGA graphs of the **1c**, **2c** and **3c** HTMs.

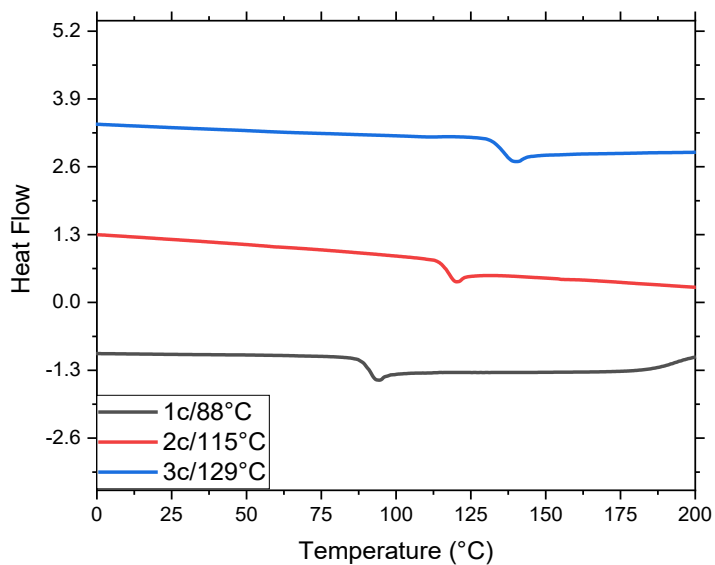


Figure 63. DSC graphs of **1c**, **2c** and **3c** HTMs.

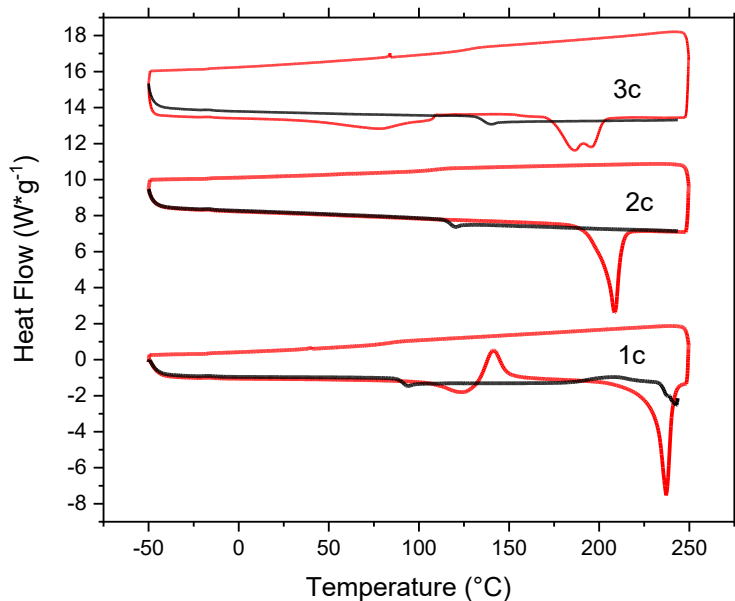


Figure 64. DSC of the **1c**, **2c** and **3c** HTMs, the down red color line is the first heating cycle and the upper red color line is the first cooling cycle, while the black line is second heating cycle.

Table 8. Optoelectronic properties of the **1c**, **2c**, **3c** and **Spiro-OMeTAD** HTMs.

HTM	λ_{abs} (nm)	λ_{onset} (nm)	λ_{em} (nm)	SS (nm)	HOMO (eV)	B_g (eV)	$T_{\text{Stab.}}$ (°C)	T_g (°C)	T_m (°C)
1c	319	424	475	156	-5.28	2.87	373	88	224
2c	323	460	467	144	-5.34	2.81	413	115	188
3c	365	405	423	58	-5.61	3.13	378	129	171
Spiro¹⁸⁷	386	426	419	33	-5.22	2.7	409	103	248

Table 9. Photovoltaic performances of the **2c** and **Spiro-OMeTAD** HTMs.

HTM	FF	V_{oc} (V)	J_{sc} (mA cm ⁻²)	PCE (%)
2c	0.63	1.63	6.5	6.8
Spiro¹⁸⁷	0.72	1.62	5.8	9.9

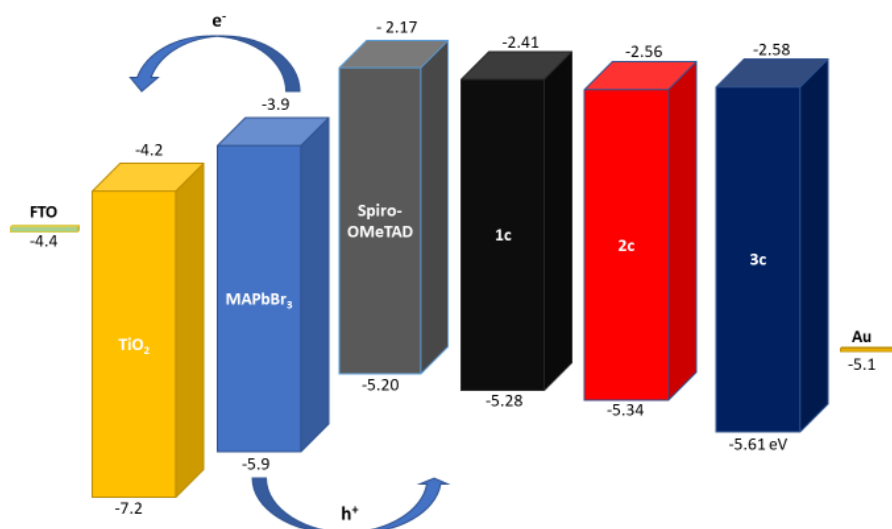


Figure 65. Frontier Molecular Energy Levels of the **1c**, **2c** and **3c** HTMs compared to **Spiro-OMeTAD** and the other PSCs components.

7 SYNTHESIS AND CHARACTERIZATION OF PHENOTHIAZINE POLYMERIC BASED HTMS: RESULTS AND DISCUSSION

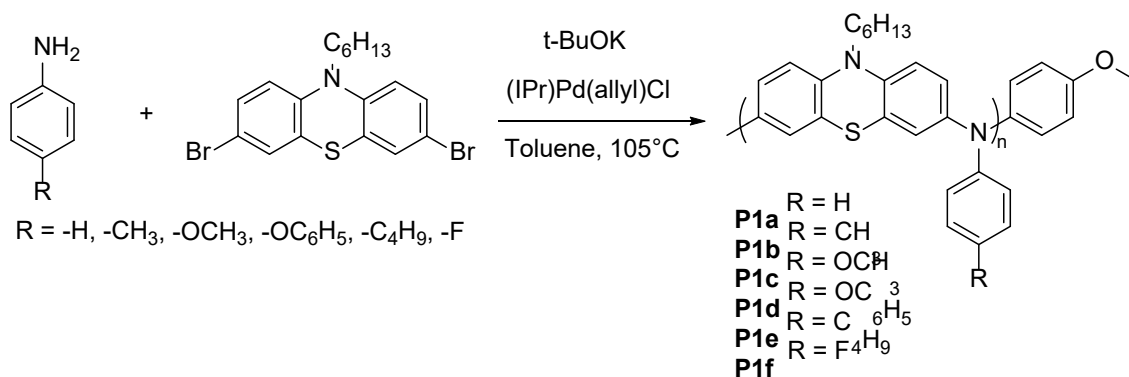
7.1 An overview

A common building block in the HTMs, based on small molecules or polymers, is the triphenylamine unit,^{117,193–196} which is an electron-rich moiety that can build materials with high hole mobility. Polymer based HTMs have been shown, with either the triphenylamine inserted in the polymer backbone^{195,197} or as pendant unit.¹⁹⁸ These polymeric HTMs usually require a long multistep synthesis with long and time expensive purification procedures for the monomers, resulting expensive materials with low overall yield.

7.2 Synthesis

In this work we were inspired by the previous materials using phenothiazine as a scaffold unit and choosing the scaffold **1** (see previous chapters) for its facile synthesis and cost-effective preparation. We synthesize a novel family of polymers via one-pot Buchwald-Hartwig coupling reaction. Buchwald-Hartwig amination gives nitrogen-carbon bond when an aryl halide is reacted with a primary or secondary amine in the presence of a palladium catalyst and base. The reaction between 3,7-

dibromo-10-hexyl-10H-phenothiazine (Scaffold **1**) with selected commercially available low-cost aniline derivatives feature a facile work up, leading to reduction of time-consuming purification steps. The reaction was carried out in 24 hours and to minimize the reaction steps 0.01 equivalent of 4-bromoanisole were added to terminate end amino groups. It has been reported that the degradation of HTM molecules caused by radical at the 4-position of a pendant group of the amine.¹⁹⁹ To avoid the possibility of degradation, beside aniline amines with different functional groups at the position 4 were used. The functional groups were selected to study the effect of electron withdrawing and electron donating units at the 4-position on the characterization and functionality of the final polymer. The yield of the polymers **P1a**, **P1b**, **P1c**, **P1d**, **P1e**, **P1f** were 22%, 55%, 49%, 44%, 56%, and 35%, respectively.



Scheme 23. Synthetic route for the polymeric HTMs through Buchwald coupling.

7.3 Characterization

7.3.1 Molecular weight measurement by SEC

The weight average molecular weight (M_w) value for all polymers is in the range from 5-8 kDa (Table 9). Due to that, polymers can improve the stability of the device by protecting the perovskite active layer from degradation. The obtained polymers have a reasonably low polydispersity from 1.2 to 1.6, which indicates their homogeneity.

The presence of an electron withdrawing group (-F, **P1f**) on the aniline unit at the para position led to a decrease in the molecular weight of the polymer while the presence of electron donating groups increased the molecular weight of the polymer.

7.3.2 Absorption and emission through UV-Vis and Fluorescence spectroscopy

The polymeric HMTs (**P1a-f**) were characterized by UV-Vis and Fluorescence spectroscopies (Figure 66, Figure 67, and Table 10). All the UV-Vis spectra of the polymers are similar and have a maximum absorption peak in between 263 and 269 nm, followed by a shoulder peak at around 340 nm. The introduction of an electron donating group at the para position of the aniline unit led to a small red shift of the absorption maximum, as found for the small molecule **2k**. This agrees with the

conjugation breaking attitude of the triarylamine, through its nitrogen. The polymers behave similarly for the emission spectroscopy, showing emission peaks in the range 480-484 nm.

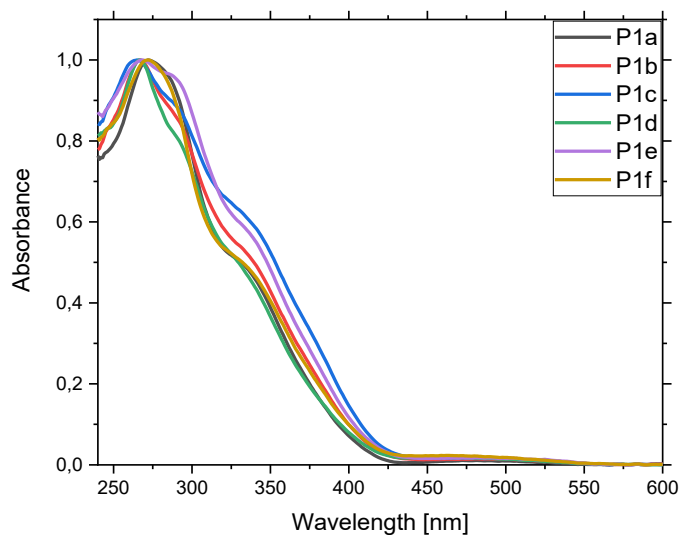


Figure 66. UV-Vis Spectra of polymeric HTMs.

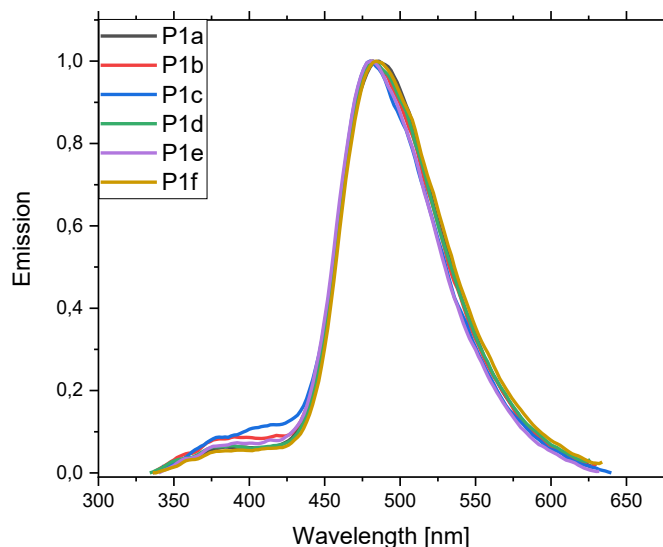


Figure 67. Fluorescence Spectra of polymeric HTMs.

7.3.3 Thermal Stability through TGA and DSC

The polymers (**P1a-1f**) demonstrated good thermal stability (Table 10 and Figure 68).

The general structure of the polymer is the same and therefore it is reasonable to obtain similar values since this should be mainly related to the stability of the polymeric backbone. The variation in the thermal stability is minimal and can be related to the substituent on the para position of the aniline moiety. The values obtained for the polymers show that the unsubstituted polymer (**P1a**, R = H) and the polymers substituted with alkyl groups and electron acceptors (**P1b**, R = CH₃ and **P1e**, R = C₄H₉, **P1f**, R = F) show the higher stability temperatures (between 372 and 380 °C), while the polymers substituted with strong electron donor groups (**P1c**, R = OCH₃ and **P1d**, R = OC₆H₅) are somewhat less stable (362-367 °C) probably connected to

the presence of the ether group. However, the overall stability is still very good. These values showed that the polymers can be processable for the preparation of perovskite solar cells.

From the DSC plots the glass transition, reported in (Table 10 and Figure 69), was obtained for all polymers. The presence of a glass transition in one of the most studied molecular HTMs, Spiro-OMeTAD ($T_g = 126\text{ }^\circ\text{C}$), is considered an essential point in favoring the good performance of the cell, as it ensures that an amorphous structure can be maintained. The HTM is stable in the film until glass transition is reached. Furthermore, stiffness is a symptom of strong packing while remaining in an amorphous state, where the polymer chains are in close contact with each other, favoring in principle the transfer of charge and therefore the transport of the holes, in the case of p-type polymers. The glass transition (T_g), for **P1a** is observable at $111.97\text{ }^\circ\text{C}$ and for **P1b** at $117.91\text{ }^\circ\text{C}$. This demonstrates a significant difference in stiffness between the two polymers, due to the presence of the methyl group in the para position of the pendant phenyl group ($R = \text{H}$ for **P1a** and $R = \text{CH}_3$ for **P1b**). In the case of polymer **P1e** ($R = \text{C}_4\text{H}_9$) the glass transition is less evident, and lower ($99.80\text{ }^\circ\text{C}$) probably due to the steric hindrance of the butyl chain, which strongly reduces the polymer packing. The polymer **P1c** has a high T_g ($133.29\text{ }^\circ\text{C}$). Packing and stiffness are particularly high, most likely because of the presence of oxygen which can provide interactions with portions of the polymer chain in which a partial positive

charge is present. This effect is less marked in the case of the **P1d** polymer, in which probably the size of the benzene ring of the phenoxy group ($R = OC_6H_5$) distances the polymer chains from each other. In conclusion, the materials can maintain their solid phase structure at least up to 99 °C and up to about 109 °C, if polymer P1e ($R = C_4H_9$) is excluded.

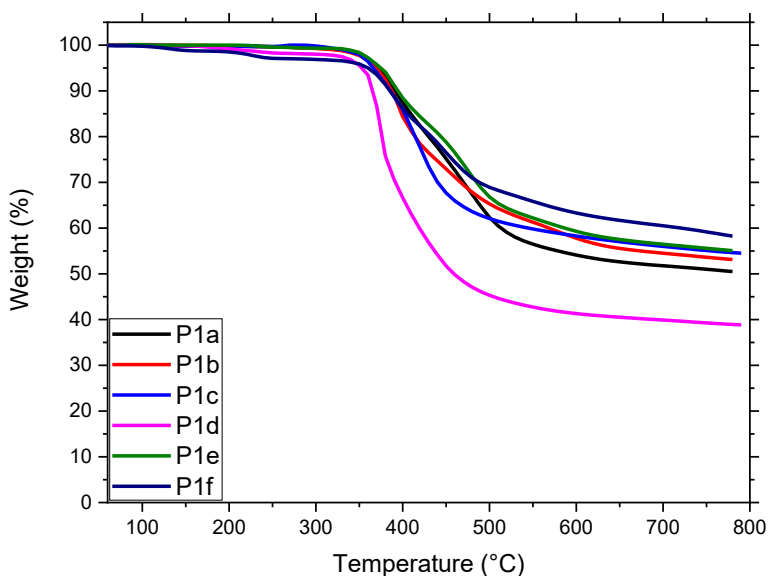


Figure 68. TGA curves of the Polymeric HTMs.

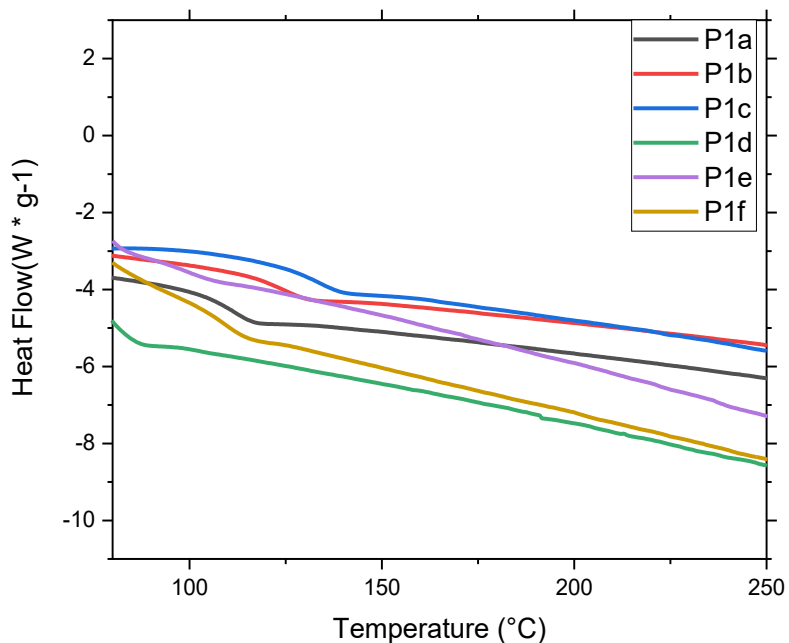


Figure 69. DSC curves of the second heating cycle of the polymeric HTMs.

7.3.4 Electrochemical characterization through cyclic voltammetry

The HTM substituted with Fluorine atom at the para position of the aniline unit, **P1f**, showed the deepest HOMO energy, as expected from the acceptor nature of the fluorine substituent. As expected, the most effective donor substituent, OCH₃ (**P1c**), showed the highest HOMO level, but this is still very close to the others. In fact, the HOMO values, as seen also by the E_{1/2} potentials (Figure 70), do not vary much between them. This is mainly due to the localization of HOMO around the phenothiazine core since the breaking of conjugation imposed by the triarylamine nature of these polymers. Therefore, the effect of the substituent of the benzene

ring of the aniline unit only marginally affects the energy value of HOMO. It should be emphasized that, although the differences between the values can be considered within the experimental error, a relationship between the energy value of the HOMO of the polymer and the inductive characteristics of the substituent can be outlined. In any case, given the proximity of the energy levels of the polymers, it is likely that important differences in the photovoltaic behavior of the polymers are dependent on the morphological state of the polymer film deposited on the perovskite, for which the glass transition temperature of the polymer can be an important indication.

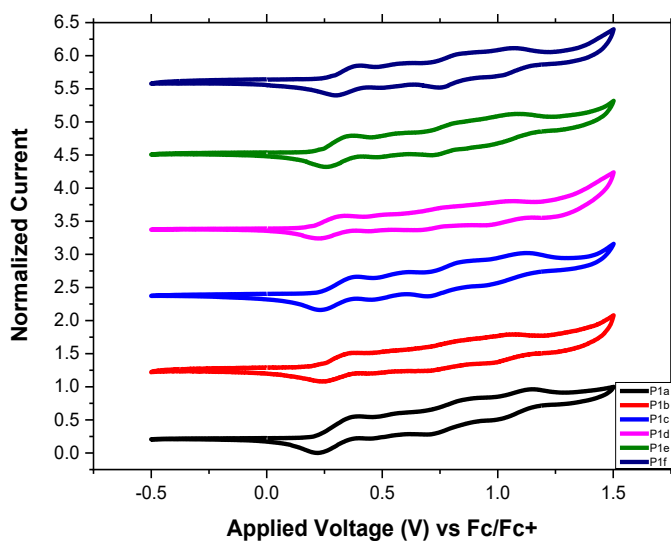


Figure 70. Cyclic Voltammograms of the polymeric HTMs.

Table 9. Optical, electrochemical and thermal characterization of the polymeric HTMs.

HTM	λ_{\max} (nm)	λ_{onset} (nm)	λ_{em} (nm)	HOMO (eV)	B_g (eV)	T_{stab} (°C)	T_g (°C)
P1a	269	418	480	-4.98	2.97	372	111.97
P1b	266	430	480	-4.94	2.88	373	117.91
P1c	263	408	480	-4.91	3.04	366	133.29
P1d	266	415	480	-4.95	2.99	362	119.61
P1e	263	402	480	-4.94	3.08	380	99.8
P1f	269	422	485	-5.00	2.94	376	109.34

8 EXPERIMENTAL

8.1 Materials and instruments:

8.1.1 Materials

All chemicals and solvents were purchased as pure grade for synthesis or spectroscopy from Merck, TCI Chemicals, abcr and VWR, and used without further purification.

8.1.2 Instruments

8.1.2.1 NMR Spectra:

NMR spectra were recorded a JEOL ECZ-R 600, working at 600 MHz and 151 MHz for ^1H -NMR and ^{13}C , respectively.

8.1.2.2 Mass Spectra:

ESI-MS experiments were performed with a Thermo Fisher Scientific LCQ Advantage Max ion-trap mass spectrometer, equipped with an ESI source.

8.1.2.3 UV-Vis spectra:

The UV-Vis spectra were recorded in dichloromethane (DCM) with an Agilent Technologies Cary60 UV-Vis spectrometer.

8.1.2.4 Fluorescence spectra:

Fluorescence spectra were acquired in dichloromethane (DCM) with a Cary Eclipse Fluorescence spectrophotofluorometer.

8.1.2.5 SEC – Molecular weight measurement

SEC–Molecular weight measurements were performed with Waters SEC chromatographic system equipped with a refractometer detector, using a guard column and three columns in series (Styragel HR2,HR4 and HR6). The analyses were performed at 35°C and THF was used as the mobile phase at a 1 ml min⁻¹ flow rate. A calibration curve was prepared with a series of polystyrenes of different molecular weight (575-3848000 g mol⁻¹).

8.1.2.6 Cyclic Voltammetry Measurement

Cyclic voltammetry analyses were performed with SP-300 BIOLOGIC potentiostat using DCM as solvent and tetrabutylammonium hexafluorophosphate (TBAP) as support electrolyte. Scan rate was set to 50 mV/s and the scan was performed from -1.2 to 1.5 V using Ag/AgCl as reference electrode and Ferrocene (Fc/Fc+) as internal reference.

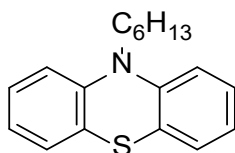
8.1.2.7 Thermal Analysis:

Thermogravimetric analyses (TGA) were performed with a TGA TAQ 600 (TA Instruments) in nitrogen atmosphere with a heating gradient of 30°C/min from 30°C to 800°C.

Calorimetric analyses (DSC) were performed with a DSC TAQ 200 (TA Instruments) in nitrogen atmosphere with a heating gradient of 30°C/min from -50 °C to 250°C.

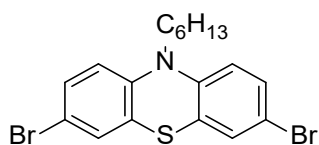
8.2 Synthesis

8.2.1 10-hexyl-10H-phenothiazine (**1a**)



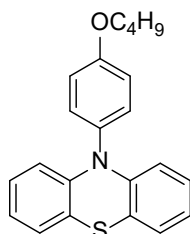
Phenothiazine (5 g, 25.1 mmol, 1 eq) was dissolved in dry DMF (10 mL) under argon atmosphere, then it was cooled to 0 °C and after that NaH (903 mg, 32.62 mmol, 1.5 eq) was added portion wise to the mixture and kept stirring for 1 hour. 1-Iodohexane (18 g, 38 mmol, 1.7 eq) was added to the mixture and kept stirring at RT until consumption of phenothiazine, monitoring by TLC using an eluent of 10% EtOAc in PE (petroleum ether). The reaction was quenched by ice cold water and extracted by EtOAc and brine. After drying with Na₂SO₄ the organic phase was evaporated under vacuum. The crude was purified by a short silica column using hexanes eluent giving a yellow oil (6.319 g, 88%). ¹H NMR (600 MHz, DMSO-d₆) δ 7.16 – 7.11 (m, 2H), 7.08 (dd, J = 7.6, 1.5 Hz, 2H), 3.77 (t, J = 7.0 Hz, 2H), 1.63 – 1.55 (m, 2H), 1.34 – 1.24 (m, 2H), 1.15 (td, J = 6.6, 3.3 Hz, 4H), 0.82 – 0.71 (m, 3H). ¹³C NMR (151 MHz, DMSO-d₆) δ 145.35, 128.10, 127.64, 124.17, 122.93, 116.35, 46.93, 31.36, 26.73, 26.36, 22.59, 14.36.

8.2.2 3,7-dibromo-10-hexyl-10H-phenothiazine (**11**)



10-hexyl-10H-phenothiazine (2 g, 7.1 mmol, 1 eq) was dissolved in dichloromethane (DCM) (20 mL), then bromine (5.6 g, 35.3 mmol, 5 eq) was dissolved in DCM (10 mL) and added dropwise, the mixture was stirred at room temperature until consumption of the starting material. Then, the mixture was cooled to -5 °C and sodium bisulfite was added slowly until the color changed from purple to white then NaOH solution was added, and the crude mixture was extracted twice with DCM. The organic layer was dried over Na₂SO₄, and the solvent was evaporated under vacuum giving as yellow oil which turned onto a greenish solid (2.9 g, 93%). ¹H NMR (600 MHz, DMSO-D₆) δ 7.33 – 7.27 (m, 4H), 6.89 (d, J = 8.6, 0.7 Hz, 2H), 3.75 (t, J = 7.0 Hz, 2H), 1.57 (q, J = 7.5, 6.1 Hz, 2H), 1.33 – 1.25 (m, 2H), 1.22 – 1.13 (m, 4H), 0.79 – 0.72 (m, 3H). ¹³C NMR (151 MHz, DMSO-D₆) δ 144.35, 130.89, 129.60, 126.01, 118.17, 114.54, 47.17, 31.30, 26.45, 26.23, 22.58, 14.35. MS/ESI⁺: 440.89 a.m.u.

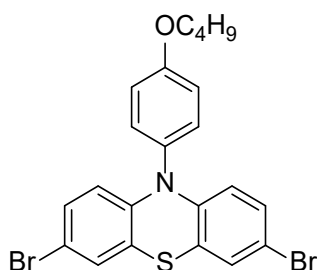
8.2.3 10-(4-butoxyphenyl)-10H-phenothiazine (**2a**)



The reaction was performed in a 20 ml MW vial dried in an oven overnight, closed with a crimp and purged with argon. Phenothiazine (5 g, 25.1 mmol, 1 eq), 1-bromo-4-n-butoxy-benzene (7.5 g, 32.6 mmol, 1.3 eq), $\text{Pd}_2(\text{dba})_3$ [tris(dibenzylideneacetone)dipalladium(0)] (460 mg, 0.5 mmol, 0.02 eq), sodium t-butoxide (3.7 g, 38.4 mmol, 1.5 eq) and tri-t-butylphosphine (102 mg, 0.5 mmol, 0.02 eq) were dissolved in o-xylene (10 mL) and stirred under argon at 80 °C for 12h. After completion of the reaction, the mixture was cooled down to room temperature and quenched with water. The mixture was extracted three times using dichloromethane and water. The organic layer was separated and dried with anhydrous sodium sulfate, and then the solvent was removed using a rotary evaporator. The crude product was precipitated from MeOH giving white crystals (6.5 g, 75%). ^1H NMR (600 MHz, Acetone- d_6) δ 7.33 – 7.27 (m, 2H), 7.21 – 7.15 (m, 2H), 7.01 – 6.95 (m, 2H), 6.87 (m, $J = 8.3, 7.3, 1.6$ Hz, 2H), 6.79 (m, 2H), 6.19 (dd, $J = 8.2, 1.3$ Hz, 2H), 4.08 (t, $J = 6.4$ Hz, 2H), 1.83 – 1.75 (m, 2H), 1.57 – 1.47 (m, 2H), 0.97 (t, $J = 7.4$ Hz, 3H). ^{13}C NMR (151

MHz, Acetone-d₆) δ 159.19, 144.74, 133.00, 132.20, 127.08, 126.50, 122.43, 119.55, 116.51, 115.82, 67.81, 31.27, 19.12, 13.32. MS/ESI⁺: 347.08 a.m.u.

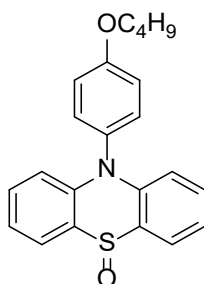
8.2.4 3,7-dibromo-10-(4-butoxyphenyl)-10H-phenothiazine (**21**)



10-(4-butoxyphenyl)-10H-phenothiazine (2.5 g, 7.2 mmol, 1 eq) was dissolved in CHCl₃ (150 mL) and the temperature was maintained at 0 °C. Then Br₂ (2.3 g, 14.4 mmol, 2 eq) was dissolved in 50 mL of CHCl₃ and was dropped into the flask very slowly while keeping the temperature at around 0 °C. The reaction mixture was stirred until consumption of all starting material. Then, the mixture was cooled to -5 °C and sodium bisulfite was added slowly until the color changed from purple to white then NaOH solution was added and the crude mixture was extracted using DCM twice, the organic layer was dried over Na₂SO₄ and the solvent was dried under vacuum giving a crude product which was purified by redissolving in minimum dichloromethane and precipitating it from MeOH, giving a white powder (3.15 g, 86.7%). ¹H NMR (600 MHz, CDCl₃) δ 7.23 – 7.18 (m, 2H), 7.11 – 7.04 (m, 4H), 6.89 (dd, J = 8.7, 2.4 Hz, 2H), 6.00 (d, J = 8.8 Hz, 2H), 4.02 (t, J = 6.4 Hz, 2H), 1.85 – 1.78

(m, 2H), 1.58 – 1.48 (m, 2H), 1.00 (t, J = 7.4 Hz, 3H). ¹³C NMR (151 MHz, CDCl₃) δ 159.27, 143.60, 132.28, 131.84, 129.77, 128.79, 121.08, 117.01, 116.73, 114.59, 68.13, 31.38, 19.37, 13.96.

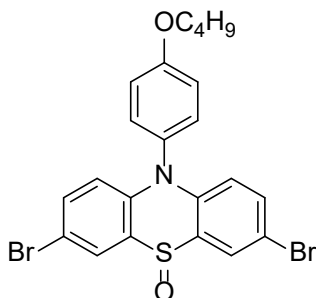
8.2.5 10-(4-butoxyphenyl)-10H-phenothiazine 5-oxide (**3a**)



To a solution of 10-(4-methoxyphenyl)-10H-phenothiazine (500 mg, 1.64 mmol, 1 eq) in 10 mL of DCM, a solution of 3-chloroperbenzoic acid (366.92 mg, 1.64 mmol, 1 eq, 77%) in 20 mL of DCM was added dropwise over 30 min at 0 °C. The reaction was completed with 2 h. The reaction mixture was washed with saturated Na₂CO₃ aqueous solution, and then the reaction mixture was extracted with DCM (3 x 20 mL) and the combined organic layers were dried with Na₂SO₄ and completely removed by rotary evaporation. The residue was purified with column chromatography using 80% EtOAc in PE as eluent (467 mg, 89%). ¹H NMR (600 MHz, CDCl₃) δ 7.98 (dd, J = 7.8, 1.7 Hz, 2H), 7.42 – 7.37 (m, 2H), 7.31 – 7.28 (m, 2H), 7.22 (t, J = 1.6 Hz, 2H), 7.18 – 7.13 (m, 2H), 6.77 (d, J = 1.1 Hz, 2H), 4.07 (t, J = 6.5 Hz, 2H), 1.90 – 1.80 (m, 2H), 1.65 – 1.49 (m, 2H), 1.02 (t, J = 7.4 Hz, 3H). ¹³C NMR (151 MHz, CDCl₃) δ 159.76,

139.50, 132.85, 131.95, 131.41 (d, J = 5.3 Hz), 122.14, 117.59, 116.82, 68.22, 31.37, 19.38, 13.98. MS/ESI⁺: 363.98 a.m.u.

8.2.6 3,7-dibromo-10-(4-butoxyphenyl)-10H-phenothiazine 5-oxide (**3I**)

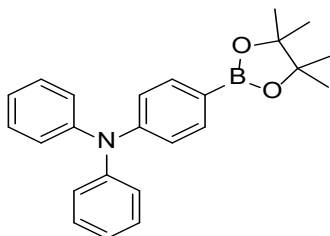


To a solution of 3,7-dibromo-10-(4-butoxyphenyl)-10H-phenothiazine (3 g , 5.94 mmol, 1 eq) in 60 mL of DCM, a solution of 3-chloroperbenzoic acid (1.33 g, 5.94 mmol, 1 eq) in 120 mL of DCM was added dropwise over 30 min at 0 °C. The reaction was completed within 2 h. The reaction mixture was washed with saturated aq. of Na₂CO₃, and then the reaction mixture was extracted with DCM (3 x 50 mL) and the combined organic layers were dried with Na₂SO₄ and completely removed by rotary evaporation. The residue was purified by column chromatography using % 80EtOAc in PE giving 2.9 g of a white solid, 94%. ¹H NMR (600 MHz, CDCl₃) δ 8.07 (d, J = 2.3 Hz, 2H), 7.46 (dd, J = 9.2, 2.3 Hz, 2H), 7.24 (dd, J = 9.0, 2.5 Hz, 3H), 7.15 (d, J = 8.7 Hz, 2H), 6.65 (d, J = 9.1 Hz, 2H), 4.06 (t, J = 6.4 Hz, 2H), 1.90 – 1.80 (m, 2H), 1.60 – 1.50 (m, 2H), 1.02 (t, J = 7.4 Hz, 3H). ¹³C NMR (151 MHz, CDCl₃) δ 160.07, 138.04, 135.71,

133.88, 131.00, 130.70, 123.39, 119.51, 117.07, 114.26, 68.30, 31.32, 19.36, 13.96.

MS/ESI⁺: 521.81 a.m.u.

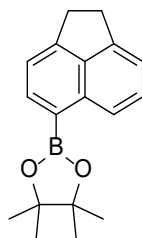
8.2.7 N,N-diphenyl-4-(4,4,5,5-tetramethyl-1,3,2-dioxaborolan-2-yl)aniline (**c**)



To N-(4-bromophenyl)diphenylamine (5 g, 15.42 mmol, 1 eq) in a 100 mL Schlenk flask, 90 mL of anhydrous THF was added and the solution was cooled to -78 °C. To this, 2.5 M n-butyllithium in hexane (9.25 mL, 23.13 mmol, 1.5 eq) was added slowly and stirred for 30 min. Then 2-isopropoxy-4,4,5,5-tetramethyl-1,3,2-dioxaborolane (4.88 g, 26.22 mmol, 1.7 eq) was added and slowly allowed to warm to room temperature. The reaction was stirred overnight and then quenched with brine. The product was then extracted with diethyl ether, washed with brine, dried over Na₂SO₄ and the solvent was removed under vacuum. The crude product was chromatographed on silica gel eluted with 0-10% ethyl acetate in hexane, giving a white solid 5.6 g (97%) of a yellow oily liquid. ¹H NMR (600 MHz, Acetone-d₆) δ 7.69 – 7.57 (m, 2H), 7.38 (tt, J = 7.6, 1.7 Hz, 4H), 7.21 – 7.13 (m, 6H), 7.10 – 6.89 (m, 2H),

1.38 (s, 12H). ^{13}C NMR (151 MHz, Acetone- d_6) δ 150.86, 147.44, 135.85, 129.73, 125.41, 124.04, 121.07, 117.49, 83.74, 25.22. MS/ESI $^+$: 372 a.m.u.

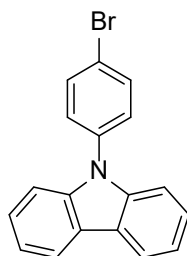
8.2.8 2-(1,2-dihydroacenaphthylen-5-yl)-4,4,5,5-tetramethyl-1,3,2-dioxaborolane (**b**)



This product was obtained by applying the same procedure for the compound (c).

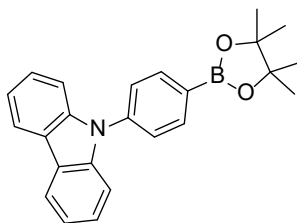
The crude product was chromatographed on silica gel, eluted with 0-10% ethyl acetate in hexane giving a 70% yield. ^1H NMR (600 MHz, Acetone- d_6) δ 8.33 (dt, J = 8.4, 0.8 Hz, 1H), 7.98 (d, J = 6.9 Hz, 1H), 7.44 (dd, J = 8.4, 6.8 Hz, 1H), 7.27 (tt, J = 6.7, 1.2 Hz, 2H), 3.34 (t, J = 0.9 Hz, 4H), 1.38 (s, 12H). ^{13}C NMR (151 MHz, Acetone- d_6) δ 150.35, 146.09, 138.85, 137.74, 135.63, 128.11, 123.70, 119.16, 118.80, 83.36, 30.08, 29.78, 24.48.

8.2.9 9-(4-bromophenyl)-9H-carbazole (**d-Br**)



A mixture of carbazole (1 g, 1eq), 1-bromo-4-iodobenzene (2.6 g, 1.5 eq), copper powder (762 mg, 2 eq), potassium carbonate (3.4 g, 4 eq), and anhydrous DMF (20mL) were added into a 50 ml round bottom flask. After stirring and degassing for 15 min, the reaction system was refluxed for 12h under Ar. The reaction mixture was cooled to room temperature. After adding deionized water, a brown solid was obtained by filtration and purified by silica gel column chromatography with hexane. 932 mg of 9-(4-bromophenyl)-9H-carbazole were obtained as white crystals, 48%. ^1H NMR (600 MHz, Acetone- d_6) δ 10.29 (s, 1H), 8.19 (dt, $J = 7.8, 1.0$ Hz, 1H), 8.08 (m, 1H), 7.88 – 7.82 (m, 1H), 7.62 – 7.54 (m, 1H), 7.48 (dt, $J = 8.1, 0.9$ Hz, 1H), 7.45 – 7.39 (m, 1H), 7.41 – 7.35 (m, 1H), 7.38 – 7.32 (m, 1H), 7.27 (m, 1H), 7.15 (m, 1H). ^{13}C NMR (151 MHz, Acetone- d_6) δ 140.63, 136.98, 133.29, 129.05, 126.28, 123.52, 120.53, 120.40, 120.35, 109.64.

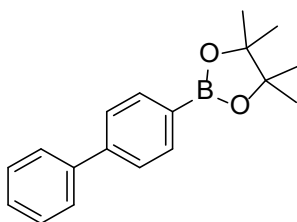
8.2.10 9-(4-(4,4,5,5-tetramethyl-1,3,2-dioxaborolan-2-yl)phenyl)-9H-carbazole (**d**)



This product was obtained by applying the same procedure for the compound (c).

The crude product was chromatographed on silica gel eluted with yield 0-10% ethyl acetate in hexane. Isolated yield 72% (380 mg). ^1H NMR (600 MHz, Acetone- d_6) δ : 8.20 (m, 2H), 8.05 – 8.02 (m, 2H), 7.65 – 7.62 (m, 2H), 7.47 – 7.39 (m, 4H), 7.27 (m, , 2H), 1.37 (s, 12H).

8.2.11 2-([1,1'-biphenyl]-4-yl)-4,4,5,5-tetramethyl-1,3,2-dioxaborolane (**e**)

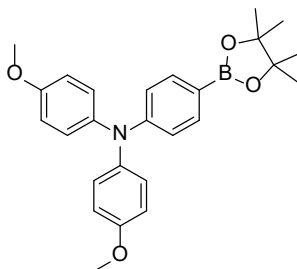


This product was obtained by applying the same procedure for the compound (c).

The crude product was chromatographed on silica gel eluted with 0-10% ethyl acetate in hexane giving 3.397 g, 94%. ^1H NMR (600 MHz, Acetone- d_6) δ 7.82 – 7.80 (m, 2H), 7.67 – 7.64 (m, 4H), 7.47 – 7.43 (m, 2H), 7.36 (m, 1H), 1.33 (s, 12H). ^{13}C NMR

(151 MHz, Acetone-d₆) δ 143.72, 140.76, 135.27, 128.97, 127.75, 127.00, 126.25, 83.74, 24.38.

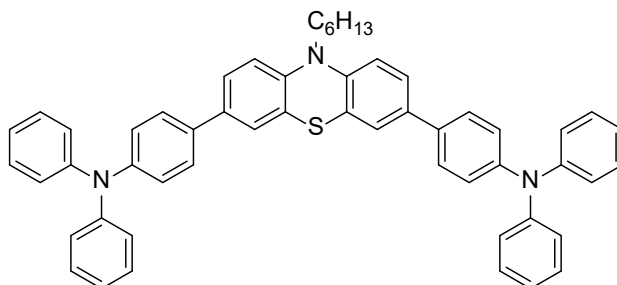
8.2.12 4-methoxy-N-(4-methoxyphenyl)-N-(4-(4,4,5,5-tetramethyl-1,3,2-dioxaborolan-2-yl)phenyl)aniline (**k**)



This product was obtained by applying the same procedure for the compound (c).

The crude product was chromatographed on silica gel eluted with 0-10% ethyl acetate in hexane giving 2.16 g, 76%. ¹H NMR (600 MHz, Acetone-d₆) δ 7.52 – 7.48 (m, 2H), 7.07 – 7.03 (m, 4H), 6.91 – 6.88 (m, 4H), 6.75 – 6.73 (m, 2H), 3.77 (d, J = 1.1 Hz, 6H), 1.27 (s, 12H). ¹³C NMR (151 MHz, Acetone-d₆) δ 156.82, 151.69, 140.18, 135.73, 127.51, 126.55, 120.45, 117.70, 114.88, 114.75, 83.20, 54.90, 24.35.

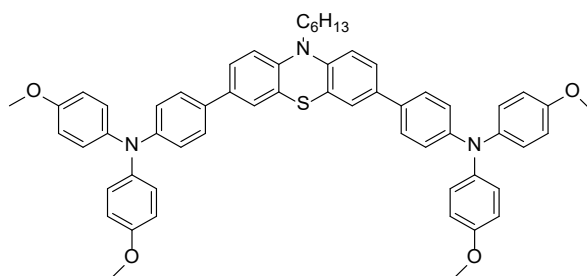
8.2.13 4,4'-(10-hexyl-10H-phenothiazine-3,7-diyl)bis(N,N-diphenylaniline) (**1c**)



The reaction was performed in a 25 ml round bottom flask connected with condenser and purged with argon. A mixture of 3,7-dibromo-10-hexyl-10H-phenothiazine (600 mg, 1.36 mmol, 1 eq), (4-(diphenylamino)phenyl)boronic acid (1.06 g, 3.67 mmol 2.7 eq) and Pd(PPh₃)₄ (79 mg, 0.68 mmol, 0.05 eq) and Aliquat 336 (0.110 mg, 0.272 mmol, 0.2 eq) in toluene (10 mL). To this solution, a mixture K₂CO₃ (1.18 g, 8.57 mmol, 6.3 eq) aqueous solution (4.3 mL) was added. Then the reaction was stirred overnight at 110 °C. After cooling down the reaction to room temperature, the mixture was diluted with dichloromethane and washed with water. The organic layer was dried over Na₂SO₄ and evaporated. The crude product was concentrated and passed through a short pad of silica, then the organic phase was concentrated under vacuum and precipitated from MeOH giving 988 mg as a yellow solid, 94%. ¹H NMR (600 MHz, THF-d₈) δ 7.46 – 7.42 (m, 4H), 7.37 – 7.33 (m, 4H), 7.22 – 7.18 (m, 8H), 7.06 – 7.03 (m, 12H), 6.96 (m, 6H), 3.95 – 3.89 (m, 2H), 1.84

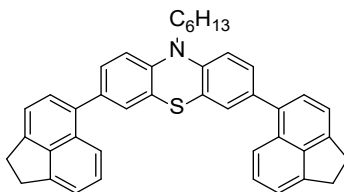
– 1.78 (m, 2H), 1.46 (q, $J = 7.2$ Hz, 2H), 1.35 – 1.29 (m, 4H), 0.86 (m, 3H). 7.1 Hz, 2H), 1.84 - 1.78 (m, 2H), 1.47 (q, $J = 8.3, 7.8$ Hz, 2H), 1.33 - 1.29 (m, 4H), 0.86 - 0.84 (m, 3H). ^{13}C NMR (151 MHz, THF- d_8) δ 147.89, 146.96, 144.02, 134.89, 134.29, 129.10, 126.93, 125.16, 124.90, 124.16, 124.05, 122.69, 115.48, 31.55, 26.85, 26.52, 22.59, 13.41. MS/ESI $^+$: 769.27 a.m.u.

8.2.14 4,4'-(10-hexyl-10H-phenothiazine-3,7-diyl)bis(N,N-bis(4-methoxyphenyl)aniline) (**1k**)



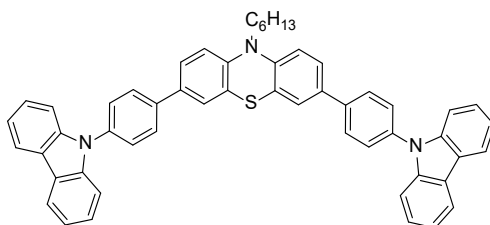
This compound was obtained by applying the same protocol as for the compound **1c**. Yield: 324 mg, 80%. ^1H NMR (600 MHz, THF- d_8) δ : 7.36 – 7.29 (m, 8H), 7.01 – 6.97 (m, 8H), 6.93 (dd, $J = 8.5, 1.3$ Hz, 2H), 6.90 – 6.87 (m, 4H), 6.82 – 6.79 (m, 8H), 3.89 (t, $J = 7.2$ Hz, 2H), 3.72 (d, $J = 1.0$ Hz, 12H), 1.81 – 1.76 (m, 2H), 1.45 (m, 2H), 1.33 – 1.28 (m, 4H), 0.90 – 0.79 (m, 3H). ^{13}C NMR (151 MHz, THF- d_8) δ 156.25, 148.02, 143.76, 140.94, 135.12, 132.01, 126.56, 126.35, 124.88, 124.64, 120.72, 115.40, 114.49, 54.64, 47.08, 31.57, 26.86, 24.85, 24.72, 22.61, 13.42. MS/ESI $^+$: 889.27 a.m.u.

8.2.15 3,7-bis(1,2-dihydroacenaphthylen-5-yl)-10-hexyl-10H-phenothiazine (**1b**)



This compound was obtained by applying the same protocol as for the compound **1c**. Yield : 359 mg, 67%. ¹H NMR (600 MHz, CDCl₃) δ: 7.73 – 7.71 (m, 2H), 7.42 (dd, J = 8.4, 6.8 Hz, 2H), 7.38 – 7.34 (m, 6H), 7.32 – 7.28 (m, 4H), 7.00 (d, J = 8.8 Hz, 2H), 3.98 – 3.94 (m, 2H), 3.44 – 3.40 (m, 8H), 1.93 (q, J = 7.5 Hz, 2H), 1.51 (dd, J = 8.6, 6.6 Hz, 2H), 1.39 – 1.33 (m, 4H), 0.93 – 0.89 (m, 3H). MS/ESI⁺: 587.19 a.m.u.

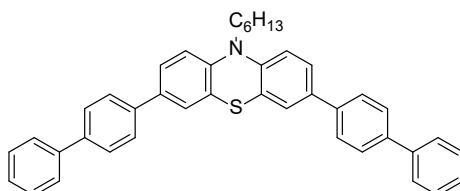
8.2.16 3,7-bis(4-(9H-carbazol-9-yl)phenyl)-10-hexyl-10H-phenothiazine (**1d**)



This compound was obtained by applying the same protocol as for the compound **1c**. Yield: 647 mg, 74% yield. ¹H NMR (600 MHz, CDCl₃) δ 8.15 (m, 4H), 7.78 – 7.74 (m, 4H), 7.64 – 7.59 (m, 4H), 7.50 – 7.45 (m, 8H), 7.42 (m, 4H), 7.30 (m, 4H), 7.01 – 6.98 (m, 2H), 3.95 (t, J = 7.3 Hz, 2H), 1.91 (m, 2H), 1.54 – 1.48 (m, 2H), 1.37 (m, 4H), 0.93 – 0.90 (m, 3H). ¹³C NMR (151 MHz, CDCl₃) δ 144.62, 140.95, 139.15, 136.65,

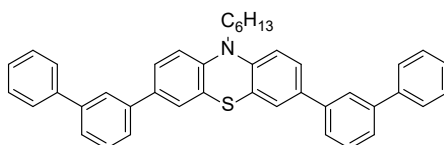
134.70, 127.91, 127.47, 126.14, 126.06, 125.97, 124.98, 123.50, 120.43, 120.06, 115.75, 109.94, 47.82, 31.62, 26.98, 26.82, 22.75, 14.15. MS/ESI⁺: 765.28 a.m.u.

8.2.17 3,7-di([1,1'-biphenyl]-4-yl)-10-hexyl-10H-phenothiazine (**1e**)



This compound was obtained by applying the same protocol as for the compound **1c**. Yield: 346 mg, 67%. ¹H NMR (600 MHz, CDCl₃) δ 7.66 – 7.60 (m, 12H), 7.46 – 7.42 (m, 8H), 7.37 – 7.33 (m, 2H), 6.94 (d, J = 9.0 Hz, 2H), 3.93 – 3.88 (m, 2H), 1.87 (p, J = 7.5 Hz, 2H), 1.47 (t, J = 7.5 Hz, 2H), 1.34 (m, 4H), 0.91 – 0.87 (m, 3H). MS/ESI⁺: 587.19 a.m.u.

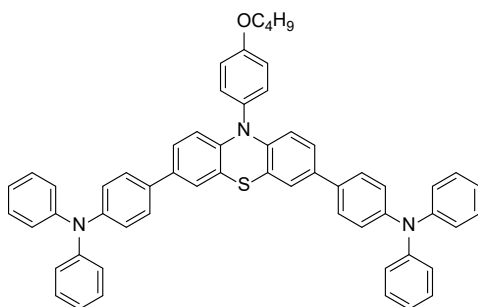
8.2.18 3,7-di([1,1'-biphenyl]-3-yl)-10-hexyl-10H-phenothiazine (**1f**)



This compound was obtained by applying the same protocol as for the compound **1c**. Yield: 460 mg, 57%. ¹H NMR (600 MHz, CDCl₃) δ 7.66 – 7.60 (m, 12H), 7.46 – 7.42 (m, 8H), 7.37 – 7.33 (m, 2H), 6.94 (d, J = 9.0 Hz, 2H), 3.93 – 3.88 (m, 2H), 1.87 (p, J =

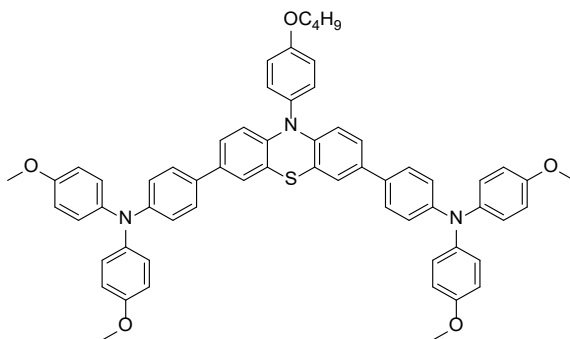
7.5 Hz, 2H), 1.47 (t, J = 7.5 Hz, 2H), 1.34 (m, 4H), 0.91 – 0.87 (m, 3H). ^{13}C NMR (151 MHz, CDCl_3) δ 144.51, 141.91, 141.27, 140.63, 135.54, 129.31, 128.90, 127.51, 127.36, 126.18, 126.05, 125.95, 125.58, 125.55, 124.86, 115.59, 47.73, 31.60, 26.96, 26.80, 22.73, 14.12, 1.12. MS/ESI⁺: 588.17 a.m.u.

8.2.19 4,4'-(10-(4-butoxyphenyl)-10H-phenothiazine-3,7-diyl)bis(N,N-diphenylaniline) (**2c**)



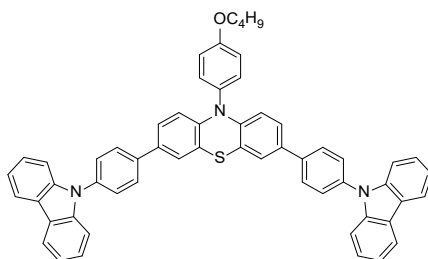
This compound was obtained by applying the same protocol as for the compound **1c**. Yield: 2.8 g, 80%. ^1H NMR (600 MHz, THF-d_8) δ 7.40 – 7.36 (m, 4H), 7.33 – 7.30 (m, 2H), 7.22 – 7.14 (m, 12H), 7.05 – 7.00 (m, 14H), 6.97 – 6.93 (m, 4H), 6.19 (d, J = 8.6 Hz, 2H), 4.05 (t, J = 6.4 Hz, 2H), 1.82 – 1.77 (m, 2H), 1.53 (dt, J = 14.9, 7.5 Hz, 2H), 0.99 (t, J = 7.4 Hz, 3H). ^{13}C NMR (151 MHz, THF-d_8) δ 147.86, 146.94, 143.33, 134.75, 134.07, 132.03, 129.10, 126.77, 124.58, 124.14, 124.04, 122.69, 119.78, 116.34, 115.79, 66.97, 31.42, 19.26, 13.28. MS/ESI⁺: 838.39 a.m.u.

8.2.20 4,4'-(10-(4-butoxyphenyl)-10H-phenothiazine-3,7-diyl)bis(N,N-bis(4-methoxyphenyl)aniline) (**2k**)



This compound was obtained by applying the same protocol as for the compound **1c**. Yield : 635 mg, 84% ^1H NMR (600 MHz, $\text{THF-}d_8$) δ 7.31 – 7.27 (m, 6H), 7.18 – 7.13 (m, 4H), 7.00 – 6.96 (m, 10H), 6.87 – 6.84 (m, 4H), 6.81 – 6.78 (m, 8H), 6.17 (d, $J = 8.6$ Hz, 2H), 4.04 (t, $J = 6.4$ Hz, 2H), 3.71 (d, $J = 0.7$ Hz, 12H), 1.80 – 1.77 (m, 2H), 1.57 – 1.50 (m, 2H), 0.99 (t, $J = 7.4$ Hz, 3H). MS/ESI $^+$: 953.39 a.m.u.

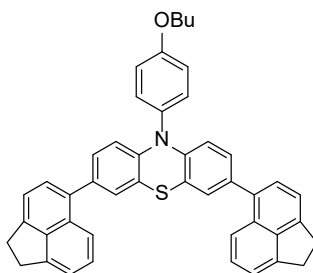
8.2.21 3,7-bis(4-(9H-carbazol-9-yl)phenyl)-10-(4-butoxyphenyl)-10H-phenothiazine (**2d**)



This compound was obtained by applying the same protocol as for the compound **1c**. Yield: 725 mg, 88%. ^1H NMR (600 MHz, $\text{THF-}d_8$) δ 8.11 (m, 4H), 7.84 – 7.78 (m,

4H), 7.62 – 7.58 (m, 4H), 7.44 – 7.31 (m, 12H), 7.25 – 7.18 (m, 8H), 6.31 (d, J = 8.6 Hz, 2H), 4.08 (t, J = 6.4 Hz, 2H), 1.86 – 1.78 (m, 2H), 1.60 – 1.51 (m, 2H), 1.01 (t, J = 7.4 Hz, 3H). ¹³C NMR (151 MHz, THF-d₈) δ 159.43, 143.95, 140.87, 138.91, 136.62, 134.40, 132.88, 132.02, 127.50, 127.22, 125.74, 125.22, 124.70, 123.51, 120.03, 119.79, 116.48, 116.03, 109.58, 67.76, 31.44, 19.29, 13.30. MS/ESI⁺: 773.26 a.m.u.

8.2.22 10-(4-butoxyphenyl)-3,7-bis(1,2-dihydroacenaphthylen-5-yl)-10H-phenothiazine (**2b**)

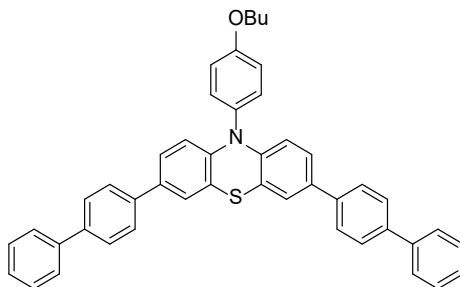


This compound was obtained by applying the same protocol as for the compound **1c**. Yield : 346 mg (yellow solid), 67%. ¹H NMR (600 MHz, CDCl₃) δ: 7.70 (dd, J = 8.3, 0.9 Hz, 2H), 7.43 – 7.38 (m, 4H), 7.33 (d, J = 7.1 Hz, 2H), 7.30 – 7.26 (m, 4H), 7.22 (d, J = 2.0 Hz, 2H), 7.17 – 7.14 (m, 2H), 7.04 (dd, J = 8.4, 2.1 Hz, 2H), 6.34 (d, J = 8.4 Hz, 2H), 4.06 (t, J = 6.5 Hz, 2H), 3.43 – 3.38 (m, 8H), 1.86 – 1.81 (m, 2H), 1.57 – 1.55 (m, 2H), 1.01 (t, J = 7.4 Hz, 3H). ¹³C NMR (151 MHz, THF-d₈) δ 146.03, 145.23, 143.75, 139.62, 134.74, 132.15, 129.79, 128.05, 127.82, 127.73, 127.37, 120.51, 119.71,

119.07, 118.87, 116.39, 115.50, 31.43, 30.21, 29.67, 24.85, 19.26, 13.27. MS/ESI⁺:

651.29 a.m.u.

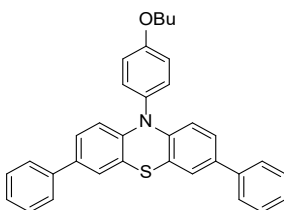
8.2.23 3,7-di([1,1'-biphenyl]-4-yl)-10-(4-butoxyphenyl)-10H-phenothiazine (**2e**)



This compound was obtained by applying the same protocol as for the compound

1c. Yield: 330 mg, 64%. ¹H NMR (600 MHz, CDCl₃) δ 7.63 – 7.54 (m, 12H), 7.45 – 7.41 (m, 4H), 7.35 – 7.32 (m, 4H), 7.29 (d, J = 2.2 Hz, 2H), 7.15 – 7.09 (m, 4H), 6.26 (d, J = 8.5 Hz, 2H), 4.06 (t, J = 6.5 Hz, 2H), 1.88 – 1.81 (m, 2H), 1.57 (d, J = 7.6 Hz, 2H), 1.02 (t, J = 7.4 Hz, 3H). MS/ESI⁺: 651.35 a.m.u.

8.2.24 10-(4-butoxyphenyl)-3,7-diphenyl-10H-phenothiazine (**2g**)

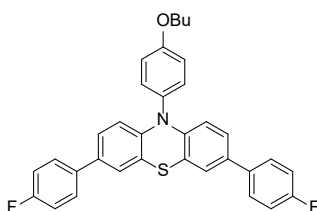


This compound was obtained by applying the same protocol as for the compound

1c. Yield: 333 mg, 42%. ¹H NMR (600 MHz, CDCl₃) δ 7.66 – 7.60 (m, 12H), 7.46 – 7.42

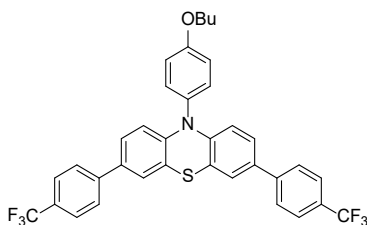
(m, 8H), 7.37 – 7.33 (m, 2H), 6.94 (d, J = 9.0 Hz, 2H), 3.93 – 3.88 (m, 2H), 1.87 (p, J = 7.5 Hz, 2H), 1.47 (t, J = 7.5 Hz, 2H), 1.34 (m, 4H), 0.91 – 0.87 (m, 3H). MS/ESI⁺: 499.14 a.m.u.

8.2.25 10-(4-butoxyphenyl)-3,7-bis(4-fluorophenyl)-10H-phenothiazine (**2h**)



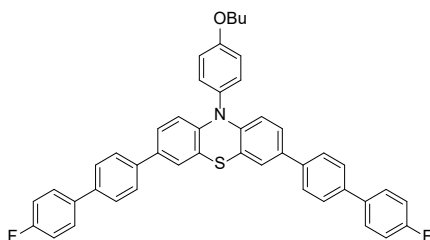
This compound was obtained by applying the same protocol as for the compound **1c**. Yield: 685 mg, 65 %. ¹H NMR (600 MHz, CDCl₃) δ 7.43 – 7.39 (m, 4H), 7.32 – 7.29 (m, 2H), 7.17 (d, J = 2.2 Hz, 2H), 7.14 – 7.11 (m, 2H), 7.08 – 7.03 (m, 4H), 6.99 (dd, J = 8.5, 2.2 Hz, 2H), 6.22 (d, J = 8.6 Hz, 2H), 4.05 (t, J = 6.5 Hz, 2H), 1.87 – 1.78 (m, 2H), 1.57 (s, 2H), 1.02 (t, J = 7.4 Hz, 3H). MS/ESI⁺: 535.13 a.m.u.

8.2.26 10-(4-butoxyphenyl)-3,7-bis(4-(trifluoromethyl)phenyl)-10H-phenothiazine (**2i**)



This compound was obtained by applying the same protocol as for the compound **1c**. Yield: 375 mg, 49%. $^1\text{H NMR}$ (600 MHz, CDCl_3) δ 7.66 – 7.60 (m, 12H), 7.46 – 7.42 (m, 8H), 7.37 – 7.33 (m, 2H), 6.94 (d, $J = 9.0$ Hz, 2H), 3.93 – 3.88 (m, 2H), 1.87 (p, $J = 7.5$ Hz, 2H), 1.47 (t, $J = 7.5$ Hz, 2H), 1.34 (m, 4H), 0.91 – 0.87 (m, 3H). MS/ESI $^+$: 635.15 a.m.u.

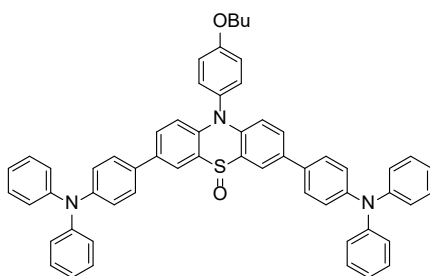
8.2.27 10-(4-butoxyphenyl)-3,7-bis(4'-fluoro-[1,1'-biphenyl]-4-yl)-10H-phenothiazine (**2j**)



This compound was obtained by applying the same protocol as for the compound **1c**. Yield: 480 mg, 70%. $^1\text{H NMR}$ (600 MHz, THF-d_8) δ 7.69 – 7.56 (m, 12H), 7.36 – 7.31

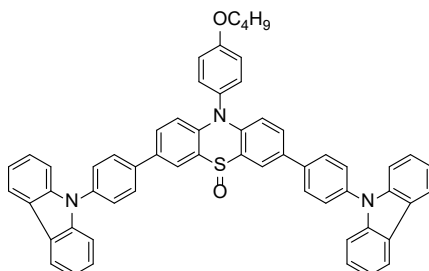
(m, 4H), 7.22 – 7.10 (m, 8H), 6.24 (d, $J = 8.5$ Hz, 2H), 4.06 (t, $J = 6.4$ Hz, 2H), 1.85 – 1.74 (m, 2H), 1.61 – 1.48 (m, 2H), 1.00 (t, $J = 7.4$ Hz, 3H). ^{13}C NMR (151 MHz, THF- d_8) δ 161.75, 159.35, 143.73, 138.58 (d, $J = 4.5$ Hz), 136.96, 134.58, 132.96, 131.99, 128.41, 128.36, 127.04, 126.36, 124.98, 119.89, 116.41, 115.91, 115.45, 115.31, 67.73, 31.43, 19.27, 13.29. MS/ESI $^+$: 829.28 a.m.u.

8.2.28 10-(4-butoxyphenyl)-3,7-bis(4-(diphenylamino)phenyl)-10H-phenothiazine 5-oxide (**3c**)



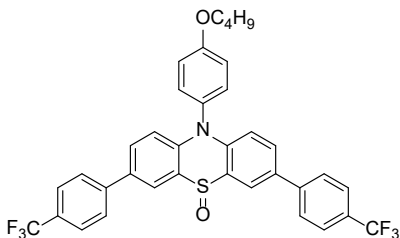
This compound was obtained by applying the same protocol as for the compound **1c**. Yield: 650 mg, 49%. ^1H NMR (600 MHz, THF- d_8) δ 8.19 (d, $J = 2.2$ Hz, 2H), 7.63 (dd, $J = 8.9, 2.3$ Hz, 2H), 7.57 – 7.54 (m, 4H), 7.38 – 7.34 (m, 2H), 7.25 – 7.19 (m, 10H), 7.10 – 7.05 (m, 12H), 6.97 (m, 4H), 6.80 (d, $J = 8.9$ Hz, 2H), 4.09 (t, $J = 6.4$ Hz, 2H), 1.82 (m, 2H), 1.56 (m, 2H), 1.01 (m, 3H). ^{13}C NMR (151 MHz, THF- d_8) δ 159.90, 147.82, 147.32, 138.05, 134.24, 133.53, 131.41, 129.72, 129.16, 129.03, 127.20, 124.81, 124.28, 124.02, 122.84, 117.56, 116.57, 67.86, 31.40, 19.26, 13.28. MS/ESI $^+$: 849.27 a.m.u.

8.2.29 3,7-bis(4-(9H-carbazol-9-yl)phenyl)-10-(4-butoxyphenyl)-10H-phenothiazine 5-oxide (**3d**)



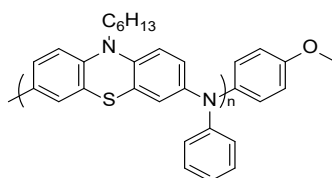
This compound was obtained by applying the same protocol as for the compound **1c**. Yield: 715 mg, 73%. ^1H NMR (600 MHz, CDCl_3) δ 8.35 (d, $J = 2.2$ Hz, 2H), 8.16 (m, 4H), 7.86 – 7.82 (m, 4H), 7.75 (dd, $J = 8.8, 2.3$ Hz, 2H), 7.69 – 7.65 (m, 4H), 7.49 (m, 4H), 7.43 (m, 4H), 7.41 – 7.38 (m, 2H), 7.31 (m, 4H), 7.24 (d, $J = 7.0$ Hz, 1H), 6.95 (d, $J = 8.8$ Hz, 2H), 4.13 (t, $J = 6.4$ Hz, 2H), 1.97 – 1.85 (m, 2H), 1.62 – 1.58 (m, 2H), 1.06 (t, $J = 7.4$ Hz, 3H). ^{13}C NMR (151 MHz, CDCl_3) δ 159.98, 140.89, 138.64, 138.38, 137.19, 134.45, 131.40, 131.34, 131.27, 130.27, 128.18, 127.66, 126.11, 123.57, 122.99, 120.45, 120.16, 118.36, 117.01, 109.92, 68.33, 31.40, 19.41, 13.99.

8.2.30 10-(4-butoxyphenyl)-3,7-bis(4-(trifluoromethyl)phenyl)-10H-phenothiazine 5-oxide (**3i**)



This compound was obtained by applying the same protocol as for the compound **1c**. Yield : 380 mg, 56%, ^1H NMR (600 MHz, Acetone- d_6) δ 8.39 (t, J = 2.5 Hz, 2H), 7.98 (dd, J = 8.5, 2.5 Hz, 4H), 7.90 (m, 2H), 7.80 (dd, J = 8.6, 2.5 Hz, 4H), 7.42 (dd, J = 8.8, 2.7 Hz, 2H), 7.37 – 7.29 (m, 2H), 6.94 (dd, J = 8.9, 2.6 Hz, 2H), 4.16 (m, 2H), 1.83 (m, 2H), 1.59 – 1.51 (m, 2H), 1.00 (m, 3H). ^{13}C NMR (151 MHz, Acetone- d_6) δ 160.11, 142.95, 139.04, 133.13, 131.41, 131.29, 131.14, 130.12, 128.91, 127.23, 125.98 (q, J = 4.5 Hz), 124.46, 118.33, 68.04, 31.25, 19.12, 13.31. MS/ESI $^+$: 652.07 a.m.u.

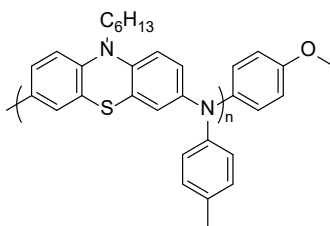
8.2.31 P1a Polymer



The *t*-BuOK (610.37 mg, 5.44 mmol, 4 eq) was inserted into a 20 ml reactor and heated with heating-gun under applied vacuum. The vial was fluxed with argon until it reached room temperature. The 3,7-dibromo-10-hexyl-10H-phenothiazine (600 mg, 1.36 mmol, 1 eq) and the catalyst and (IPr)Pd(allyl)Cl (15.54 mg, 0.027 mmol, 0.02 eq) were added in the vial under argon. The system was evacuated for 10 min and then filled again with argon. Dry toluene (5 ml), freshly distilled aniline (127 mg, 124 microliters, 1.36 mmol, 1 eq) and a 50 mmol/L solution of 4-bromoanisole in toluene (1.53 mg, 0.206 ml, 8.16 μ mol, 0.01 eq) were added in sequence. The vial was heated using an oil bath at 105 °C and stirred for 22 hours. At the end, the mixture was left to cool and was precipitated from methanol. The crude was dissolved into dichloromethane and filtered through a short pad of silica and then washed with a 0.1 M of sodium diethyldithiocarbamate solution to remove any remaining traces of Pd. The organic phase was dried with MgSO₄ and concentrated under vacuum. The product was obtained from the concentrated solution by precipitation with methanol. The crude has been extracted four times with Soxhlet with the following solvents in succession: methanol, hexane, acetone, and

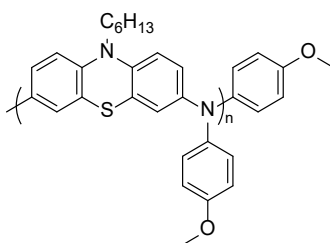
dichloromethane. The solution extracted with dichloromethane was concentrated, precipitated in methanol and the final product was recovered by filtration (100 mg, 18.3%). ^1H NMR (600 MHz, THF- d_8) δ 7.30 – 6.57 (m, 11H), 3.85 (m, 2H), 1.80 (s, 2H), 1.46 (s, 2H), 1.32 (m, 4H), 0.87 (m, 3H). SEC (35°C, THF): M_n = 4.9 KDa; M_w = 6.1 KDa; PDI= 1.2.

8.2.32 P1b Polymer



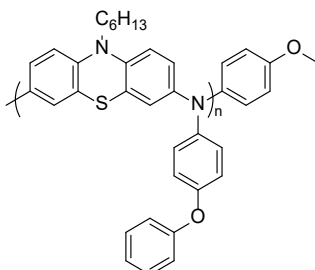
P1b was prepared using the same method used for the preparation of **P1a**. Yield: 185 mg, 19.6 %. ^1H NMR (600 MHz, THF- d_8) δ 7.31 – 6.53 (m, 10H), 3.78 (s, 2H), 2.27 – 2.08 (m, 3H), 1.76 (s, 2H), 1.44 (s, 2H), 1.32 (m, 4H), 0.87 (m, 3H). SEC (35°C, THF): M_n = 5.9 KDa; M_w = 7.7 KDa; PDI= 1.3.

8.2.33 P1c Polymer



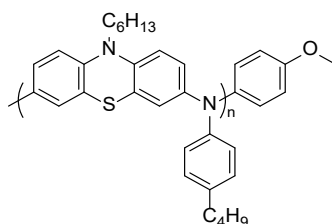
P1c was prepared using the same method used for the preparation of **P1a**. Yield: 397 mg, 40.5 %. ¹H NMR (600 MHz, THF-d₈) δ : 7.27 – 6.48 (m, 10H), 3.97 – 3.64 (m, 5H), 1.85 (s, 2H), 1.45 (s, 2H), 1.32 (s, 4H), 0.86 (m, 3H). SEC (35°C, THF): M_n= 5.0 KDa; M_w= 8.1 KDa; PDI= 1.6.

8.2.34 P1d Polymer



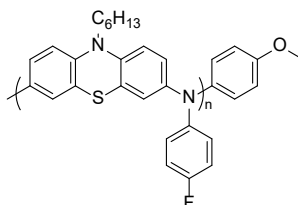
P1d was prepared using the same method used for the preparation of **P1a**. Yield: 488 mg 43.6 %. ¹H NMR (600 MHz, THF-d₈) δ : 7.45 – 6.59 (m, 15H), 3.98 – 3.71 (m, 2H), 1.78 (s, 2H), 1.45 (s, 2H), 1.34 (m, 2H), 0.88 (t, J = 1.2 Hz, 3H). SEC (35°C, THF): M_n= 2.5 KDa; M_w= 3.3 KDa; PDI= 1.3.

8.2.35 P1e Polymer



P1e was prepared using the same method used for the preparation of **P1a**. Acetone soluble polymer yield: 349 mg, 33.6%. DCM soluble polymer yield: 214 mg, 20.6%. ¹H NMR (600 MHz, THF-d₈) δ: 7.34 – 6.48 (m, 10H), 3.79 (s, 2H), 2.52 (s, 2H), 1.77 (s, 2H), 1.55 (s, 2H), 1.45 (s, 2H), 1.34 – 1.26 (m, 6H), 0.87 (t, 3H). SEC (35°C, THF): M_n= 5.6 KDa; M_w= 7.9 KDa; PDI= 1.4.

8.2.36 P1f Polymer



P1f was prepared using the same method used for the preparation of **P1a**. Yield: 355 mg, 37.3%. ¹H NMR (600 MHz, THF-d₈) δ : 7.29 – 6.58 (m, 10H), 3.79 (s, 2H), 1.78 (s, 2H), 1.45 (s, 2H), 1.32 (d, 4H), 0.88 (s, 3H). SEC (35°C, THF): M_n= 4.3 KDa; M_w= 5.9 KDa; PDI= 1.4.

9 REFERENCES

- (1) Nonrenewable Resources Definition
<https://www.investopedia.com/terms/n/nonrenewableresource.asp>
(accessed 2022 -01 -27).
- (2) Глобальное изменение климата - проблемы потепления климата - изменение климата на Земле - ТАСС <https://tass.ru/спец/climate>
(accessed 2022 -01 -27).
- (3) Pal, J. S.; Eltahir, E. A. B. Future Temperature in Southwest Asia Projected to Exceed a Threshold for Human Adaptability. *Nat. Clim. Chang.* **2016**, *6* (2), 197–200. <https://doi.org/10.1038/nclimate2833>.
- (4) Gulf will be too hot for humans by 2070: study | Environment – Gulf News <https://gulfnews.com/uae/environment/gulf-will-be-too-hot-for-humans-by-2070-study-1.1608055> (accessed 2022 -01 -27).
- (5) This Incredible Fact Should Get You Psyched About Solar Power <https://www.businessinsider.com/solar-power-potential-how-much-energy-does-sun-have-2017-3?r=US&IR=T> (accessed 2022 -01 -27).
- (6) Strielkowski, W.; Civín, L.; Tarkhanova, E.; Tvaronavičienė, M.; Petrenko, Y. Renewable Energy in the Sustainable Development of Electrical Power Sector: A Review. *Energies* **2021**, *14* (24), 8240.

<https://doi.org/10.3390/en14248240>.

- (7) Renewable Capacity Statistics 2019. */publications/2019/Mar/Renewable-Capacity-Statistics-2019*.
- (8) Kusch-Brandt. Urban Renewable Energy on the Upswing: A Spotlight on Renewable Energy in Cities in REN21's "Renewables 2019 Global Status Report." *Resources* **2019**, *8* (3), 139.
<https://doi.org/10.3390/resources8030139>.
- (9) Pham, H. D.; Yang, T. C. J.; Jain, S. M.; Wilson, G. J.; Sonar, P. Development of Dopant-Free Organic Hole Transporting Materials for Perovskite Solar Cells. *Adv. Energy Mater.* **2020**, *10* (13), 1903326.
<https://doi.org/10.1002/aenm.201903326>.
- (10) Chakhmouradian, A. R.; Woodward, P. M. Celebrating 175 Years of Perovskite Research: A Tribute to Roger H. Mitchell. *Phys. Chem. Miner.* **2014**, *41* (6), 387–391. <https://doi.org/10.1007/s00269-014-0678-9>.
- (11) Kojima, A.; Teshima, K.; Shirai, Y.; Miyasaka, T. Organometal Halide Perovskites as Visible-Light Sensitizers for Photovoltaic Cells. *J. Am. Chem. Soc.* **2009**, *131* (17), 6050–6051. <https://doi.org/10.1021/ja809598r>.
- (12) Calió, L.; Kazim, S.; Grätzel, M.; Ahmad, S. Hole-Transport Materials for Perovskite Solar Cells. *Angew. Chemie Int. Ed.* **2016**, *55* (47), 14522–14545.
<https://doi.org/10.1002/anie.201601757>.

- (13) Rakstys, K.; Igci, C.; Nazeeruddin, M. K. Efficiency: Vs. Stability: Dopant-Free Hole Transporting Materials towards Stabilized Perovskite Solar Cells. *Chem. Sci.* **2019**, *10* (28), 6748–6769. <https://doi.org/10.1039/c9sc01184f>.
- (14) Kim, H.-S.; Lee, C.-R.; Im, J.-H.; Lee, K.-B.; Moehl, T.; Marchioro, A.; Moon, S.-J.; Humphry-Baker, R.; Yum, J.-H.; Moser, J. E.; Grätzel, M.; Park, N.-G. Lead Iodide Perovskite Sensitized All-Solid-State Submicron Thin Film Mesoscopic Solar Cell with Efficiency Exceeding 9%. *Sci. Rep.* **2012**, *2* (1), 591. <https://doi.org/10.1038/srep00591>.
- (15) Lee, M. M.; Teuscher, J.; Miyasaka, T.; Murakami, T. N.; Snaith, H. J. Efficient Hybrid Solar Cells Based on Meso-Superstructured Organometal Halide Perovskites. *Science* **2012**, *338* (6107), 643–647. <https://doi.org/10.1126/science.1228604>.
- (16) UNIST, EPFL claim 25.6% efficiency world record for perovskite solar cell – pv magazine International <https://www.pv-magazine.com/2021/04/06/unist-epfl-claim-25-6-efficiency-world-record-for-perovskite-solar-cell/> (accessed 2022 -01 -28).
- (17) NREL. Best Research-Cell Efficiencies: Emerging Photovoltaics (2022). *Best Research-Cell Efficiency Chart | Photovoltaic Research | NREL*. 2022, p <https://www.nrel.gov/pv/assets/pdfs/cell-pv-eff-em>.
- (18) Urieta-Mora, J.; García-Benito, I.; Molina-Ontoria, A.; Martín, N. Hole

Transporting Materials for Perovskite Solar Cells: A Chemical Approach.

Chem. Soc. Rev. **2018**, *47* (23), 8541–8571.

<https://doi.org/10.1039/C8CS00262B>.

- (19) Filatova, E. O.; Konashuk, A. S. Interpretation of the Changing the Band Gap of Al₂O₃ Depending on Its Crystalline Form: Connection with Different Local Symmetries. *J. Phys. Chem. C* **2015**, *119* (35), 20755–20761.
<https://doi.org/10.1021/acs.jpcc.5b06843>.
- (20) Che, M.; Zhu, L.; Zhao, Y. L.; Yao, D. S.; Gu, X. Q.; Song, J.; Qiang, Y. H. Enhancing Current Density of Perovskite Solar Cells Using TiO₂-ZrO₂ Composite Scaffold Layer. *Mater. Sci. Semicond. Process.* **2016**, *56*, 29–36.
<https://doi.org/10.1016/j.mssp.2016.07.003>.
- (21) Yang, W. S.; Park, B.-W.; Jung, E. H.; Jeon, N. J.; Kim, Y. C.; Lee, D. U.; Shin, S. S.; Seo, J.; Kim, E. K.; Noh, J. H.; Seok, S. Il. Iodide Management in Formamidinium-Lead-Halide-Based Perovskite Layers for Efficient Solar Cells. *Science* **2017**, *356* (6345), 1376–1379.
<https://doi.org/10.1126/science.aan2301>.
- (22) Roose, B.; Baena, J.-P. C.; Gödel, K. C.; Graetzel, M.; Hagfeldt, A.; Steiner, U.; Abate, A. Mesoporous SnO₂ Electron Selective Contact Enables UV-Stable Perovskite Solar Cells. *Nano Energy* **2016**, *30* (October), 517–522.
<https://doi.org/10.1016/j.nanoen.2016.10.055>.

- (23) Yu, Y.; Li, J.; Geng, D.; Wang, J.; Zhang, L.; Andrew, T. L.; Arnold, M. S.; Wang, X. Development of Lead Iodide Perovskite Solar Cells Using Three-Dimensional Titanium Dioxide Nanowire Architectures. *ACS Nano* **2015**, *9* (1), 564–572. <https://doi.org/10.1021/nn5058672>.
- (24) Xiong, L.; Qin, M.; Chen, C.; Wen, J.; Yang, G.; Guo, Y.; Ma, J.; Zhang, Q.; Qin, P.; Li, S.; Fang, G. Fully High-Temperature-Processed SnO₂ as Blocking Layer and Scaffold for Efficient, Stable, and Hysteresis-Free Mesoporous Perovskite Solar Cells. *Adv. Funct. Mater.* **2018**, *28* (10), 1706276. <https://doi.org/10.1002/adfm.201706276>.
- (25) *Nanostructured Materials for Next-Generation Energy Storage and Conversion*; Atesin, T. A., Bashir, S., Liu, J. L., Eds.; Springer Berlin Heidelberg: Berlin, Heidelberg, 2019. <https://doi.org/10.1007/978-3-662-59594-7>.
- (26) Li, W.; Liu, J.; Zhao, D. Mesoporous Materials for Energy Conversion and Storage Devices. *Nat. Rev. Mater.* **2016**, *1* (6), 16023. <https://doi.org/10.1038/natrevmats.2016.23>.
- (27) Eperon, G. E.; Burlakov, V. M.; Docampo, P.; Goriely, A.; Snaith, H. J. Morphological Control for High Performance, Solution-Processed Planar Heterojunction Perovskite Solar Cells. *Adv. Funct. Mater.* **2014**, *24* (1), 151–157. <https://doi.org/10.1002/adfm.201302090>.
- (28) Zhou, Z.; Li, X.; Cai, M.; Xie, F.; Wu, Y.; Lan, Z.; Yang, X.; Qiang, Y.; Islam, A.;

- Han, L. Stable Inverted Planar Perovskite Solar Cells with Low-Temperature-Processed Hole-Transport Bilayer. *Adv. Energy Mater.* **2017**, 7 (22), 1700763. <https://doi.org/10.1002/aenm.201700763>.
- (29) Liu, M.; Johnston, M. B.; Snaith, H. J. Efficient Planar Heterojunction Perovskite Solar Cells by Vapour Deposition. *Nature* **2013**, 501 (7467), 395–398. <https://doi.org/10.1038/nature12509>.
- (30) Liu, X.; Cheng, Y.; Liu, C.; Zhang, T.; Zhang, N.; Zhang, S.; Chen, J.; Xu, Q.; Ouyang, J.; Gong, H. 20.7% Highly Reproducible Inverted Planar Perovskite Solar Cells with Enhanced Fill Factor and Eliminated Hysteresis. *Energy Environ. Sci.* **2019**, 12 (5), 1622–1633. <https://doi.org/10.1039/C9EE00872A>.
- (31) Yang, L.; Cai, F.; Yan, Y.; Li, J.; Liu, D.; Pearson, A. J.; Wang, T. Conjugated Small Molecule for Efficient Hole Transport in High-Performance p-i-n Type Perovskite Solar Cells. *Adv. Funct. Mater.* **2017**, 27 (31), 1702613. <https://doi.org/10.1002/adfm.201702613>.
- (32) Urieta-Mora, J.; García-Benito, I.; Molina-Ontoria, A.; Martín, N. Hole Transporting Materials for Perovskite Solar Cells: A Chemical Approach. *Chem. Soc. Rev.* **2018**, 47 (23), 8541–8571. <https://doi.org/10.1039/C8CS00262B>.
- (33) Ming, W.; Yang, D.; Li, T.; Zhang, L.; Du, M. Formation and Diffusion of Metal Impurities in Perovskite Solar Cell Material $\text{CH}_3\text{NH}_3\text{PbI}_3$: Implications on

- Solar Cell Degradation and Choice of Electrode. *Adv. Sci.* **2018**, *5* (2), 1700662. <https://doi.org/10.1002/advs.201700662>.
- (34) Domanski, K.; Correa-Baena, J.-P.; Mine, N.; Nazeeruddin, M. K.; Abate, A.; Saliba, M.; Tress, W.; Hagfeldt, A.; Grätzel, M. Not All That Glitters Is Gold: Metal-Migration-Induced Degradation in Perovskite Solar Cells. *ACS Nano* **2016**, *10* (6), 6306–6314. <https://doi.org/10.1021/acsnano.6b02613>.
- (35) Kato, Y.; Ono, L. K.; Lee, M. V.; Wang, S.; Raga, S. R.; Qi, Y. Silver Iodide Formation in Methyl Ammonium Lead Iodide Perovskite Solar Cells with Silver Top Electrodes. *Adv. Mater. Interfaces* **2015**, *2* (13), 1500195. <https://doi.org/10.1002/admi.201500195>.
- (36) Zhao, J.; Zheng, X.; Deng, Y.; Li, T.; Shao, Y.; Gruverman, A.; Shield, J.; Huang, J. Is Cu a Stable Electrode Material in Hybrid Perovskite Solar Cells for a 30-Year Lifetime? *Energy Environ. Sci.* **2016**, *9* (12), 3650–3656. <https://doi.org/10.1039/C6EE02980A>.
- (37) Deng, Y.; Dong, Q.; Bi, C.; Yuan, Y.; Huang, J.; Deng, Y.; Dong, Q.; Bi, C.; Yuan, Y.; Huang, J. Air-Stable, Efficient Mixed-Cation Perovskite Solar Cells with Cu Electrode by Scalable Fabrication of Active Layer. *Adv. Energy Mater.* **2016**, *6*, 1600372. <https://doi.org/10.1002/aenm.201600372>.
- (38) Jiang, Q.; Sheng, X.; Shi, B.; Feng, X.; Xu, T. Nickel-Cathoded Perovskite Solar Cells. *J. Phys. Chem. C* **2014**, *118* (45), 25878–25883.

<https://doi.org/10.1021/jp506991x>.

- (39) Wang, Y.; Yue, Y.; Yang, X.; Han, L. Toward Long-Term Stable and Highly Efficient Perovskite Solar Cells via Effective Charge Transporting Materials. *Adv. Energy Mater.* **2018**, *8* (22), 1800249.
<https://doi.org/10.1002/aenm.201800249>.
- (40) Zhang, W.; Wang, Y.-C.; Li, X.; Song, C.; Wan, L.; Usman, K.; Fang, J. Recent Advance in Solution-Processed Organic Interlayers for High-Performance Planar Perovskite Solar Cells. *Adv. Sci.* **2018**, *5* (7), 1800159.
<https://doi.org/10.1002/advs.201800159>.
- (41) Tong, X.; Lin, F.; Wu, J.; Wang, Z. M. High Performance Perovskite Solar Cells. *Adv. Sci.* **2016**, *3* (5), 1500201. <https://doi.org/10.1002/advs.201500201>.
- (42) Bi, E.; Chen, H.; Xie, F.; Wu, Y.; Chen, W.; Su, Y.; Islam, A.; Grätzel, M.; Yang, X.; Han, L. Diffusion Engineering of Ions and Charge Carriers for Stable Efficient Perovskite Solar Cells. *Nat. Commun.* **2017**, *8* (1), 15330.
<https://doi.org/10.1038/ncomms15330>.
- (43) Lian, J.; Lu, B.; Niu, F.; Zeng, P.; Zhan, X. Electron-Transport Materials in Perovskite Solar Cells. *Small Methods* **2018**, *2* (10), 1–27.
<https://doi.org/10.1002/smt.201800082>.
- (44) Huang, L.; Ge, Z. Simple, Robust, and Going More Efficient: Recent Advance on Electron Transport Layer-Free Perovskite Solar Cells. *Adv. Energy Mater.*

2019, 9 (24), 1–31. <https://doi.org/10.1002/aenm.201900248>.

- (45) Juarez-Perez, E. J.; Wußler, M.; Fabregat-Santiago, F.; Lakus-Wollny, K.; Mankel, E.; Mayer, T.; Jaegermann, W.; Mora-Sero, I. Role of the Selective Contacts in the Performance of Lead Halide Perovskite Solar Cells. *J. Phys. Chem. Lett.* **2014**, 5 (4), 680–685. <https://doi.org/10.1021/jz500059v>.
- (46) Bera, A.; Sheikh, A. D.; Haque, M. A.; Bose, R.; Alarousu, E.; Mohammed, O. F.; Wu, T. Fast Crystallization and Improved Stability of Perovskite Solar Cells with Zn₂SnO₄ Electron Transporting Layer: Interface Matters. *ACS Appl. Mater. Interfaces* **2015**, 7 (51), 12404–12411. <https://doi.org/10.1021/acsami.5b09182>.
- (47) Yun, A. J.; Kim, J.; Hwang, T.; Park, B. Origins of Efficient Perovskite Solar Cells with Low-Temperature Processed SnO₂ Electron Transport Layer. *ACS Appl. Energy Mater.* **2019**, 2 (5), 3554–3560. <https://doi.org/10.1021/acsaem.9b00293>.
- (48) Bera, A.; Wu, K.; Sheikh, A.; Alarousu, E.; Mohammed, O. F.; Wu, T. Perovskite Oxide SrTiO₃ as an Efficient Electron Transporter for Hybrid Perovskite Solar Cells. *J. Phys. Chem. C* **2014**, 118 (49), 28494–28501. <https://doi.org/10.1021/jp509753p>.
- (49) Zhen, C.; Wu, T.; Chen, R.; Wang, L.; Liu, G.; Cheng, H.-M. Strategies for Modifying TiO₂ Based Electron Transport Layers to Boost Perovskite Solar

Cells. *ACS Sustain. Chem. Eng.* **2019**, 7 (5), 4586–4618.

<https://doi.org/10.1021/acssuschemeng.8b06580>.

- (50) Sun, H.; Zhou, Y.; Xin, Y.; Deng, K.; Meng, L.; Xiong, J.; Li, L. Composition and Energy Band-Modified Commercial FTO Substrate for In Situ Formed Highly Efficient Electron Transport Layer in Planar Perovskite Solar Cells. *Adv. Funct. Mater.* **2019**, 29 (11), 1808667. <https://doi.org/10.1002/adfm.201808667>.
- (51) Liu, D.; Kelly, T. L. Perovskite Solar Cells with a Planar Heterojunction Structure Prepared Using Room-Temperature Solution Processing Techniques. *Nat. Photonics* **2014**, 8 (2), 133–138. <https://doi.org/10.1038/nphoton.2013.342>.
- (52) Zhang, H.; Xue, L.; Han, J.; Fu, Y. Q.; Shen, Y.; Zhang, Z.; Li, Y.; Wang, M. New Generation Perovskite Solar Cells with Solution-Processed Amino-Substituted Perylene Diimide Derivative as Electron-Transport Layer. *J. Mater. Chem. A* **2016**, 4 (22), 8724–8733. <https://doi.org/10.1039/C6TA03119F>.
- (53) Huang, J.; Gu, Z.; Zuo, L.; Ye, T.; Chen, H. Morphology Control of Planar Heterojunction Perovskite Solar Cells with Fluorinated PDI Films as Organic Electron Transport Layer. *Sol. Energy* **2016**, 133, 331–338. <https://doi.org/10.1016/j.solener.2016.04.017>.
- (54) Yang, D.; Yang, R.; Ren, X.; Zhu, X.; Yang, Z.; Li, C.; Liu, S. F. Hysteresis-

Suppressed High-Efficiency Flexible Perovskite Solar Cells Using Solid-State Ionic-Liquids for Effective Electron Transport. *Adv. Mater.* **2016**, *28* (26), 5206–5213. <https://doi.org/10.1002/adma.201600446>.

- (55) Yang, D.; Yang, R.; Priya, S.; Liu, S. (Frank). Recent Advances in Flexible Perovskite Solar Cells: Fabrication and Applications. *Angew. Chemie Int. Ed.* **2019**, *58* (14), 4466–4483. <https://doi.org/10.1002/anie.201809781>.
- (56) Bai, Y.; Dong, Q.; Shao, Y.; Deng, Y.; Wang, Q.; Shen, L.; Wang, D.; Wei, W.; Huang, J. Enhancing Stability and Efficiency of Perovskite Solar Cells with Crosslinkable Silane-Functionalized and Doped Fullerene. *Nat. Commun.* **2016**, *7*, 1–9. <https://doi.org/10.1038/ncomms12806>.
- (57) Azimi, H.; Ameri, T.; Zhang, H.; Hou, Y.; Quiroz, C. O. R.; Min, J.; Hu, M.; Zhang, Z.-G.; Przybilla, T.; Matt, G. J.; Spiecker, E.; Li, Y.; Brabec, C. J. A Universal Interface Layer Based on an Amine-Functionalized Fullerene Derivative with Dual Functionality for Efficient Solution Processed Organic and Perovskite Solar Cells. *Adv. Energy Mater.* **2015**, *5* (8), 1401692. <https://doi.org/10.1002/aenm.201401692>.
- (58) Zhu, Z.; Chueh, C.-C.; Lin, F.; Jen, A. K.-Y. Enhanced Ambient Stability of Efficient Perovskite Solar Cells by Employing a Modified Fullerene Cathode Interlayer. *Adv. Sci.* **2016**, *3* (9), 1600027. <https://doi.org/10.1002/advs.201600027>.

- (59) Gu, P.-Y.; Wang, N.; Wang, C.; Zhou, Y.; Long, G.; Tian, M.; Chen, W.; Sun, X. W.; Kanatzidis, M. G.; Zhang, Q. Pushing up the Efficiency of Planar Perovskite Solar Cells to 18.2% with Organic Small Molecules as the Electron Transport Layer. *J. Mater. Chem. A* **2017**, *5* (16), 7339–7344.
<https://doi.org/10.1039/C7TA01764B>.
- (60) Gu, P.-Y.; Wang, N.; Wu, A.; Wang, Z.; Tian, M.; Fu, Z.; Sun, X. W.; Zhang, Q. An Azaacene Derivative as Promising Electron-Transport Layer for Inverted Perovskite Solar Cells. *Chem. - An Asian J.* **2016**, *11* (15), 2135–2138.
<https://doi.org/10.1002/asia.201600856>.
- (61) Lin, Y.; Shen, L.; Dai, J.; Deng, Y.; Wu, Y.; Bai, Y.; Zheng, X.; Wang, J.; Fang, Y.; Wei, H.; Ma, W.; Zeng, X. C.; Zhan, X.; Huang, J. π -Conjugated Lewis Base: Efficient Trap-Passivation and Charge-Extraction for Hybrid Perovskite Solar Cells. *Adv. Mater.* **2017**, *29* (7), 1604545.
<https://doi.org/10.1002/adma.201604545>.
- (62) Zhao, L.; Kerner, R. A.; Xiao, Z.; Lin, Y. L.; Lee, K. M.; Schwartz, J.; Rand, B. P. Redox Chemistry Dominates the Degradation and Decomposition of Metal Halide Perovskite Optoelectronic Devices. *ACS Energy Lett.* **2016**, *1* (3), 595–602. <https://doi.org/10.1021/acsendergylett.6b00320>.
- (63) Sanhira, E. M.; Tremolet De Villers, B. J.; Schulz, P.; Reese, M. O.; Ferrere, S.; Zhu, K.; Lin, L. Y.; Berry, J. J.; Luther, J. M. Influence of Electrode Interfaces

on the Stability of Perovskite Solar Cells: Reduced Degradation Using

MoOx/Al for Hole Collection. *ACS Energy Lett.* **2016**, *1* (1), 38–45.

<https://doi.org/10.1021/acsenergylett.6b00013>.

- (64) Reddy, S. S.; Arivunithi, V. M.; Sree, V. G.; Kwon, H.; Park, J.; Kang, Y. C.; Zhu, H.; Noh, Y. Y.; Jin, S. H. Lewis Acid-Base Adduct-Type Organic Hole Transport Material for High Performance and Air-Stable Perovskite Solar Cells. *Nano Energy* **2019**, *58* (October 2018), 284–292.

<https://doi.org/10.1016/j.nanoen.2019.01.041>.

- (65) Yue, Y.; Salim, N. T.; Wu, Y.; Yang, X.; Islam, A.; Chen, W.; Liu, J.; Bi, E.; Xie, F.; Cai, M.; Han, L. Enhanced Stability of Perovskite Solar Cells through Corrosion-Free Pyridine Derivatives in Hole-Transporting Materials. *Adv. Mater.* **2016**, *28* (48), 10738–10743.

<https://doi.org/10.1002/adma.201602822>.

- (66) Saliba, M.; Orlandi, S.; Matsui, T.; Aghazada, S.; Cavazzini, M.; Correa-Baena, J.-P.; Gao, P.; Scopelliti, R.; Mosconi, E.; Dahmen, K.-H.; De Angelis, F.; Abate, A.; Hagfeldt, A.; Pozzi, G.; Graetzel, M.; Nazeeruddin, M. K. A Molecularly Engineered Hole-Transporting Material for Efficient Perovskite Solar Cells. *Nat. Energy* **2016**, *1* (2), 15017. <https://doi.org/10.1038/nenergy.2015.17>.

- (67) García-Benito, I.; Zimmermann, I.; Urieta-Mora, J.; Aragón, J.; Calbo, J.; Perles, J.; Serrano, A.; Molina-Ontoria, A.; Ortí, E.; Martín, N.; Nazeeruddin, M. K.

Heteroatom Effect on Star-Shaped Hole-Transporting Materials for

Perovskite Solar Cells. *Adv. Funct. Mater.* **2018**, *28* (31), 1–10.

<https://doi.org/10.1002/adfm.201801734>.

- (68) Ti, D.; Gao, K.; Zhang, Z. P.; Qu, L. T. Conjugated Polymers as Hole Transporting Materials for Solar Cells. *Chinese J. Polym. Sci. (English Ed.)* **2020**, *38* (5), 449–458. <https://doi.org/10.1007/s10118-020-2369-y>.
- (69) Petrus, M. L.; Schutt, K.; Sirtl, M. T.; Hutter, E. M.; Closs, A. C.; Ball, J. M.; Bijleveld, J. C.; Petrozza, A.; Bein, T.; Dingemans, T. J.; Savenije, T. J.; Snaith, H.; Docampo, P. New Generation Hole Transporting Materials for Perovskite Solar Cells: Amide-Based Small-Molecules with Nonconjugated Backbones. *Adv. Energy Mater.* **2018**, *8* (32), 1–11. <https://doi.org/10.1002/aenm.201801605>.
- (70) Petrus, M. L.; Bein, T.; Dingemans, T. J.; Docampo, P. A Low Cost Azomethine-Based Hole Transporting Material for Perovskite Photovoltaics. *J. Mater. Chem. A* **2015**, *3* (23), 12159–12162. <https://doi.org/10.1039/C5TA03046C>.
- (71) Vaitukaityte, D.; Wang, Z.; Malinauskas, T.; Magomedov, A.; Bubniene, G.; Jankauskas, V.; Getautis, V.; Snaith, H. J. Efficient and Stable Perovskite Solar Cells Using Low-Cost Aniline-Based Enamine Hole-Transporting Materials. *Adv. Mater.* **2018**, *30* (45), 1–7. <https://doi.org/10.1002/adma.201803735>.

- (72) Lim, K. G.; Kim, H. B.; Jeong, J.; Kim, H.; Kim, J. Y.; Lee, T. W. Boosting the Power Conversion Efficiency of Perovskite Solar Cells Using Self-Organized Polymeric Hole Extraction Layers with High Work Function. *Adv. Mater.* **2014**, *26* (37), 6461–6466. <https://doi.org/10.1002/adma.201401775>.
- (73) Lamberti, F.; Schmitz, F.; Chen, W.; He, Z.; Gatti, T. The Non-Innocent Role of Hole-Transporting Materials in Perovskite Solar Cells. *Sol. RRL* **2021**, *2100514*, 2100514. <https://doi.org/10.1002/solr.202100514>.
- (74) Singh, R.; Singh, P. K.; Bhattacharya, B.; Rhee, H.-W. Review of Current Progress in Inorganic Hole-Transport Materials for Perovskite Solar Cells. *Appl. Mater. Today* **2019**, *14*, 175–200. <https://doi.org/10.1016/j.apmt.2018.12.011>.
- (75) Zhou, W.; Wen, Z.; Gao, P. Less Is More: Dopant-Free Hole Transporting Materials for High-Efficiency Perovskite Solar Cells. *Adv. Energy Mater.* **2018**, *8* (9), 1–28. <https://doi.org/10.1002/aenm.201702512>.
- (76) Ummadisingu, A.; Seo, J.-Y.; Stojanovic, M.; Zakeeruddin, S. M.; Grätzel, M.; Hagfeldt, A.; Vlachopoulos, N.; Saliba, M. Additives, Hole Transporting Materials and Spectroscopic Methods to Characterize the Properties of Perovskite Films. *Chimia (Aarau)*. **2017**, *71* (11), 754. <https://doi.org/10.2533/chimia.2017.754>.
- (77) Desoky, M. M. H.; Bonomo, M.; Buscaino, R.; Fin, A.; Viscardi, G.; Barolo, C.;

- Quagliotto, P. Dopant-Free All-Organic Small-Molecule HTMs for Perovskite Solar Cells: Concepts and Structure–Property Relationships. *Energies* **2021**, *14* (8), 2279. <https://doi.org/10.3390/en14082279>.
- (78) Calió, L.; Kazim, S.; Grätzel, M.; Ahmad, S. Hole-Transport Materials for Perovskite Solar Cells. *Angew. Chemie Int. Ed.* **2016**, *55* (47), 14522–14545. <https://doi.org/10.1002/anie.201601757>.
- (79) Heeger, A. J. Semiconducting and Metallic Polymers: The Fourth Generation of Polymeric Materials. *Synth. Met.* **2001**, *125* (1), 23–42. [https://doi.org/10.1016/S0379-6779\(01\)00509-4](https://doi.org/10.1016/S0379-6779(01)00509-4).
- (80) Bach, U.; Lupo, D.; Comte, P.; Moser, J. E.; Weissörtel, F.; Salbeck, J.; Spreitzer, H.; Grätzel, M. Solid-State Dye-Sensitized Mesoporous TiO₂ Solar Cells with High Photon-to-Electron Conversion Efficiencies. *Nature* **1998**, *395* (6702), 583–585. <https://doi.org/10.1038/26936>.
- (81) Krüger, J.; Plass, R.; Cevey, L.; Piccirelli, M.; Grätzel, M.; Bach, U. High Efficiency Solid-State Photovoltaic Device Due to Inhibition of Interface Charge Recombination. *Appl. Phys. Lett.* **2001**, *79* (13), 2085–2087. <https://doi.org/10.1063/1.1406148>.
- (82) Burschka, J.; Dualeh, A.; Kessler, F.; Baranoff, E.; Cevey-Ha, N.-L.; Yi, C.; Nazeeruddin, M. K.; Grätzel, M. Tris(2-(1 H -Pyrazol-1-Yl)Pyridine)Cobalt(III) as p-Type Dopant for Organic Semiconductors and Its Application in Highly

- Efficient Solid-State Dye-Sensitized Solar Cells. *J. Am. Chem. Soc.* **2011**, *133* (45), 18042–18045. <https://doi.org/10.1021/ja207367t>.
- (83) Jeon, N. J.; Noh, J. H.; Yang, W. S.; Kim, Y. C.; Ryu, S.; Seo, J.; Seok, S. Il. Compositional Engineering of Perovskite Materials for High-Performance Solar Cells. *Nature* **2015**, *517* (7535), 476–480. <https://doi.org/10.1038/nature14133>.
- (84) Bi, D.; Tress, W.; Dar, M. I.; Gao, P.; Luo, J.; Renevier, C.; Schenk, K.; Abate, A.; Giordano, F.; Correa Baena, J.-P.; Decoppet, J.-D.; Zakeeruddin, S. M.; Nazeeruddin, M. K.; Grätzel, M.; Hagfeldt, A. Efficient Luminescent Solar Cells Based on Tailored Mixed-Cation Perovskites. *Sci. Adv.* **2016**, *2* (1), e1501170. <https://doi.org/10.1126/sciadv.1501170>.
- (85) Jeon, N. J.; Lee, H. G.; Kim, Y. C.; Seo, J.; Noh, J. H.; Lee, J.; Seok, S. Il. O - Methoxy Substituents in Spiro-OMeTAD for Efficient Inorganic–Organic Hybrid Perovskite Solar Cells. *J. Am. Chem. Soc.* **2014**, *136* (22), 7837–7840. <https://doi.org/10.1021/ja502824c>.
- (86) Iwan, A.; Sek, D. Polymers with Triphenylamine Units: Photonic and Electroactive Materials. *Prog. Polym. Sci.* **2011**, *36* (10), 1277–1325. <https://doi.org/10.1016/j.progpolymsci.2011.05.001>.
- (87) Choi, H.; Park, S.; Paek, S.; Ekanayake, P.; Nazeeruddin, M. K.; Ko, J. Efficient Star-Shaped Hole Transporting Materials with Diphenylethenyl Side Arms for

- an Efficient Perovskite Solar Cell. *J. Mater. Chem. A* **2014**, *2* (45), 19136–19140. <https://doi.org/10.1039/C4TA04179H>.
- (88) Kimpel, J.; Michinobu, T. Conjugated Polymers for Functional Applications: Lifetime and Performance of Polymeric Organic Semiconductors in Organic Field-Effect Transistors. *Polym. Int.* **2021**, *70* (4), 367–373. <https://doi.org/10.1002/pi.6020>.
- (89) Hou, W.; Xiao, Y.; Han, G.; Lin, J. Y. The Applications of Polymers in Solar Cells: A Review. *Polymers (Basel)*. **2019**, *11* (1), 1–46. <https://doi.org/10.3390/polym11010143>.
- (90) AlSalhi, M. S.; Alam, J.; Dass, L. A.; Raja, M. Recent Advances in Conjugated Polymers for Light Emitting Devices. *Int. J. Mol. Sci.* **2011**, *12* (3), 2036–2054. <https://doi.org/10.3390/ijms12032036>.
- (91) Desoky, M. M. H.; Bonomo, M.; Barbero, N.; Viscardi, G.; Barolo, C.; Quagliotto, P. Polymeric Dopant-Free Hole Transporting Materials for Perovskite Solar Cells: Structures and Concepts towards Better Performances. *Polymers (Basel)*. **2021**, *13* (10), 1652. <https://doi.org/10.3390/polym13101652>.
- (92) Magaldi, D.; Ulfa, M.; Nghiê, M. P.; Sini, G.; Goubard, F.; Pauporté, T.; Bui, T. T. Hole Transporting Materials for Perovskite Solar Cells: Molecular versus Polymeric Carbazole-Based Derivatives. *J. Mater. Sci.* **2020**, *55* (11), 4820–

4829. <https://doi.org/10.1007/s10853-019-04342-6>.

- (93) Hsu, C. Y.; Chen, Y. C.; Lin, R. Y. Y.; Ho, K. C.; Lin, J. T. Solid-State Dye-Sensitized Solar Cells Based on Spirofluorene (Spiro-OMeTAD) and Arylamines as Hole Transporting Materials. *Phys. Chem. Chem. Phys.* **2012**, *14* (41), 14099–14109. <https://doi.org/10.1039/c2cp41326d>.
- (94) Holliday, S.; Donaghey, J. E.; McCulloch, I. Advances in Charge Carrier Mobilities of Semiconducting Polymers Used in Organic Transistors. *Chem. Mater.* **2014**, *26* (1), 647–663. <https://doi.org/10.1021/cm402421p>.
- (95) Arias, A. C.; MacKenzie, J. D.; McCulloch, I.; Rivnay, J.; Salleo, A. Materials and Applications for Large Area Electronics: Solution-Based Approaches. *Chem. Rev.* **2010**, *110* (1), 3–24. <https://doi.org/10.1021/cr900150b>.
- (96) Zaumseil, J.; Sirringhaus, H. Electron and Ambipolar Transport in Organic Field-Effect Transistors. *Chem. Rev.* **2007**, *107* (4), 1296–1323. <https://doi.org/10.1021/cr0501543>.
- (97) Jung, E. H.; Jeon, N. J.; Park, E. Y.; Moon, C. S.; Shin, T. J.; Yang, T.-Y.; Noh, J. H.; Seo, J. Efficient, Stable and Scalable Perovskite Solar Cells Using Poly(3-Hexylthiophene). *Nature* **2019**, *567* (7749), 511–515. <https://doi.org/10.1038/s41586-019-1036-3>.
- (98) Chiang, C. H.; Nazeeruddin, M. K.; Grätzel, M.; Wu, C. G. The Synergistic Effect of H₂O and DMF towards Stable and 20% Efficiency Inverted

Perovskite Solar Cells. *Energy Environ. Sci.* **2017**, *10* (3), 808–817.

<https://doi.org/10.1039/c6ee03586h>.

- (99) Ning, Z.; Tian, H. Triarylamine: A Promising Core Unit for Efficient Photovoltaic Materials. *Chem. Commun.* **2009**, No. 37, 5483.
<https://doi.org/10.1039/b908802d>.
- (100) Heo, J. H.; Im, S. H.; Noh, J. H.; Mandal, T. N.; Lim, C.-S.; Chang, J. A.; Lee, Y. H.; Kim, H.; Sarkar, A.; Nazeeruddin, M. K.; Grätzel, M.; Seok, S. II. Efficient Inorganic–Organic Hybrid Heterojunction Solar Cells Containing Perovskite Compound and Polymeric Hole Conductors. *Nat. Photonics* **2013**, *7* (6), 486–491. <https://doi.org/10.1038/nphoton.2013.80>.
- (101) Coakley, K. M.; Srinivasan, B. S.; Ziebarth, J. M.; Goh, C.; Liu, Y.; McGehee, M. D. Enhanced Hole Mobility in Regioregular Polythiophene Infiltrated in Straight Nanopores. *Adv. Funct. Mater.* **2005**, *15* (12), 1927–1932.
<https://doi.org/10.1002/adfm.200500364>.
- (102) Cheng, Y.-J.; Yang, S.-H.; Hsu, C.-S. Synthesis of Conjugated Polymers for Organic Solar Cell Applications. *Chem. Rev.* **2009**, *109* (11), 5868–5923.
<https://doi.org/10.1021/cr900182s>.
- (103) Bi, D.; Yang, L.; Boschloo, G.; Hagfeldt, A.; Johansson, E. M. J. Effect of Different Hole Transport Materials on Recombination in CH₃NH₃PbI₃ Perovskite-Sensitized Mesoscopic Solar Cells. *J. Phys. Chem. Lett.* **2013**, *4* (9),

1532–1536. <https://doi.org/10.1021/jz400638x>.

- (104) Edri, E.; Kirmayer, S.; Cahen, D.; Hodes, G. High Open-Circuit Voltage Solar Cells Based on Organic-Inorganic Lead Bromide Perovskite. *J. Phys. Chem. Lett.* **2013**, *4* (6), 897–902. <https://doi.org/10.1021/jz400348q>.
- (105) Heo, J. H.; Im, S. H. CH₃NH₃PbI₃/Poly-3-Hexylthiophen Perovskite Mesoscopic Solar Cells: Performance Enhancement by Li-Assisted Hole Conduction. *Phys. Status Solidi - Rapid Res. Lett.* **2014**, *8* (10), 816–821. <https://doi.org/10.1002/pssr.201409330>.
- (106) Guo, Y.; Liu, C.; Inoue, K.; Harano, K.; Tanaka, H.; Nakamura, E. Enhancement in the Efficiency of an Organic-Inorganic Hybrid Solar Cell with a Doped P3HT Hole-Transporting Layer on a Void-Free Perovskite Active Layer. *J. Mater. Chem. A* **2014**, *2* (34), 13827–13830. <https://doi.org/10.1039/c4ta02976c>.
- (107) Bi, H.; Zhang, Y. Influence of the Additives in Poly(3-Hexylthiophene) Hole Transport Layer on the Performance of Perovskite Solar Cells. *Mater. Lett.* **2015**, *161*, 767–769. <https://doi.org/10.1016/j.matlet.2015.09.092>.
- (108) Yaghoobi Nia, N.; Bonomo, M.; Zendejdel, M.; Lamanna, E.; Desoky, M. M. H.; Paci, B.; Zurlo, F.; Generosi, A.; Barolo, C.; Viscardi, G.; Quagliotto, P.; Di Carlo, A. Impact of P3HT Regioregularity and Molecular Weight on the Efficiency and Stability of Perovskite Solar Cells. *ACS Sustain. Chem. Eng.* **2021**, *9* (14), 5061–5073. <https://doi.org/10.1021/acssuschemeng.0c09015>.

- (109) Rezaee, E.; Liu, X.; Hu, Q.; Dong, L.; Chen, Q.; Pan, J. H.; Xu, Z. X. Dopant-Free Hole Transporting Materials for Perovskite Solar Cells. *Sol. RRL* **2018**, *2* (11). <https://doi.org/10.1002/solr.201800200>.
- (110) Xiao, Z.; Dong, Q.; Bi, C.; Shao, Y.; Yuan, Y.; Huang, J. Solvent Annealing of Perovskite-Induced Crystal Growth for Photovoltaic-Device Efficiency Enhancement. *Adv. Mater.* **2014**, *26* (37), 6503–6509. <https://doi.org/10.1002/adma.201401685>.
- (111) You, J.; Yang, Y. (Michael); Hong, Z.; Song, T.-B.; Meng, L.; Liu, Y.; Jiang, C.; Zhou, H.; Chang, W.-H.; Li, G.; Yang, Y. Moisture Assisted Perovskite Film Growth for High Performance Solar Cells. *Appl. Phys. Lett.* **2014**, *105* (18), 183902. <https://doi.org/10.1063/1.4901510>.
- (112) Heo, J. H.; Han, H. J.; Kim, D.; Ahn, T. K.; Im, S. H. Hysteresis-Less Inverted CH₃NH₃PbI₃ Planar Perovskite Hybrid Solar Cells with 18.1% Power Conversion Efficiency. *Energy Environ. Sci.* **2015**, *8* (5), 1602–1608. <https://doi.org/10.1039/c5ee00120j>.
- (113) Salzmann, I.; Heimel, G.; Oehzelt, M.; Winkler, S.; Koch, N. Molecular Electrical Doping of Organic Semiconductors: Fundamental Mechanisms and Emerging Dopant Design Rules. *Acc. Chem. Res.* **2016**, *49* (3), 370–378. <https://doi.org/10.1021/acs.accounts.5b00438>.
- (114) Kim, J. M.; Yoo, S. J.; Moon, C. K.; Sim, B.; Lee, J. H.; Lim, H.; Kim, J. W.; Kim, J.

- J. N-Type Molecular Doping in Organic Semiconductors: Formation and Dissociation Efficiencies of a Charge Transfer Complex. *J. Phys. Chem. C* **2016**, *120* (17), 9475–9481. <https://doi.org/10.1021/acs.jpcc.6b01175>.
- (115) Lüsse, B.; Riede, M.; Leo, K. Doping of Organic Semiconductors. *Phys. status solidi* **2013**, *210* (1), 9–43. <https://doi.org/10.1002/pssa.201228310>.
- (116) Walzer, K.; Maennig, B.; Pfeiffer, M.; Leo, K. Highly Efficient Organic Devices Based on Electrically Doped Transport Layers. *Chem. Rev.* **2007**, *107* (4), 1233–1271. <https://doi.org/10.1021/cr050156n>.
- (117) Leijtens, T.; Giovenzana, T.; Habisreutinger, S. N.; Tinkham, J. S.; Noel, N. K.; Kamino, B. A.; Sadoughi, G.; Sellinger, A.; Snaith, H. J. Hydrophobic Organic Hole Transporters for Improved Moisture Resistance in Metal Halide Perovskite Solar Cells. *ACS Appl. Mater. Interfaces* **2016**, *8* (9), 5981–5989. <https://doi.org/10.1021/acsami.5b10093>.
- (118) Li, W.; Dong, H.; Wang, L.; Li, N.; Guo, X.; Li, J.; Qiu, Y. Montmorillonite as Bifunctional Buffer Layer Material for Hybrid Perovskite Solar Cells with Protection from Corrosion and Retarding Recombination. *J. Mater. Chem. A* **2014**, *2* (33), 13587–13592. <https://doi.org/10.1039/c4ta01550a>.
- (119) Magomedov, A.; Kasparavičius, E.; Rakstys, K.; Paek, S.; Gasilova, N.; Genevičius, K.; Juška, G.; Malinauskas, T.; Nazeeruddin, M. K.; Getautis, V. Pyridination of Hole Transporting Material in Perovskite Solar Cells

Questions the Long-Term Stability. *J. Mater. Chem. C* **2018**, *6* (33), 8874–8878. <https://doi.org/10.1039/c8tc02242a>.

- (120) Zhan, C.; Yao, J. More than Conformational “Twisting” or “Coplanarity”: Molecular Strategies for Designing High-Efficiency Nonfullerene Organic Solar Cells. *Chem. Mater.* **2016**, *28* (7), 1948–1964. <https://doi.org/10.1021/acs.chemmater.5b04339>.
- (121) Fernández-Lázaro, F.; Zink-Lorre, N.; Sastre-Santos, Á. Perylenediimides as Non-Fullerene Acceptors in Bulk-Heterojunction Solar Cells (BHJSCs). *J. Mater. Chem. A* **2016**, *4* (24), 9336–9346. <https://doi.org/10.1039/c6ta02045c>.
- (122) Huang, Z. S.; Meier, H.; Cao, D. Phenothiazine-Based Dyes for Efficient Dye-Sensitized Solar Cells. *Journal of Materials Chemistry C*. Royal Society of Chemistry 2016, pp 2404–2426. <https://doi.org/10.1039/c5tc04418a>.
- (123) Shinde, D. B.; Salunke, J. K.; Candeias, N. R.; Tinti, F.; Gazzano, M.; Wadgaonkar, P. P.; Priimagi, A.; Camaioni, N.; Vivo, P. Crystallisation-Enhanced Bulk Hole Mobility in Phenothiazine-Based Organic Semiconductors. *Sci. Rep.* **2017**, *7* (1), 46268. <https://doi.org/10.1038/srep46268>.
- (124) Karreman, G.; Isenberg, I.; Szent-Gyorgyi, A. On the Mechanism of Action of Chlorpromazine. *Science* **1959**, *130* (3383), 1191–1192.

<https://doi.org/10.1126/science.130.3383.1191>.

(125) Roseboom, H.; Perrin, J. H. Mechanism for Phenothiazine Oxidation. *J.*

Pharm. Sci. **1977**, *66* (10), 1395–1398.

<https://doi.org/10.1002/jps.2600661011>.

(126) G. Cauquis, A. Deronzier, D. S. No Title. *Bull. Soc. Chim. Fr.* **1976**, 295–302.

(127) Bosch, E.; Kochi, J. K. Catalytic Oxidation of Chlorpromazine and Related Phenothiazines. Cation Radicals as the Reactive Intermediates in Sulfoxide Formation. *J. Chem. Soc. Perkin Trans. 1* **1995**, No. 8, 1057.

<https://doi.org/10.1039/p19950001057>.

(128) Clarke, D.; Gilbert, B. C.; Hanson, P.; Kirk, C. M. Heterocyclic Free Radicals.

Part 8. The Influence of the Structure and the Conformation of the Side-Chain on the Properties of Phenothiazine Cation-Radicals Substituted at Nitrogen. *J. Chem. Soc. Perkin Trans. 2* **1978**, No. 10, 1103.

<https://doi.org/10.1039/p29780001103>.

(129) Hester, R. E.; Williams, K. P. J. Free Radical Studies by Resonance Raman Spectroscopy: Phenothiazine, 10-Methylphenothiazine, and Phenoxazine Radical Cations. *J. Chem. Soc. Perkin Trans. 2* **1981**, No. 5, 852.

<https://doi.org/10.1039/p29810000852>.

(130) Revoju, S.; Matuhina, A.; Canil, L.; Salonen, H.; Hiltunen, A.; Abate, A.; Vivo, P. Structure-Induced Optoelectronic Properties of Phenothiazine-Based

Materials. *J. Mater. Chem. C* **2020**, *8* (44), 15486–15506.

<https://doi.org/10.1039/D0TC03421E>.

- (131) Duesing, R.; Tapolsky, G.; Meyer, T. J. Long-Range, Light-Induced Redox Separation across a Ligand Bridge. *J. Am. Chem. Soc.* **1990**, *112* (13), 5378–5379. <https://doi.org/10.1021/ja00169a071>.
- (132) Daub, J.; Engl, R.; Kurzawa, J.; Miller, S. E.; Schneider, S.; Stockmann, A.; Wasielewski, M. R. Competition between Conformational Relaxation and Intramolecular Electron Transfer within Phenothiazine–Pyrene Dyads. *J. Phys. Chem. A* **2001**, *105* (23), 5655–5665. <https://doi.org/10.1021/jp0037293>.
- (133) Mako, T. L.; Racicot, J. M.; Levine, M. Supramolecular Luminescent Sensors. *Chem. Rev.* **2019**, *119* (1), 322–477. <https://doi.org/10.1021/acs.chemrev.8b00260>.
- (134) Zhang, X. H.; Seon, H. K.; In, S. L.; Chun, J. G.; Yang, S. I.; Ahn, K. H. Synthesis, Photophysical and Electrochemical Properties of Novel Conjugated Donor-Acceptor Molecules Based on Phenothiazine and Benzimidazole. *Bull. Korean Chem. Soc.* **2007**, *28* (8), 1389–1395. <https://doi.org/10.5012/bkcs.2007.28.8.1389>.
- (135) Al-Busaidi, I. J.; Haque, A.; Al Rasbi, N. K.; Khan, M. S. Phenothiazine-Based Derivatives for Optoelectronic Applications: A Review. *Synth. Met.* **2019**, *257*

(October), 116189. <https://doi.org/10.1016/j.synthmet.2019.116189>.

- (136) Han, Y. S.; Kim, S. D.; Park, L. S.; Kim, D. U.; Kwon, Y. Synthesis of Conjugated Copolymers Containing Phenothiazinylene Vinylene Moieties and Their Electrooptic Properties. *J. Polym. Sci. Part A Polym. Chem.* **2003**, *41* (16), 2502–2511. <https://doi.org/10.1002/pola.10793>.
- (137) Tse-Wei Wang, J.; M. Ball, J.; M. Barea, E.; Abate, A.; A. Alexander-Webber, J.; Huang, J.; Saliba, M.; Mora-Sero, I.; Bisquert, J.; J. Snaith, H.; J. Nicholas, R. Low-Temperature Processed Electron Collection Layers of Graphene/TiO₂ Nanocomposites in Thin Film Perovskite Solar Cells. *Nano Lett.* **2014**, *14* (2), 724–730. <https://doi.org/10.1021/nl403997a>.
- (138) Zheng, D.; Wang, G.; Huang, W.; Wang, B.; Ke, W.; Logsdon, J. L.; Wang, H.; Wang, Z.; Zhu, W.; Yu, J.; Wasielewski, M. R.; Kanatzidis, M. G.; Marks, T. J.; Facchetti, A. Combustion Synthesized Zinc Oxide Electron-Transport Layers for Efficient and Stable Perovskite Solar Cells. *Adv. Funct. Mater.* **2019**, *29* (16), 1900265. <https://doi.org/https://doi.org/10.1002/adfm.201900265>.
- (139) Zhao, X.; Quan, Y.; Pan, H.; Li, Q.; Shen, Y.; Huang, Z.-S.; Wang, M. Novel Donor-Acceptor-Donor Structured Small Molecular Hole Transporting Materials for Planar Perovskite Solar Cells. *J. Energy Chem.* **2019**, *32*, 85–92. <https://doi.org/10.1016/j.jechem.2018.07.009>.
- (140) Zhang, F.; Wang, S.; Zhu, H.; Liu, X.; Liu, H.; Li, X.; Xiao, Y.; Mohammed

Zakeeruddin, S.; Grätzel, M. Impact of Peripheral Groups on Phenothiazine-Based Hole-Transporting Materials for Perovskite Solar Cells. *ACS Energy Lett.* **2018**, *3* (5), 1145–1152.

<https://doi.org/10.1021/acsenergylett.8b00395>.

(141) Grisorio, R.; Roose, B.; Colella, S.; Listorti, A.; Paolo Suranna, G.; Abate, A. Molecular Tailoring of Phenothiazine-Based Hole-Transporting Materials for High-Performing Perovskite Solar Cells. *ACS Energy Lett.* **2017**, *2* (5), 1029–1034. <https://doi.org/10.1021/acsenergylett.7b00054>.

(142) Salunke, J.; Guo, X.; Lin, Z.; R. Vale, J.; R. Candeias, N.; Nyman, M.; Dahlström, S.; Österbacka, R.; Priimagi, A.; Chang, J.; Vivo, P. Phenothiazine-Based Hole-Transporting Materials toward Eco-Friendly Perovskite Solar Cells. *ACS Appl. Energy Mater.* **2019**, *2* (5), 3021–3027. <https://doi.org/10.1021/acsaem.9b00408>.

(143) Ding, X.; Chen, C.; Sun, L.; Li, H.; Chen, H.; Su, J.; Li, H.; Li, H.; Xu, L.; Cheng, M. Highly Efficient Phenothiazine 5,5-Dioxide-Based Hole Transport Materials for Planar Perovskite Solar Cells with a PCE Exceeding 20%. *J. Mater. Chem. A* **2019**, *7* (16), 9510–9516. <https://doi.org/10.1039/c9ta00654k>.

(144) Chen, Y.; Xu, X.; Cai, N.; Qian, S.; Luo, R.; Huo, Y.; Tsang, S. Rational Design of Dopant-Free Coplanar D- π -D Hole-Transporting Materials for High-

Performance Perovskite Solar Cells with Fill Factor Exceeding 80%. *Adv.*

Energy Mater. **2019**, *9* (39), 1901268.

<https://doi.org/10.1002/aenm.201901268>.

- (145) Liu, X.; Tan, X.; Chen, Q.; Shan, H.; Liu, C.; Xu, J.; Chen, Z.-K.; Huang, W.; Xu, Z.-X. Facile Synthesis of a Dopant-Free Hole Transporting Material with a Phenothiazine Core for Planar Perovskite Solar Cells. *RSC Adv.* **2017**, *7* (84), 53604–53610. <https://doi.org/10.1039/C7RA10677G>.
- (146) Maciejczyk, M. R.; Chen, R.; Brown, A.; Zheng, N.; Robertson, N. Beyond Efficiency: Phenothiazine, a New Commercially Viable Substituent for Hole Transport Materials in Perovskite Solar Cells. *J. Mater. Chem. C* **2019**, *7* (28), 8593–8598. <https://doi.org/10.1039/c8tc05773g>.
- (147) Maciejczyk, M.; Ivaturi, A.; Robertson, N. SFX as a Low-Cost ‘Spiro’ Hole-Transport Material for Efficient Perovskite Solar Cells. *J. Mater. Chem. A* **2016**, *4* (13), 4855–4863. <https://doi.org/10.1039/C6TA00110F>.
- (148) Liang, X.; Wang, C.; Wu, M.; Wu, Y.; Zhang, F.; Han, Z.; Lu, X.; Guo, K.; Zhao, Y.-M. Effects of Core Moiety and Substituted Positions in Phenothiazine-Based Hole Transporting Materials towards High Thermal Stability and Good Hole Mobility. *Tetrahedron* **2017**, *73* (50), 7115–7121. <https://doi.org/10.1016/j.tet.2017.11.003>.
- (149) Zhai, M.; Miao, Y.; Chen, C.; Wang, H.; Ding, X.; Wu, C.; Yang, X.; Cheng, M.

Molecular Engineering of Phenothiazine-Based Monomer and Dimer Hole Transport Materials and Their Photovoltaic Performance. *Dye. Pigment.*

2021, *191* (February), 109340.

<https://doi.org/10.1016/j.dyepig.2021.109340>.

- (150) Merbs, S. L.; Nathans, J. Absorption Spectra of Human Cone Pigments. *Nature* **1992**, *356* (6368), 433–435. <https://doi.org/10.1038/356433a0>.
- (151) Löper, P.; Moon, S.-J.; Martín de Nicolas, S.; Niesen, B.; Ledinsky, M.; Nicolay, S.; Bailat, J.; Yum, J.-H.; De Wolf, S.; Ballif, C. Organic–Inorganic Halide Perovskite/Crystalline Silicon Four-Terminal Tandem Solar Cells. *Phys. Chem. Chem. Phys.* **2015**, *17* (3), 1619–1629. <https://doi.org/10.1039/C4CP03788J>.
- (152) Bailie, C. D.; Christoforo, M. G.; Mailoa, J. P.; Bowring, A. R.; Unger, E. L.; Nguyen, W. H.; Burschka, J.; Pellet, N.; Lee, J. Z.; Grätzel, M.; Noufi, R.; Buonassisi, T.; Salleo, A.; McGehee, M. D. Semi-Transparent Perovskite Solar Cells for Tandems with Silicon and CIGS. *Energy Environ. Sci.* **2015**, *8* (3), 956–963. <https://doi.org/10.1039/C4EE03322A>.
- (153) Pattanasattayavong, P.; Yaacobi-Gross, N.; Zhao, K.; Ndjawa, G. O. N.; Li, J.; Yan, F.; O'Regan, B. C.; Amassian, A.; Anthopoulos, T. D. Hole-Transporting Transistors and Circuits Based on the Transparent Inorganic Semiconductor Copper(I) Thiocyanate (CuSCN) Processed from Solution at Room Temperature. *Adv. Mater.* **2013**, *25* (10), 1504–1509.

<https://doi.org/10.1002/adma.201202758>.

- (154) Qin, P.; Tanaka, S.; Ito, S.; Tetreault, N.; Manabe, K.; Nishino, H.; Nazeeruddin, M. K.; Grätzel, M. Inorganic Hole Conductor-Based Lead Halide Perovskite Solar Cells with 12.4% Conversion Efficiency. *Nat. Commun.* **2014**, *5* (1), 3834. <https://doi.org/10.1038/ncomms4834>.
- (155) Yamada, N.; Ino, R.; Ninomiya, Y. Truly Transparent P-Type γ -CuI Thin Films with High Hole Mobility. *Chem. Mater.* **2016**, *28* (14), 4971–4981. <https://doi.org/10.1021/acs.chemmater.6b01358>.
- (156) Jeng, J.-Y.; Chen, K.-C.; Chiang, T.-Y.; Lin, P.-Y.; Tsai, T.-D.; Chang, Y.-C.; Guo, T.-F.; Chen, P.; Wen, T.-C.; Hsu, Y.-J. Nickel Oxide Electrode Interlayer in $\text{CH}_3\text{NH}_3\text{PbI}_3$ Perovskite/PCBM Planar-Heterojunction Hybrid Solar Cells. *Adv. Mater.* **2014**, *26* (24), 4107–4113. <https://doi.org/10.1002/adma.201306217>.
- (157) Manders, J. R.; Tsang, S.-W.; Hartel, M. J.; Lai, T.-H.; Chen, S.; Amb, C. M.; Reynolds, J. R.; So, F. Solution-Processed Nickel Oxide Hole Transport Layers in High Efficiency Polymer Photovoltaic Cells. *Adv. Funct. Mater.* **2013**, *23* (23), 2993–3001. <https://doi.org/10.1002/adfm.201202269>.
- (158) Battaglia, C.; Yin, X.; Zheng, M.; Sharp, I. D.; Chen, T.; McDonnell, S.; Azcatl, A.; Carraro, C.; Ma, B.; Maboudian, R.; Wallace, R. M.; Javey, A. Hole Selective MoOx Contact for Silicon Solar Cells. *Nano Lett.* **2014**, *14* (2), 967–971. <https://doi.org/10.1021/nl404389u>.

- (159) Wang, J.; Ibarra, V.; Barrera, D.; Xu, L.; Lee, Y.-J.; Hsu, J. W. P. Solution Synthesized p-Type Copper Gallium Oxide Nanoplates as Hole Transport Layer for Organic Photovoltaic Devices. *J. Phys. Chem. Lett.* **2015**, *6* (6), 1071–1075. <https://doi.org/10.1021/acs.jpcclett.5b00236>.
- (160) Liu, M.-L.; Wu, L.-B.; Huang, F.-Q.; Chen, L.-D.; Chen, I.-W. A Promising P-Type Transparent Conducting Material: Layered Oxysulfide [Cu₂S₂][Sr₃Sc₂O₅]. *J. Appl. Phys.* **2007**, *102* (11), 116108. <https://doi.org/10.1063/1.2817643>.
- (161) Zhou, H.; Chen, Q.; Li, G.; Luo, S.; Song, T.; Duan, H.-S.; Hong, Z.; You, J.; Liu, Y.; Yang, Y. Photovoltaics. Interface Engineering of Highly Efficient Perovskite Solar Cells. *Science* **2014**, *345* (6196), 542–546. <https://doi.org/10.1126/science.1254050>.
- (162) Petrus, M. L.; Music, A.; Closs, A. C.; Bijleveld, J. C.; Sirtl, M. T.; Hu, Y.; Dingemans, T. J.; Bein, T.; Docampo, P. Design Rules for the Preparation of Low-Cost Hole Transporting Materials for Perovskite Solar Cells with Moisture Barrier Properties. *J. Mater. Chem. A* **2017**, *5* (48), 25200–25210. <https://doi.org/10.1039/C7TA06452G>.
- (163) Yin, X.; Song, Z.; Li, Z.; Tang, W. Toward Ideal Hole Transport Materials: A Review on Recent Progress in Dopant-Free Hole Transport Materials for Fabricating Efficient and Stable Perovskite Solar Cells. *Energy Environ. Sci.* **2020**, *13* (11), 4057–4086. <https://doi.org/10.1039/D0EE02337J>.

- (164) Nishimura, H.; Hasegawa, Y.; Wakamiya, A.; Murata, Y. Development of Transparent Organic Hole-Transporting Materials Using Partially Oxygen-Bridged Triphenylamine Skeletons. *Chem. Lett.* **2017**, *46* (6), 817–820.
<https://doi.org/10.1246/cl.170164>.
- (165) Dongxue, L.; Liu, Y. Recent Progress of Dopant-Free Organic Hole-Transporting Materials in Perovskite Solar Cells. *J. Semicond.* **2017**, *38* (1), 011005. <https://doi.org/10.1088/1674-4926/38/1/011005>.
- (166) Wang, Z.; Kamarudin, M. A.; Huey, N. C.; Yang, F.; Pandey, M.; Kapil, G.; Ma, T.; Hayase, S. Interfacial Sulfur Functionalization Anchoring SnO₂ and CH₃NH₃PbI₃ for Enhanced Stability and Trap Passivation in Perovskite Solar Cells. *ChemSusChem* **2018**, *11* (22), 3941–3948.
<https://doi.org/10.1002/cssc.201801888>.
- (167) Liu, S.; Cao, W.; Xia, D.; Zhang, J.; Fan, J.; An, C.; Fan, R.; Hao, S.; Lin, K.; Yang, Y. Sulfur-Rich Benzodithieno[3,2-b]Thiophene-Cored Hole Transporting Materials for Long-Time Stability of Perovskite Solar Cells. *Dye. Pigment.* **2021**, *193* (March), 109506. <https://doi.org/10.1016/j.dyepig.2021.109506>.
- (168) Plater, M. J.; Harrison, W. T. A. Characterisation of 3,7-Dibromophenothiazin-5-ium Perbromide and Its Use for Enhancing Latent Fingerprints. *J. Chem. Res.* **2009**, *2009* (6), 384–387.
<https://doi.org/10.3184/030823409X460704>.

- (169) de Meester, P.; Chu, S. S. C.; Jovanovic, M. V.; Biehl, E. R. Structure of 3,7-Dibromo-10-Ethylphenothiazine. *Acta Crystallogr. Sect. C Cryst. Struct. Commun.* **1986**, *42* (12), 1794–1797.
<https://doi.org/10.1107/S0108270186090522>.
- (170) Hartwig, J. Palladium-Catalyzed Amination of Aryl Halides: Mechanism and Rational Catalyst Design. *Synlett* **1997**, *1997* (4), 329–340.
<https://doi.org/10.1055/s-1997-789>.
- (171) SUNTHANKAR, S. V.; GILMAN, H. HALOGEN-METAL INTERCONVERSION AND METALATION IN THE NAPHTHALENE SERIES. *J. Org. Chem.* **1951**, *16* (1), 8–16.
<https://doi.org/10.1021/jo01141a002>.
- (172) Wittig, G.; Schöllkopf, U. Zum Chemismus Der Halogen-Lithium-Austauschreaktion. *Tetrahedron* **1958**, *3* (1), 91–93.
[https://doi.org/10.1016/S0040-4020\(01\)82616-8](https://doi.org/10.1016/S0040-4020(01)82616-8).
- (173) Miyaura, N.; Suzuki, A. Stereoselective Synthesis of Arylated (E)-Alkenes by the Reaction of Alk-1-Enylboranes with Aryl Halides in the Presence of Palladium Catalyst. *J. Chem. Soc. Chem. Commun.* **1979**, No. 19, 866.
<https://doi.org/10.1039/c39790000866>.
- (174) Miyaura, N.; Yamada, K.; Suzuki, A. A New Stereospecific Cross-Coupling by the Palladium-Catalyzed Reaction of 1-Alkenylboranes with 1-Alkenyl or 1-Alkynyl Halides. *Tetrahedron Lett.* **1979**, *20* (36), 3437–3440.

[https://doi.org/10.1016/S0040-4039\(01\)95429-2](https://doi.org/10.1016/S0040-4039(01)95429-2).

- (175) Miyaura, N.; Suzuki, A. Palladium-Catalyzed Cross-Coupling Reactions of Organoboron Compounds. *Chem. Rev.* **1995**, *95* (7), 2457–2483.
<https://doi.org/10.1021/cr00039a007>.
- (176) Han, F. S. Transition-Metal-Catalyzed Suzuki-Miyaura Cross-Coupling Reactions: A Remarkable Advance from Palladium to Nickel Catalysts. *Chem. Soc. Rev.* **2013**, *42* (12), 5270–5298. <https://doi.org/10.1039/c3cs35521g>.
- (177) Hassan, J.; Sévignon, M.; Gozzi, C.; Schulz, E.; Lemaire, M. Aryl-Aryl Bond Formation One Century after the Discovery of the Ullmann Reaction. *Chem. Rev.* **2002**, *102* (5), 1359–1469. <https://doi.org/10.1021/cr000664r>.
- (178) *Transition Metal-Catalyzed Couplings in Process Chemistry*; Magano, J., Dunetz, J. R., Eds.; Wiley-VCH Verlag GmbH & Co. KGaA: Weinheim, Germany, 2003. <https://doi.org/10.1002/9783527658909>.
- (179) The Nobel Prize in Chemistry 2010
<https://www.nobelprize.org/prizes/chemistry/2010/summary/>.
- (180) Suzuki, A. Cross-Coupling Reactions via Organoboranes. *J. Organomet. Chem.* **2002**, *653* (1–2), 83–90. [https://doi.org/10.1016/S0022-328X\(02\)01269-X](https://doi.org/10.1016/S0022-328X(02)01269-X).
- (181) Yang, X.; Dou, X.; Müllen, K. Efficient Synthesis of Symmetrically and Unsymmetrically Substituted Hexaphenylbenzene Analogues by Suzuki-Miyaura Coupling Reactions. *Chem. Asian J.* **2008**, *3* (4), 759–766.

<https://doi.org/10.1002/asia.200700370>.

- (182) Saïd, K.; Moussaoui, Y.; Salem, R. Ben. Heck Coupling Styrene With Aryl Halides Catalyzed By Palladium Complexes in Biphasic Media. *J. Soc. Chim. Tunis* **2009**, *11* (216), 59–67.
- (183) Sprick, R. S.; Hoyos, M.; Morrison, J. J.; Grace, I. M.; Lambert, C.; Navarro, O.; Turner, M. L. Triarylamine Polymers of Bridged Phenylenes by (N-Heterocyclic Carbene)-Palladium Catalysed C-N Coupling. *J. Mater. Chem. C* **2013**, *1* (20), 3327–3336. <https://doi.org/10.1039/c3tc30368c>.
- (184) Costa, J. C. S.; Taveira, R. J. S.; Lima, C. F. R. A. C.; Mendes, A.; Santos, L. M. N. B. F. Optical Band Gaps of Organic Semiconductor Materials. *Opt. Mater. (Amst)*. **2016**, *58*, 51–60. <https://doi.org/10.1016/j.optmat.2016.03.041>.
- (185) Ashassi-Sorkhabi, H.; Salehi-Abar, P. How the Change of OMe Substituent Position Affects the Performance of Spiro-OMeTAD in Neutral and Oxidized Forms: Theoretical Approaches. *RSC Adv.* **2018**, *8* (33), 18234–18242. <https://doi.org/10.1039/C8RA01879K>.
- (186) Alberga, D.; Mangiatordi, G. F.; Labat, F.; Ciofini, I.; Nicolotti, O.; Lattanzi, G.; Adamo, C. Theoretical Investigation of Hole Transporter Materials for Energy Devices. *J. Phys. Chem. C* **2015**, *119* (42), 23890–23898. <https://doi.org/10.1021/acs.jpcc.5b08981>.
- (187) Arora, N.; Orlandi, S.; Dar, M. I.; Aghazada, S.; Jacopin, G.; Cavazzini, M.;

- Mosconi, E.; Grätzel, M.; De Angelis, F.; Pozzi, G.; Graetzel, M.; Nazeeruddin, M. K. High Open-Circuit Voltage: Fabrication of Formamidinium Lead Bromide Perovskite Solar Cells Using Fluorene–Dithiophene Derivatives as Hole-Transporting Materials. *ACS Energy Lett.* **2016**, *1* (1), 107–112.
<https://doi.org/10.1021/acsenergylett.6b00077>.
- (188) Costa, J. C. S.; Lima, M. A. L.; Mendes, A.; Santos, L. M. N. B. F. The Impact of Phenyl-Phenyl Linkage on the Thermodynamic, Optical and Morphological Behavior of Carbazol Derivatives. *RSC Adv.* **2020**, *10* (20), 11766–11776.
<https://doi.org/10.1039/d0ra01518k>.
- (189) Liu, Y.; Hong, Z.; Chen, Q.; Chen, H.; Chang, W.-H.; Yang, Y. M.; Song, T.-B.; Yang, Y. Perovskite Solar Cells Employing Dopant-Free Organic Hole Transport Materials with Tunable Energy Levels. *Adv. Mater.* **2016**, *28* (3), 440–446. <https://doi.org/10.1002/adma.201504293>.
- (190) Bahrami, B.; Pathak, R.; Chowdhury, A. H.; Reza, K. M.; Chen, K.; Mabrouk, S.; El-magrou, A. A.; Qiao, Q. Modeling of Charge Transfer in Mesoscopic Perovskite Solar Cells by Considering a Trapassisted Interface. In *2019 IEEE International Conference on Electro Information Technology (EIT)*; IEEE, 2019; pp 578–583. <https://doi.org/10.1109/EIT.2019.8834020>.
- (191) Wu, Y.; Wang, Z.; Liang, M.; Cheng, H.; Li, M.; Liu, L.; Wang, B.; Wu, J.; Prasad Ghimire, R.; Wang, X.; Sun, Z.; Xue, S.; Qiao, Q. Influence of Nonfused Cores

- on the Photovoltaic Performance of Linear Triphenylamine-Based Hole-Transporting Materials for Perovskite Solar Cells. *ACS Appl. Mater. Interfaces* **2018**, *10* (21), 17883–17895. <https://doi.org/10.1021/acsami.8b02090>.
- (192) Ni, C.; Huang, Y.; Zeng, T.; Chen, D.; Chen, H.; Wei, M.; Johnston, A.; Proppe, A. H.; Ning, Z.; Sargent, E. H.; Hu, P.; Yang, Z. Thiophene Cation Intercalation to Improve Band-Edge Integrity in Reduced-Dimensional Perovskites. *Angew. Chemie Int. Ed.* **2020**, *59* (33), 13977–13983. <https://doi.org/10.1002/anie.202006112>.
- (193) Bach, U.; Lupo, D.; Comte, P.; Moser, J. E.; Weissörtel, F.; Salbeck, J.; Spreitzer, H.; Grätzel, M. Solid-State Dye-Sensitized Mesoporous TiO₂ Solar Cells with High Photon-to-Electron Conversion Efficiencies. *Nature* **1998**, *395* (6702), 583–585. <https://doi.org/10.1038/26936>.
- (194) Leijtens, T.; Ding, I.-K.; Giovenzana, T.; Bloking, J. T.; McGehee, M. D.; Sellinger, A. Hole Transport Materials with Low Glass Transition Temperatures and High Solubility for Application in Solid-State Dye-Sensitized Solar Cells. *ACS Nano* **2012**, *6* (2), 1455–1462. <https://doi.org/10.1021/nn204296b>.
- (195) Höcker, J.; Kiermasch, D.; Rieder, P.; Tvingstedt, K.; Baumann, A.; Dyakonov, V. Efficient Solution Processed CH₃NH₃PbI₃ Perovskite Solar Cells with PolyTPD Hole Transport Layer. *Zeitschrift für Naturforsch. A* **2019**, *74* (8),

665–672. <https://doi.org/10.1515/zna-2019-0127>.

- (196) Gao, L.; Schloemer, T. H.; Zhang, F.; Chen, X.; Xiao, C.; Zhu, K.; Sellinger, A. Carbazole-Based Hole-Transport Materials for High-Efficiency and Stable Perovskite Solar Cells. *ACS Appl. Energy Mater.* **2020**, *3* (5), 4492–4498. <https://doi.org/10.1021/acsaem.0c00179>.
- (197) Kim, Y.; Jung, E. H.; Kim, G.; Kim, D.; Kim, B. J.; Seo, J. Sequentially Fluorinated PTAA Polymers for Enhancing V_{oc} of High-Performance Perovskite Solar Cells. *Adv. Energy Mater.* **2018**, *8* (29), 1801668. <https://doi.org/10.1002/aenm.201801668>.
- (198) Xie, Y.; Wang, X.; Chen, Q.; Liu, S.; Yun, Y.; Liu, Y.; Chen, C.; Wang, J.; Cao, Y.; Wang, F.; Qin, T.; Huang, W. Dopant-Free Hole-Transporting Polycarbazoles with Tailored Backbones for Efficient Inverted Perovskite Solar Cells. *Macromolecules* **2019**, *52* (12), 4757–4764. <https://doi.org/10.1021/acs.macromol.9b00372>.
- (199) Schloemer, T. H.; Gehan, T. S.; Christians, J. A.; Mitchell, D. G.; Dixon, A.; Li, Z.; Zhu, K.; Berry, J. J.; Luther, J. M.; Sellinger, A. Thermally Stable Perovskite Solar Cells by Systematic Molecular Design of the Hole-Transport Layer. *ACS Energy Lett.* **2019**, *4* (2), 473–482. <https://doi.org/10.1021/acsenergylett.8b02431>.

LIST OF ABBREVIATIONS

\$: American dollar

(IPr)Pd(allyl)Cl

°C: Celsius

Ag/AgCl: silver/silver chloride

Au: gold

AVT: average visible transmittance

B_g: optical band gap

Br₂: bromine

CE: counter electrode

CH₃NH₃PbBr₃: methylammonium lead bromide

cm: centimeter

CV: cyclic voltammetry

DCM or CH₂Cl₂: dichloromethane

DFT: density function theory

DHA: double-layered halide structure

DMF: dimethylformamide

DSSCs: Dye Sensitized Solar Cells

e⁻: electron

$E_{1/2}$: half wave potential

EN: electronegativity

EPR: Electron Paramagnetic Resonance spectroscopy

Eq: molar equivalent

ETL: electron transport layer

eV: electron volt

FF: fill factor

FTO: fluorine-doped tin oxide glass

g: gram

GW: Giga Watt

h: hour

HOMO: Higher Occupied Molecular Orbital

HTL: Hole Transporting Layer

HTMs: Hole Transporting Materials

ITO: indium tin oxide glass

J_{sc} : short circuit current density

K_2CO_3 : potassium carbonate

KOtBu: Potassium tetra butoxide

LiTFSI: bis(trifluoromethanesulfonyl)imide

LUMO: Lower Unoccupied Molecular Orbital

M: molar concentration

mCPBA: meta-chloroperoxybenzoic acid

N₂: nitrogen gas

NaH: sodium hydride

NaOtBu: sodium tert-butoxide

n-BuLi: butyl lithium

NIR: Near InfraRed

nm: nanometer

OSCs: Organic SemiConductors

P(tBu)₃: tri-tert-butylphosphine

P3HT: poly(3-hexylthiophene)

PCE: Power Conversion Efficiency

Pd(PPh₃)₄: Tetrakis(triphenylphosphine)palladium(0)

Pd: palladium

Pd₂dba₃: tris(dibenzylideneacetone)dipalladium(0)

PEDOT: Poly(3,4-ethylenedioxythiophene)

PEDOT:PSS: poly(3,4-ethylenedioxythiophene) polystyrene sulfonate

PET: Photoinduced Electron Transfer

PMMA: (poly(methyl methacrylate))

PSCs: Perovskite Solar Cells

PSK: Perovskite

PTAA: polytriarylamine

PTZ: phenothiazine

PV: photovoltaics

RR: regioregularity

rt: room temperature

s: second

S...N vector: sulphur nitrogen vector

Spiro-OMeTAD:(2,2',7,7'-tetrakis[N,N-di(4-methoxyphenyl)amino]-9,9'-

spirobifluorene

SS: Stokes Shift

TBAPF₆: tetrabutylammonium hexafluorophosphate

t-BP: 4-tert-butylpyridine

Temp. or T: temperature

T_g: glass transition Temperature

THF: tetrahydrofuran

TiO₂: titanium dioxide

T_{stab}: stability temperature

Uv-Vis: ultraviolet–visible spectroscopy

V: volt

V_{oc} : open circuit voltage

WBH: Wide Band gap Halide

λ : wavelength

λ_{abs} : absorption maximum wavelength

λ_{em} : emission wavelength

λ_{onset} : absorption onset wavelength